Noncollinear Magnetism in Surfaces and Interfaces of Transition Metals

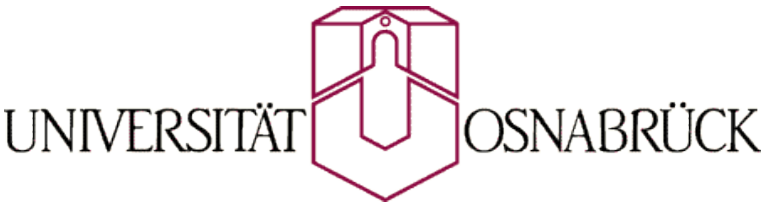

Master of Science
Huahai Tan

A thesis submitted for the
degree of *Doctor of Science* (Dr. rer. nat.)

to the
Department of Physics
University of Osnabrück

September 2009

Supervisor: Prof. Dr. Gunnar Borstel

"There's Plenty of Room at the Bottom."

—— Richard Feynman, December 29, 1959

Contents

Abbreviations

DFT	Density Functional Theory
DOS	Density of States
GCN	Global Charge Neutrality
GMR	Giant Magnetoresistance
LCAO	Linear Combination of Atomic Orbitals
LCN	Local Charge Neutrality
LDOS	Local Density of States
MOKE	Magneto-Optical Kerr Effect
STM	Scanning Tunneling Microscope
STS	Scanning Tunneling Spectroscopy
TB	Tight Binding
TB-LMTO	Tight-Binding Linear Muffin-Tin Orbitals

Chapter 1

Introduction

With our human eyes, we could see the blue sky, green trees, red flowers, and so on, all of which make up our colorful world. This is a macroscopic perspective. When we look deep into the scale of so-called "nanometer", everything changes. It is another fascinating world governed by quantum mechanics whose effects can be observed by powerful microscopes and spectroscopes. The technological applications under nanometer are referred to as nanotechnology, which becomes a popular word whatever you understand what its real meaning is. The first use of the concepts in "nanotechnology" was in a talk given by Richard Feynman, *There's Plenty of Room at the Bottom*, in 1959. In that talk he described a process by which the ability to manipulate individual atoms and molecules might be developed, using one set of precise tools to build and operate another proportionally smaller set, so on down to the needed scale. As time passes by, more and more technological innovations regarding nanotechnology become reality or at an advanced stage of research and development, such as the improvements in catalyst particles, coating materials, microscopic scale lithography, medicines to fight against cancer or other diseases, hard disk readers, quantum computing, etc.. Due to the promising revolution in our daily life, a large number of research centers either supported by governments or by companies, especially in developed countries such as USA, Japan, Germany, UK and France, has been investing numerous funds into this exciting area.

As we benefit from the amazing technological advances, it is necessary to conduct a thorough theoretical and experimental study of them. In this thesis we describe the theory of magnetism in nanostructures of transition metals. When the dimension of these materials are down to 10 nm, new magnetic properties emerge, such as large magnetic moments in free clusters [1, 2], dynamic exchange coupling [3], spin waves [4, 5] and giant magnetoresistance (GMR) [6, 7]. These properties lead to applications in permanent magnets, high-density data storage devices [8, 9], new magnetic refrigeration systems [10], agents amplifiers for magnetic resonance imaging [11], catalysis [12] and administration of controlled drugs [13]. Taking GMR as an example, we could imagine the great successes that nanotechnology has achieved to change our lives. In the late 1980s, two groups led by Albert Fert in France and Peter Grünberg in Germany discovered independently the existence of GMR in multilayers of transition metals (Fe and Cr). Now this technology is commercially used by manufacturers of hard disk drives. And the two physicists were awarded the Noble Prize in physics in 2007 for the discovery of GMR.

With regard to the experimental techniques, one of the most important instruments is the scanning tunneling microscope (STM). Its development in 1981 earned its inventors, Gerd Binning and Heinrich Rohrer [14–16] (at IBM Zürich), the Nobel Prize in physics in 1986. STM makes it possible to resolve the atomic structure of surfaces. And during the last two decades, the techniques of microscopy such as the scanning tunneling spectroscopy (STS) have been significantly developed. On the other hand, in order to implement these observing techniques, the method of preparing samples also advances, e.g., the epitaxial growth technique which can be used to produce thin films of metals and semiconductors [17–19], especially those made of magnetic metals, leading to the fabrication of spin electronic devices. Compared to traditional electronics, which only use the charge information of electrons, e.g., electric current and voltage, the new “spintronics” takes into account additionally the spin information. Every electron could be regarded as a carrier of a bit. It sheds light on the possibility to achieve the storage device of ultrahigh density.

To investigate surfaces and interfaces of thin films, different methods are employed such as the photoelectron spectroscopy with spin polarization (SP-PES), spin polarized low energy electron diffraction (SP-LEED), X-ray magnetic circular dichroism (XMCD), magneto-optical Kerr effect (MOKE) etc. However, these techniques are not capable of resolving information of magnetism at the atomic scale. The atomic force microscopy (AFM) is able to obtain a resolution of 30 nm in high vacuum [20] and scanning electron microscopy with polarization analysis (SEMPA) shows a resolution up to 5 nm [21], still far from the atomic scale. When STM and STS are used with a magnetic tip, they become a technique (SP-STM and SP-STS) that is able to study, at the atomic scale, the geometric structure as well as the electronic and magnetic properties of magnetic films at the same time. There are three ways to capture the magnetic information on surfaces. The first one would be the SP-STM, which produces a constant current topographic image. The theory of SP-STM was developed by Heinze and Blügel[22]. The weakness of SP-STM is that the magnetic information is mixed with other effects, as there may be a strong interaction between tip and sample. In the second method (SP-STS), introduced by Wiesendanger *et al* [23, 61], what you get is the derivative of current to voltage, dI/dV by modulating the voltage in the sample. If you choose a high enough voltage, you can exclude the interactions between the tip and the sample, and detect only the electronic structure and the magnetic properties. The third method is based on the second. The objects is to obtain more accurate quantitative results. It is to get the curve $I(V)$ as a function of voltage.

In the systems with *good* symmetry, in general, the magnetic moments would align parallelly (ferromagnetic) or antiparallelly (antiferromagnetic). But the materials in the real world inevitably contain various defects or impurities. Due to these imperfections, the configuration of magnetic moments will distort and align noncollinearly according to the corresponding geometrical or chemical imperfections, which leads to the magnetic frustration. During the past 25 years, much attention have been paid to the models of frustration [24]. The word “frustration” was introduced by G. Toulouse [25] and J. Villain [26] to describe the situation in which a spin (or a number of spin) can not find an orientation to fully satisfy all

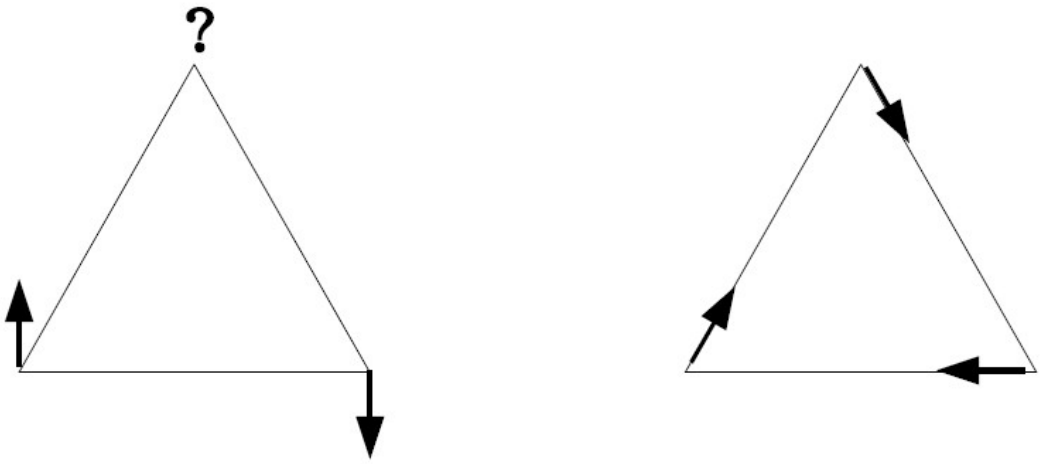

FIGURE 1.1: Example of an antiferromagnetic system with magnetic frustration (left). In the collinear framework, it is not possible to determine the orientation of the spin on the top of the triangle. A possible noncollinear configuration is given on the right figure.

the interactions with its neighboring spins. In general the frustration can result from geometrical or chemical reasons. In a geometrically frustrated system, the geometry of the lattice precludes the simultaneous minimization of all interactions. A typical example of the 2-dimensional antiferromagnetic triangle is shown in Figure 1.1, which shows a frustrated system because three neighboring spins cannot be pairwise antialigned. Indeed, if two spins on the vertices of the triangle align collinearly, the third one is impossible to comply with the collinearity. This problem can be solved if the spins are allowed to rotate until they feel good, that is, the energy is minimal. A possible noncollinear configuration is shown in the right panel of Figure 1.1. Another category of frustration could result from the change in local chemical environment. If an atom is removed or replaced by another kind of atom, the remaining atoms must respond to change their magnetic moments, which leads to noncollinearity.

The study of noncollinear magnetism of transition metals and its response to external magnetic fields is the aim of this thesis. The relevant studies in calculating magnetic structures in transition metals, but without external magnetic fields, have been the major topic in the PhD theses of R. Robles [27] and E. Martínez [28]. In their works, the systems they calculated included Cr clusters on Cu substrate, Fe clusters on Al substrate, Mn film on Fe substrate and Cr steps on

Fe substrate. In this study we extend the investigation of magnetic properties of transition metals to incorporate the interaction with external magnetic fields. Fe is typical ferromagnetic, and Cr is typical antiferromagnetic, the competition in their interface leads to magnetic frustration. Mn possesses very complex magnetic properties in nature, it also results in magnetic frustration. So in this study we choose two systems to investigate the evolution of frustrated magnetic structures under external magnetic fields: 6 Mn layers on fe substrate and Cr on a stepped Fe substrate.

In the theoretical side, we implement a semi-empirical tight-binding (TB) method, parameterized by a fit to the *ab initio* tight-binding linear muffin-tin orbitals method (TB-LMTO), to calculate the noncollinear magnetism. Compared to R. Robles and E. Martínez's method, a term corresponding to the interaction with external magnetic fields is introduced into the Hamiltonian. This method provides a possibility to calculate magnetic systems with relatively huge number of inequivalent sites, typically hundreds. Although several simplifications have been made in this method, the self-consistent calculation ensures relatively accuracy in our calculations. It may shed light on the nature of noncollinear magnetic systems under external magnetic fields and more applications, such as information storage devices, in other systems. Furthermore, the external magnetic field can be applied locally at each site in our TB method. Although at present it is not possible to apply so localized magnetic field in experiment at present, it also has theoretical meaning. And once so localized field can be obtained in experiment in the future, the storage density of storage devices could be increased drastically. In this work, we only consider uniform external magnetic fields.

The structure of this thesis is organized as follows. In chapter 2, we present a description of the theoretical method used to study electronic and magnetic properties in transition metals. Chapter 3 provides an application of this method in the system of 6 Mn layers supported on Fe substrate. Chapter 4 present another application in the system of an Cr monolayer on stepped Fe substrate and the cases with one to four Cr lines on this system. To conclude, Chapter 5 summarizes the thesis and gives perspectives for further study.

Chapter 2

Theoretical Method

2.1 Introduction

Electronic structure is one way connecting physical phenomena and theories in solid state physics. Once the electronic structure of a system is known, various mechanical, electronic, magnetic and optical properties of this system can be subsequently obtained. Currently, there are many methods to calculate electronic structures. The most widely employed methods are the so-called first principles or *ab initio* methods, which, understood from its name, provide an effective way to obtain electronic structures only with inputs of the geometry [1] and chemical composition of the system, no additional parameter is needed. The *ab initio* method are mostly based on the density functional theory (DFT) developed by P. Hohenberg and W. Kohn [29] and W. Kohn and L. J. Sham [30]. Among the advantages of this method, the notable ones are the accuracy of computation and the simplicity and essentiality of parameters. However, because of the requirement of symmetry of the considered system and the large consumption of computing

[1] mainly the lattice sturcture. Some programs can make geometrical optimization to obtain the lattice constant, such as CRYSTAL and VASP. Some programs do not make the calculation of relaxation, input of lattice constant is necessary to run the calculation, such as TB-LMTO.

power and memory, this method is not reasonable for the calculation of very complex systems[2]. An alternative category of methods of calculating the electronic structure is the semi-empirical methods, which are formulated from some simple physical ideas. Therefore, these methods are aimed to understand particular physical mechanisms. They need some parameters from experiments or from more basically first principle calculations. The accuracy depends on the suitability of the physical model and the accuracy of parameters. In many cases, the semi-empirical methods are designed to understand the qualitative, rather than the quantitative, properties of a particular phenomenon. Due to the simplification of theory in these methods, the computing power is considerably reduced with respect to the *ab initio* methods. And the release of the requirement of strict symmetry makes it possible to calculate complex structures with less symmetry. Another method of calculating electronic structures is the Green's function method whose strongpoint is to develop the properties of excited states [31, 32].

The tight-binding (TB) or linear combination of atomic orbitals [33, 34] (LCAO) method, which is a semi-empirical method, is a relatively effective and simple method to calculate electronic structure. This method has been used for a long time in the group of Valladolid led by Prof. Vega to investigate the magnetic properties of transition metals in various systems, including clusters, surfaces and interfaces, in either collinear framework or noncollinear framework. The parameters in the TB method are extracted from a fit to the *ab initio* TB-LMTO method developed by O. K. Andersen *et al* [35, 36]. In this thesis we use the TB method to consider the response of magnetic properties under external magnetic fields in the noncollinear framework, that is, the magnetic moments may rotate, rather than only reduce or enhance in magnitude, to comply with the change of external magnetic field.

[2]For nonsymmetrical systems, one could construct the supercell to enclose the nonsymmetrical structure. In this case, the whole space is fictitiously filled with infinite supercells, the system can be treated to be "symmetric", then the *ab initio* methods can be used. But the number of inequivalent sites in the supercells is normally large, which leads huge consumption of computing time.

In the following sections we briefly introduce the TB-LMTO method and simulate the systems containing surfaces and interfaces in this method. Then we derive the TB Hamiltonian in the noncollinear framework, introduce the self-consistent calculation process and finally analyze the parametrization.

2.2 TB-LMTO method

The TB-LMTO method is one of the methods that were derived from the original LMTO method, developed by O. K. Andersen[35]. It is an all-electron full-potential calculation approach, i.e., one considers the full potential of all atoms and all the electrons in the system. This is a first principles method within the DFT scheme, which has to solve the Kohn-Sham equation[30]. In this method, the whole space is divided into spheres centered around each atom (the so called muffin-tin spheres) and the remaining interstitial space among them. The potential of the system is different in both regions. In the interior areas of muffin-tin spheres,the potential varies strongly and is, in first approximation, spherical symmetric. In the interstitial areas, the potential varies very little and in first approximation is considered constant. The Hamiltonian is solved in both regions and interconnected by the boundary condition to obtain a valid solution in the whole space. The LMTO method uses the assumption that the basis set of wave functions depends on energy, but only in the first order, i.e., linear. Thus the equations are solved for some values of energy (band centers) and is an expression to first order of energy around the values chosen. The results will be much better as going closer to the band center. So the method is particularly suitable for the study of narrow bands, such as the d bands of transition metals.

If working with compact structures such as face-centered cubic (fcc) and body-centered cubic (bcc), the crystal potential has spherical symmetry not only in the proximity of the atoms, but also in the whole space. Therefore, the sphere approximation can be extended to the atomic sphere approximation (ASA). This approach replaces the muffin-tin spheres with Wigner-Seitz spheres, whose total

volume fills the whole system, i.e., the interstitial space is removed. This implies that there are narrow overlapping areas between adjacent atoms. The ASA is warranted only when the overlapping does not exceed a certain value, say, 16%[37].

To summarize, the TB-LMTO method is an LMTO method that uses the ASA approximation and works with a much more localized electronic distribution than in the original LMTO method. This method is both accurate (especially for narrow d bands of transition metals) and computationally very efficient.

2.2.1 Modelling surfaces and interfaces within TB-LMTO method

In this thesis we used the TB-LMTO method to calculate the parameters of systems that have a surface and an interface and also bulk systems. The TB-LMTO method was originally designed to deal with large solids with a periodic crystal structure in the three-dimensional space. In fact, this method works in the reciprocal space and therefore needs to move to the **k** space. As a DFT method, the precision of results depends on the number of **k** points that are used to perform the necessary integrations in the Brillouin zone. Transition metals have a very complex Fermi surface, so that the number of **k** points needed is particularly large. In all our calculations performed with TB-LMTO method to extract parameters the convergence has been achieved in the number of enough **k** points, i.e., an additional increase of **k** points does not appreciably change the results.

However, by means of the supercell we could enclose the structure of surfaces and interfaces in the supercell. Then the TB-LMTO method can be also used to simulate systems with surfaces and interfaces. As a building block the supercell is competed to construct a fictitious "periodic crystal". We illustrate the construction of the system with a surface and an interface by a diagram, shown in Figure 2.1. There are two points we need to pay attention. Firstly, in order to simulate the local environment of substrate, we design a mirror symmetric structure, in the center of which the atoms (marked with C) should carry essentially the same

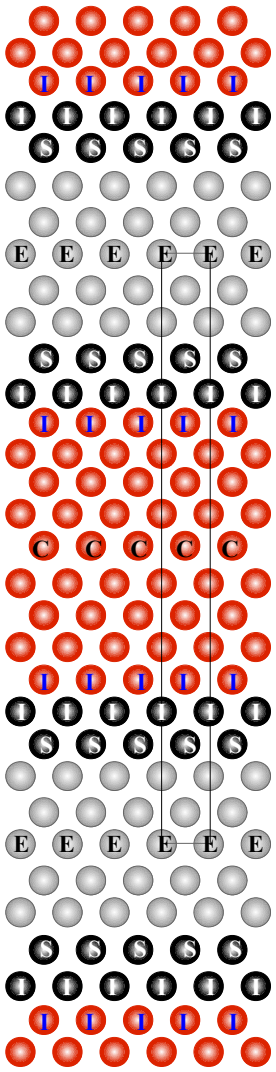

FIGURE 2.1: The schematic diagram for modelling a system with a surface and an interface in the TB-LMTO method. The red, black and grey circles represent the substrate atoms, deposited films and fictitious "empty atoms", respectively. The black lines enclose the supercell, which is repeated indefinitely in three directions of the space.

property of the ones in the pure crystal. There must be enough layers of substrate atoms to preserve this assumption. The atoms marked with I replicate the real interface between the substrate and the deposited film that contains a number of monolayers. Secondly, to achieve the aim of simulating the surface and to ensure that there is no interaction among supercells, we must introduce enough empty space between two blocks of atoms to prevent interaction among them. Within the ASA, the empty space is simulated by the so-called empty spheres, which are muffin-tin spheres without heart. Consider that this condition is met only when the charge in the central layer of empty spheres (marked with E) is negligible. A typical supercell to simulate the properties of substrate, interface and surface is enclosed by the black rectangle.

2.3 TB method

As a TB model, the general wave function of an electron is expressed by a linear combination of atomic orbitals located on the atom i with angular momentum $\alpha = (l, m)$ and spin $\sigma = (\uparrow, \downarrow)$:

$$|\Psi\rangle = \sum_{i\alpha\sigma} a_{i\alpha\sigma} |i\alpha\sigma\rangle. \tag{2.1}$$

The electron-electron interaction is formulated based on the Hubbard model, developed by J. Hubbard [38–41] to deal with electron correlations in narrow energy bands. With this Hamiltonian we subsequently generalize our model to the non-collinear framework and incorporate the interaction with external magnetic fields.

2.3.1 The collinear Hamiltonian

In the Hubbard model, the Hamiltonian is divided into two parts: the body term H_0 and the electron-electron interaction term H_I. We start from the Hamiltonian

expressed in the language of second quantization,

$$\begin{aligned} H &= \sum_{i,j}\sum_{\alpha,\beta,\sigma} T_{ij}^{\alpha\beta}\hat{c}_{i\alpha\sigma}^{\dagger}\hat{c}_{j\beta\sigma} + \frac{1}{2}{\sum_{i\alpha\sigma,j\beta\sigma'}}' U_{i\alpha\sigma,j\beta\sigma'}\hat{n}_{i\alpha\sigma}\hat{n}_{j\beta\sigma'}, \\ &\equiv H_0 + H_I, \end{aligned} \tag{2.2}$$

where

$$T_{ij}^{\alpha\beta} = \int \phi_{\alpha}^{*}(\mathbf{x}-\mathbf{R}_i)\left[-\frac{\hbar^2}{2m}\nabla^2 + V\right]\phi_{\beta}(\mathbf{x}-\mathbf{R}_j)d\mathbf{x}, \tag{2.3}$$

$$\begin{aligned} U_{i\alpha\sigma,j\beta\sigma'} &= (i\alpha\sigma, j\beta\sigma'|\frac{1}{r}|i\alpha\sigma, j\beta\sigma') \\ &= e^2\int \frac{|\phi_{\alpha\sigma}(\mathbf{x}-\mathbf{R}_i)|^2|\phi_{\beta\sigma'}(\mathbf{x}'-\mathbf{R}_j)|^2}{|\mathbf{x}-\mathbf{x}'|}d\mathbf{x}d\mathbf{x}', \end{aligned} \tag{2.4}$$

$\phi_{\alpha\sigma}(\mathbf{x}-\mathbf{R}_i)$ is the wave function of the state at atom i, orbital α and with spin σ. V represents the nuclear potential acting on the electrons together with the self-consistent potential due to electrons in other bands. $\hat{c}_{i\alpha\sigma}^{\dagger}$ ($\hat{c}_{i\alpha\sigma}$) is the creation (annihilation) operator of an electron on site i, orbital α and with spin σ. $U_{i\alpha\sigma,j\beta\sigma'}$ is the Coulomb integral, for terms with parallel spins $U_{\sigma\sigma} = U_{\uparrow\uparrow} = U_{\downarrow\downarrow}$, for terms with antiparallel spins $U_{\sigma\sigma'} = U_{\uparrow\downarrow} = U_{\downarrow\uparrow}$. The prime at the top right corner of the summation symbol stands for the terms with index $i = j, \alpha = \beta, \sigma = \sigma'$ are excluded.

Let

$$T_{ii}^{\alpha\alpha} = \int \phi_{\alpha}^{*}(\mathbf{x}-\mathbf{R}_i)\left[-\frac{\hbar^2}{2m}\nabla^2 + V\right]\phi_{\alpha}(\mathbf{x}-\mathbf{R}_i)d\mathbf{x} \equiv \varepsilon_{i\alpha}^{0} \tag{2.5}$$

be the energy of electron at atom i, orbital α, excluding the electron-electron interaction energy. And define the residual terms

$$T_{ij}^{\alpha\beta}|_{i\neq j} \equiv t_{ij}^{\alpha\beta}$$

to be the hopping integrals between an electron on site i, orbital α and an electron on site j, orbital β to represent the effect of electronic delocalization. To calculate these hopping integrals, we need a limited number of parameters regarding the Slater-Koster two-center approximation [48], and in general they only depend on

the considered material, the crystal packing and the distance between the considered atoms. Then the body term could be written as

$$H_0 = \sum_{i,\alpha,\sigma} \varepsilon^0_{i\alpha} \hat{n}_{i\alpha\sigma} + \sum_{i\neq j} \sum_{\alpha,\beta,\sigma} t^{\alpha\beta}_{ij} \hat{c}^\dagger_{i\alpha\sigma} \hat{c}_{j\beta\sigma}, \tag{2.6}$$

where $\hat{n}_{i\alpha\sigma} = \hat{c}^\dagger_{i\alpha\sigma}\hat{c}_{i\alpha\sigma}$ is the particle-number operator.

We next analyze the interaction term H_I with the help of the mean-field approximation (equivalent to the unrestricted Hartree-Fock approximations) which retains the main electronic correlation effects to accurately account for the itinerant magnetism in transition metals at $T = 0K$. To do this we introduce the identity

$$\hat{n}_i\hat{n}_j = (\hat{n}_i - \langle\hat{n}_i\rangle)(\hat{n}_j - \langle\hat{n}_j\rangle) + \hat{n}_i\langle\hat{n}_j\rangle + \hat{n}_j\langle\hat{n}_i\rangle - \langle\hat{n}_i\rangle\langle\hat{n}_j\rangle, \tag{2.7}$$

where $\langle\hat{n}_i\rangle$ is the average occupation of state i ($i \equiv i\alpha\sigma$). Substitute equation (2.7) into H_I, the interaction term becomes

$$\begin{aligned} H_{\mathrm{I}} &= H_{\mathrm{corr}} + \sum_{i\alpha\sigma} \Delta\varepsilon_{i\alpha\sigma}\hat{n}_{i\alpha\sigma} - \frac{1}{2}\sum_{i\alpha\sigma} \Delta\varepsilon_{i\alpha\sigma}\langle\hat{n}_{i\alpha\sigma}\rangle \\ &= H_{\mathrm{corr}} + \sum_{i\alpha\sigma} \Delta\varepsilon_{i\alpha\sigma}\hat{n}_{i\alpha\sigma} - E_{dc}. \end{aligned} \tag{2.8}$$

The term $\Delta\varepsilon_{i\alpha\sigma}$ represents the variation of energy levels of an electron on site i with orbital α, spin σ due to the Coulomb interaction, and is given by:

$$\Delta\varepsilon_{i\alpha\sigma} = {\sum_{j\beta\sigma'}}' U_{i\alpha\sigma,j\beta\sigma'}\langle\hat{n}_{j\beta\sigma'}\rangle. \tag{2.9}$$

The correction term E_{dc} is constant and has the form:

$$E_{dc} \equiv \frac{1}{2}\sum_{i\alpha\sigma} \Delta\varepsilon_{i\alpha\sigma}\langle\hat{n}_{i\alpha\sigma}\rangle. \tag{2.10}$$

The remaining term

$$H_{\text{corr}} = \frac{1}{2} \sum_{i\alpha\sigma, j\beta\sigma'}{}' U_{i\alpha\sigma, j\beta\sigma'} (\hat{n}_i - \langle \hat{n}_i \rangle)(\hat{n}_j - \langle \hat{n}_j \rangle) \tag{2.11}$$

accounts for the effect of electron correlation due to the fluctuation of electron number $n_{i\alpha\sigma}$ around its mean value $\langle \hat{n}_{i\alpha\sigma} \rangle$. Within the mean field approximation, it can be neglected. So we obtain the approximate Hamiltonian,

$$H = \sum_{i\alpha\sigma} \varepsilon_{i\alpha\sigma} \hat{n}_{i\alpha\sigma} + \sum_{i \neq j} \sum_{\alpha,\beta,\sigma} t_{ij}^{\alpha\beta} \hat{c}_{i\alpha\sigma}^{\dagger} \hat{c}_{j\beta\sigma} - E_{\text{dc}}, \tag{2.12}$$

where $\varepsilon_{i\alpha\sigma} = \varepsilon_{i\alpha}^{0} + \Delta\varepsilon_{i\alpha\sigma}$. These are the new energy levels, once we have added the term from the electron-electron interaction. This Hamiltonian describes the behavior of electrons as if each electron is an independent particle moving in an effective potential created by other. The mean-field approximation is valid for studying magnetic systems whose properties are measured at low temperature where electron fluctuation can be negligible. By referring to the quantity, this approach tends to overestimate the magnetic moment, since the effect of correlation is neglected here.

To make further approximation, we consider only the intra-atomic contributions U_{ii}, which are primarily responsible for the magnetic properties. Introduce the direct interaction term

$$U_{i\alpha\beta} = \frac{U_{i\alpha\uparrow, i\beta\uparrow} + U_{i\alpha\uparrow, i\beta\downarrow}}{2} \tag{2.13}$$

and the interchange terms

$$J_{i\alpha\beta} = U_{i\alpha\uparrow, i\beta\downarrow} - U_{i\alpha\uparrow, i\beta\uparrow}. \tag{2.14}$$

The term $\Delta\varepsilon_{i\alpha\sigma}$ could be written explicitly for different spins. If $\sigma = \uparrow$,

$$\Delta\varepsilon_{i\alpha\uparrow} = \sum_{\beta \neq \alpha} U_{i\alpha\uparrow, i\beta\uparrow} \langle \hat{n}_{i\beta\uparrow} \rangle + \sum_{\beta} U_{i\alpha\uparrow, i\beta\downarrow} \langle \hat{n}_{i\beta\downarrow} \rangle, \tag{2.15}$$

if $\sigma =\downarrow$,

$$\begin{aligned}\Delta\varepsilon_{i\alpha\downarrow} &= \sum_{\beta} U_{i\alpha\downarrow,i\beta\uparrow}\langle\hat{n}_{i\beta\uparrow}\rangle + \sum_{\beta\neq\alpha} U_{i\alpha\downarrow,i\beta\downarrow}\langle\hat{n}_{i\beta\downarrow}\rangle \\ &= \sum_{\beta} U_{i\alpha\downarrow,i\beta\uparrow}\langle\hat{n}_{i\beta\uparrow}\rangle + \sum_{\beta\neq\alpha} U_{i\alpha\uparrow,i\beta\uparrow}\langle\hat{n}_{i\beta\uparrow}\rangle. \end{aligned} \tag{2.16}$$

Using the analysis above, we obtain a compact form for the term $\varepsilon_{i\alpha\sigma}$,

$$\varepsilon_{i\alpha\sigma} = \varepsilon^0_{i\alpha} + \sum_{\beta} U_{i\alpha\beta}N_{i\beta} - z_\sigma\frac{1}{2}\sum_{\beta} J_{i\alpha\beta}\mu_{i\beta}, \tag{2.17}$$

where $z_\sigma = \begin{cases} 1, & \sigma =\uparrow, \\ -1, & \sigma =\downarrow, \end{cases}$, the electron number $N_{i\beta} = \langle\hat{n}_{i\beta\uparrow}\rangle + \langle\hat{n}_{i\beta\downarrow}\rangle = \langle\hat{n}_{i\beta}\rangle$, and the magnetic moment $\mu_{i\beta} = \langle\hat{n}_{i\beta\uparrow}\rangle - \langle\hat{n}_{i\beta\downarrow}\rangle$.

2.3.2 The noncollinear Hamiltonian

We extend our TB model to allow the calculation of noncollinear magnetic properties. To do this, the first step is to divide the collinear approximate Hamiltonian, expressed in equations (2.12) and (2.17), into a magnetic independent term H_{indep} and a magnetic dependent term H_{dep},

$$H = H_{indep} + H_{dep}, \tag{2.18}$$

where

$$\begin{aligned} H_{indep} &= \sum_{i\alpha\sigma}\left(\varepsilon_{i\alpha} + \sum_{\beta} U_{i\alpha\beta}\langle N_{i\beta}\rangle\right)\hat{n}_{i\alpha\sigma} + \sum_{i\neq j}\sum_{\alpha,\beta\sigma} t^{\alpha\beta}_{ij}\hat{c}^\dagger_{i\alpha\sigma}\hat{c}_{j\beta\sigma} \\ &= \sum_{i,j}\sum_{\alpha,\beta,\sigma}\left[\left(\varepsilon_{i\alpha} + \sum_{\gamma} U_{i\alpha\gamma}\langle N_{i\gamma}\rangle\right)\delta_{ij}\delta_{\alpha\beta} + (1-\delta_{ij})t^{\alpha\beta}_{ij}\right]\hat{c}^\dagger_{i\alpha\sigma}\hat{c}_{j\beta\sigma} \end{aligned} \tag{2.19}$$

$$H_{dep} = \sum_{i\alpha\sigma}\left(-\frac{1}{2}\sum_{\beta} J_{i\alpha\beta}\mu_{i\beta}\right) z_\sigma\hat{n}_{i\alpha\sigma}. \tag{2.20}$$

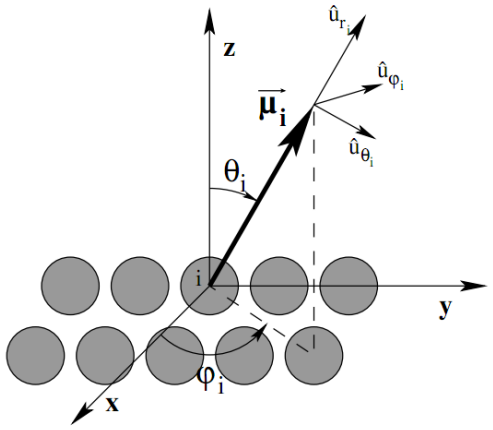

FIGURE 2.2: The local coordinate system on site i with magnetic moment μ_i.

Next we rewrite the Hamiltonian in the spinor space, with the basis for spin-up $\sigma_\uparrow = \begin{pmatrix} 1 \\ 0 \end{pmatrix}$ and for spin-down $\sigma_\downarrow = \begin{pmatrix} 0 \\ 1 \end{pmatrix}$,

$$H_{indep} = \sum_{\substack{i,j \\ \alpha,\beta}} \left[\left(\varepsilon_{i\alpha} + \sum_{\beta} U_{i\alpha\beta} \langle N_{i\beta} \rangle \right) \delta_{ij}\delta_{\alpha\beta} + (1-\delta_{ij}) t_{ij}^{\alpha\beta} \right] \hat{c}_{i\alpha}^{\dagger} \hat{c}_{j\beta} \begin{pmatrix} 1 & 0 \\ 0 & 1 \end{pmatrix} \quad (2.21)$$

$$H_{dep} = \sum_{i\alpha} \left(-\frac{1}{2} \sum_{\beta} J_{i\alpha\beta} \mu_{i\beta} \right) \hat{n}_{i\alpha} \begin{pmatrix} 1 & 0 \\ 0 & -1 \end{pmatrix}. \quad (2.22)$$

This Hamiltonian is valid for collinear systems, where all magnetic moments are parallel or antiparallel. However, in general cases noncollinearity may exist, then we have a local spin-quantization axis, which is different in each site i (shown in Fig. 2.2). The alternative is to rotate the global axis $\{\mathbf{x}, \mathbf{y}, \mathbf{z}\}$ to the local axis $\{\varphi_\mathbf{i}, \theta_\mathbf{i}, \mathbf{r_i}\}$ which differ in each local site. The local axis is referred to a unique basis for the whole system, and all the local quantities are expressed in their corresponding local spherical coordinate.

The magnetic independent term H_{indep} by its nature keeps unchanged, while the magnetic dependent term H_{dep} must rotate to the local axis on each site. This rotation can be decomposed into two steps: a rotation of angle θ_i around axis $\mathbf{y}$, followed a rotation of angle φ_i around axis $\mathbf{z}$. Using the representation of Pauli

Matrices

$$\sigma_0 = \begin{pmatrix} 1 & 0 \\ 0 & 1 \end{pmatrix}, \sigma_x = \begin{pmatrix} 0 & 1 \\ 1 & 0 \end{pmatrix}, \sigma_y = \begin{pmatrix} 0 & -i \\ i & 0 \end{pmatrix}, \sigma_z = \begin{pmatrix} 1 & 0 \\ 0 & -1 \end{pmatrix}, \quad (2.23)$$

the rotation matrix on site i is described by

$$R_i = R_z(\varphi_i)R_y(\theta_i) = \exp\left(-i\frac{\varphi_i}{2}\sigma_z\right)\exp\left(-i\frac{\theta_i}{2}\sigma_y\right) = \begin{pmatrix} \cos\frac{\theta_i}{2} & e^{-i\varphi_i}\sin\frac{\theta_i}{2} \\ e^{i\varphi_i}\sin\frac{\theta_i}{2} & -\cos\frac{\theta_i}{2} \end{pmatrix}. \quad (2.24)$$

Under this local axis rotation, the magnetic dependent term H_{dep} in noncollinear framework reads

$$\begin{aligned} H_{dep} &= \sum_{i\alpha}\left(-\frac{1}{2}\sum_{\beta}J_{i\alpha\beta}\mu_{i\beta}\right)\hat{n}_{i\alpha}R_i\begin{pmatrix} 1 & 0 \\ 0 & -1 \end{pmatrix}R_i^{\dagger} \\ &= \sum_{i\alpha}\left(-\frac{1}{2}\sum_{\beta}J_{i\alpha\beta}\mu_{i\beta}\right)\hat{n}_{i\alpha}\begin{pmatrix} \cos\theta_i & e^{-i\varphi_i}\sin\theta_i \\ e^{i\varphi_i}\sin\theta_i & -\cos\theta_i \end{pmatrix}. \end{aligned} \quad (2.25)$$

2.3.3 The interaction with an external magnetic field

We next introduce directly the interaction term H_{Bext} with external magnetic field in the noncollinear framework,

$$H_{Bext} = -\sum_{i,\alpha}\frac{g_s\mu_B}{\hbar}\overrightarrow{B}_i\cdot\overrightarrow{S}_i\hat{n}_{i\alpha}, \quad (2.26)$$

where $g_s = 2$ is the gyromagnetic factor, $\hbar$ is the Planck constant and μ_B is the Bohr magneton. $\overrightarrow{S}_i = \frac{1}{2}\hbar\overrightarrow{\sigma}$ is the local spin angular moment. Using the Pauli matrices again, this interaction term is described in the matrix form,

$$H_{Bext} = -\frac{1}{2}g_s\mu_B\sum_{i,\alpha}\hat{n}_{i\alpha}\begin{pmatrix} B_i^z & B_i^x - iB_i^y \\ B_i^x + iB_i^y & -B_i^z \end{pmatrix}. \quad (2.27)$$

Now we obtain the desired Hamiltonian in the noncollinear framework with the interaction of an external magnetic field, which comprises the three terms described

in equations (2.21), (2.25) and (2.27), respectively. It is worthwhile to emphasize that our model allows the study for the cases that a local external magnetic field is applied, which can be seen in equation (2.27) that the magnetic field $\overrightarrow{B}_i$ depends on local site i. Despite that no such tiny localized magnetic field can be produced in practice, our method could be used to study localized magnetic properties up to the atomic resolution, which may be possible in the future. In this thesis we only deal with the case of a uniform external magnetic field applied along the z axis.

2.3.4 Treatment of the charge: global charge neutrality vs. local charge neutrality

At this stage we should deal with the term given in equation (2.17), which involves the charge in the system, and now we treat the charge in 2 different approximations. The total charge in the system must be constant, so that the immediate result we could draw is to require that the total charge of the entire system at the end of calculation is equal to the total charge that we had at the beginning of calculation. This is called the global charge neutrality (GCN). However, there are situations in which the charge transfer is difficult to analyze and may lead to non-physical results. It is, therefore, necessary to take special care of it and ensure as far as possible, that the charge transfer is correct. This can be achieved in two ways. On the one hand, without getting rid of the GCN, we analyze all the causes of charge transfer and make a complete consideration of the charge in an overall point of view. Another way is to use the local charge neutrality (LCN) approximation. This approach assumes that there is no charge transfer between atoms in the system, so that the charge in each atom keeps constant throughout the calculation process. We know from various *ab initio* calculations that the charge transfer in transition metals is small and therefore the error relative to the physical requirement of GCN is small too. Furthermore, we could minimize this error if we take account of a reference charge distribution that is as similar as possible to the real distribution in the system that we wish to study.

2.3.4.1 Global charge neutrality

Consider the global charge neutrality in equation (2.17), the charge transfer is governed by the direct interaction term $U_{i\alpha\sigma}$ and the total value of charge is preserved by moving the Fermi level. However, as explained above, the GCN may give some non-physical results of the charge transfer. To improve the results, we must analyze what are the origins of charge transfer. In general, the charge transfer occurs when the atoms in the systems having asymmetric local environment. This may occur for geometrical reasons, when the number or position of neighbors of an atom differs from the perfect crystal structure, or chemical causes, when the chemical nature of neighbors of an atom is changed. In the systems with low dimensional interfaces or surfaces, such as those studied in this thesis, we have both effects.

As for the geometrical reasons, the main source of error is the use of a uniform energy level $\varepsilon^0_{i\alpha}$ for all atoms of the same elements, regardless of their local environment. However, in a solid the crystal field potential is produced by the local environment and varies in different sites. In first approximation, the crystal field potential depends on the number of neighbors (coordination). We express this approximation explicitly in the energy level,

$$\varepsilon^0_{i\alpha} = \varepsilon^{0,at}_{i\alpha} + Z_i\xi_{i\alpha}, \tag{2.28}$$

where $\varepsilon^{0,at}_{i\alpha}$ is the energy level for the isolated atom excluding the electron-electron interaction and $Z_i\xi_{i\alpha}$ is the crystal field potential, being Z_i the coordination of the atom i and $\xi_{i\alpha}$ is a potential which depends on the orbital character and element considered. The final expression of the energy level in our approximation made in the GCN reads

$$\varepsilon_{i\alpha\sigma} = \varepsilon^{0,at}_{i\alpha} + Z_i\xi_{i\alpha} + \sum_\beta U_{i\alpha\beta}N_{i\beta} - z_\sigma\frac{1}{2}\sum_\beta J_{i\alpha\beta}\mu_{i\beta}. \tag{2.29}$$

With this approximation a great adaptability of environment is achieved, since the charge transfer is regulated by the variation of the crystal field.

Regarding the chemical causes, we have shown that it occurs in the systems where there is an interface between two (or more) elements. In our treatment we try to minimize the error by a careful choice of all parameters involved in the calculation, as we will see later.

2.3.4.2 Local charge neutrality

In practice, some calculations [42–44] take into account the LCN approximation, which is to fix the electron charge distribution of a physical system to a system which has a "static" reference charge distribution $N_{i\alpha}^{ref}$ and reference coordination Z_i^{ref}, being without charge transfer. For transition metals, the charge transfer between different atoms is small, so both the GCN approach and the LCN approach are in principle valid. Starting from the equation (2.29) obtained for the GCN and considering a reference system with charges $N_{i\alpha}^{ref}$ and coordinations Z_i^{ref}, we have

$$\begin{aligned}
\varepsilon_{i\alpha\sigma} &= \varepsilon_{i\alpha}^{0,at} + Z_i\xi_{i\alpha} + \left(Z_i^{ref}\xi_{i\alpha} - Z_i^{ref}\xi_{i\alpha}\right) + \sum_\beta U_{i\alpha\beta}N_{i\beta} \\
&\quad + \left(\sum_\beta U_{i\alpha\beta}N_{i\beta}^{ref} - \sum_\beta U_{i\alpha\beta}N_{i\beta}^{ref}\right) - z_\sigma\frac{1}{2}\sum_\beta J_{i\alpha\beta}\mu_{i\beta} \qquad (2.30)\\
&\equiv \varepsilon_{i\alpha}^{0,ref} + \Delta Z_i\xi_{i\alpha} + \sum_\beta U_{i\alpha\beta}\Delta N_{i\beta} - z_\sigma\frac{1}{2}\sum_\beta J_{i\alpha\beta}\mu_{i\beta},
\end{aligned}$$

where

$$\varepsilon_{i\alpha}^{0,ref} = \varepsilon_{i\alpha}^{0,at} + Z_i^{ref}\xi_{i\alpha} + \sum_\beta U_{i\alpha\beta}N_{i\beta}^{ref}, \qquad (2.31a)$$

$$\Delta Z_i\xi_{i\alpha} = \left(Z_i - Z_i^{ref}\right)\xi_{i\alpha}, \qquad (2.31b)$$

$$\sum_\beta U_{i\alpha\beta}\Delta N_{i\beta} = \sum_\beta U_{i\alpha\beta}\left(N_{i\beta} - N_{i\beta}^{ref}\right). \qquad (2.31c)$$

The term $\varepsilon_{i\alpha}^{0,ref}$ is derived directly from the reference system. The term (2.31c) is zero by requiring LCN ($\Delta N_{i\alpha} = 0, \forall i, \alpha$), which is achieved by introducing the potentials $\Omega_{i\alpha}$, which vary in the self-consistent calculation so that the charge is the desired one. These potentials are also introduced in the term (2.31b), that

gives the difference of the crystal field between the considered system and the reference. The origin of these potentials can also be understood in an intuitive way: in general the charge transfer is largely governed by the direct interaction term $U_{i\alpha\beta}$. The requirement of no charge transfer is equivalent to working in the limit ($U_{i\alpha\beta} \to \infty$). Multiplying $U_{i\alpha\beta}$ by $\Delta N_{i\alpha}$ (which is zero), we obtain an uncertainty, which could be explained to be the potential $\Omega_{i\alpha}$.

In practice we also block the charge transfer between orbitals s (p) and d, therefore this requires that $N_{is} + N_{ip} = N_{is}^{ref} + N_{ip}^{ref}$ and $N_{id} = N_{id}^{ref}$. However the charge transfer between orbitals s and p and between d is allowed, which means that only two different potentials $\Omega_{i(sp)}$ and $\Omega_{i(d)}$ are necessary. This takes into account the different nature of the s and p electrons, delocalized, and d electrons, localized, with a bandwidth of about 5 eV.

With this requirement, the expression for the energy levels within the LCN approximation is written as

$$\varepsilon_{i\alpha\sigma} = \varepsilon_{i\alpha}^{0,ref} + \Omega_{i\alpha} - z_\sigma \frac{1}{2} \sum_\beta J_{i\alpha\beta}\mu_{i\beta}. \tag{2.32}$$

The LCN approximation, on the one hand, provides an easy way to regulate the charge transfer in the system, on the other hand it has two major disadvantages. One has already been mentioned: it prevents charge transfer. We have already seen that the error can be minimized in the systems we deal with in which the absence of charge transfer does not cause serious effect. The other disadvantage is that it adds an extra difficulty for the convergence, since the requirement of no charge transfer is very strict and the search for reference system is complex. Normally the convergence can be solved in an appropriate manner by varying the potential $\Omega_{i\alpha}$ iteration by iteration, but in specific cases the convergence is very industrious and usually requires a great number of iterations to achieve compared to the GCN approach. In this thesis, for noncollinear study the convergence is extremely slow and difficult, making it impossible to achieve in practice with LCN, so we employed the GCN approach.

2.3.5 The calculation of energy

To calculate the total energy of the system, we start from the band energy obtained from the self-consistent calculation and correct it with the correction term E_{dc}. The total energy reads

$$E_T = E_{bnd} - E_{dc}, \tag{2.33}$$

where the band energy is obtained by integrating the local density of states $\rho_{i\alpha\sigma}$ with the weight of energy ε up to the Fermi level ε_F,

$$E_{bnd} = \sum_{i\alpha\sigma} \int_{-\infty}^{\varepsilon_F} \varepsilon \rho_{i\alpha\sigma}(\varepsilon) d\varepsilon. \tag{2.34}$$

The term E_{dc} corrects the double counting of energy. Thus, taking into account the expression of E_{dc} in equation (2.17),

$$E_{dc} = \frac{1}{2} \sum_{i\alpha\beta} U_{i\alpha\beta} N_{i\alpha} N_{i\beta} - \frac{1}{4} \sum_{i\alpha\beta} J_{i\alpha\beta} \mu_{i\alpha} \mu_{i\beta}. \tag{2.35}$$

The first part of this expression represents the electrostatic interaction and the second the magnetic interaction. This expression is valid in the case of GCN. For LCN approximation, it is expressed as follows,

$$E_{dc} = \frac{1}{2} \sum_{i\alpha} \Omega_{i\alpha} N_{i\alpha} - \frac{1}{4} \sum_{i\alpha\beta} J_{i\alpha\beta} \mu_{i\alpha} \mu_{i\beta}. \tag{2.36}$$

Although it is clear to calculate the total energy from above equations, we have to emphasize that the energy calculated is purely from the electronic part. The remainder of the total energy should be calculated externally. It is also important to note that we will use a relative form of energy to compare different configurations of a magnetic system. Therefore, we could predict the most stable electron configuration in our model.

2.3.6 Self-consistent calculation

To solve the Hamiltonian we can follow two different ways. One is to solve an eigenvalue problem: diagonalizing the Hamiltonian to obtain the eigenvalues and eigenvectors, from which the demanded physical quantity can be computed. The problem of this method is that in a semi-infinite system with a large number of inequivalent atoms, the computing time needed is very long. In this thesis we use an alternative method to circumvent the intricate diagonalization process, this is the recursion method (for details, see Appendix A) proposed by R. Haydock [45–47]. The recursion method gives directly the local density of states (LDOS) that is proportional to imaginary part of the Green's function,

$$\rho_{i\alpha\sigma} = -\frac{1}{\pi} \lim_{\eta \to 0^+} \mathrm{Im} \langle i\alpha\sigma | G(\varepsilon + i\eta) | i\alpha\sigma \rangle. \tag{2.37}$$

Within the GCN, the Fermi level ε_F is computed by integrating all the LDOS up to a certain value of energy to obtain the total charge N_T,

$$\int_{-\infty}^{\varepsilon_F} \sum_{i\alpha\sigma} \rho_{i\alpha\sigma}(\varepsilon) d\varepsilon = N_T. \tag{2.38}$$

Once the LDOS and Fermi level is known, the local average occupation is obtained,

$$\langle \hat{n}_{i\alpha\sigma} \rangle = \int_{-\infty}^{\varepsilon_F} \rho_{i\alpha\sigma}(\varepsilon) d\varepsilon, \tag{2.39}$$

from which we compute the local magnetic moment, $\mu_{i\alpha} = \langle \hat{n}_{i\alpha\uparrow} \rangle - \langle \hat{n}_{i\alpha\downarrow} \rangle$.

In the case of LCN, the iterative process is performed as follows. We start from an initially proposed local magnetic moment $\mu_{i\alpha}$ and a potential $\Omega_{i\alpha}$, from which the Hamiltonian can be formulated. Using equation (2.37), we compute a new moment $\mu'_{i\alpha}$ and then a new potential $\Omega'_{i\alpha}$, which continue the iterative process.

The process ends when the convergence conditions are fulfilled,

$$\max_i \left\{ |N_{i(sp)} - N_{i(sp)}^{ref}|, |N_{id} - N_{id}^{ref}| \right\} < \delta, \tag{2.40a}$$

$$\max_{i\alpha} |\mu_{i\alpha} - \mu'_{i\alpha}| < \delta, \tag{2.40b}$$

$$\max_i |E_i^T(n) - E_i^T(n-1)| < \delta \tag{2.40c}$$

where $N_{i(sp)} = N_{is} + N_{ip}$ and $E_i^T(n)$ is the total energy in the nth-iteration. Here δ is a constant given to measure the convergence.

The determination of convergence is similar in the case of GCN, except that there is no potential $\Omega_{i\alpha}$. The convergence is achieved when the following conditions are satisfied,

$$\max_{i\alpha} |N_{i\alpha} - N'_{i\alpha}| < \delta, \tag{2.41a}$$

$$\max_{i\alpha} |\mu_{i\alpha} - \mu'_{i\alpha}| < \delta, \tag{2.41b}$$

$$\max_i |E_i^T(n) - E_i^T(n-1)| < \delta \tag{2.41c}$$

The above discussion is implemented for the case of collinearity. In the non-collinear framework, however, the determination of convergence is a little more complicated, since the direction of magnetic moments might be changed in the iterative process. Suppose the magnitude of the initially proposed magnetic moment is $\mu_i = \mu_{is} + \mu_{ip} + \mu_{id}$ and the direction is determined by the angles θ_i and φ_i in the spherical coordinates, so that the initial magnetic moment is $\overrightarrow{\mu}_i = \mu_{r_i}\hat{u}_{r_i}$, where $\hat{u}_{r_i}$ is the unit vector in the radial direction. Substituting these values into the Hamiltonian and solving the LDOS, we obtain a new magnetic moment, expressed in the "old" local coordinate system,

$$\overrightarrow{\mu}'_i = \mu'_{r_i}\hat{\mu}_{r_i} + \mu'_{\theta_i}\hat{\mu}_{\theta_i} + \mu'_{\varphi_i}\hat{\mu}_{\varphi_i}. \tag{2.42}$$

The magnitude of the new magnetic moment can be obtained by

$$\mu'_i = \sqrt{(\mu'_{r_i})^2 + (\mu'_{\theta_i})^2 + (\mu'_{\varphi_i})^2}. \tag{2.43}$$

In order to ensure that the new magnetic moment is close enough to the former one, both in magnitude and in direction, except for the the restriction on total charge (2.41a) and total energy (2.41c), the convergence condition for local magnetic moment (2.41b) should be replaced by

$$\max_i |\mu_i - \mu_i'| < \delta, \tag{2.44a}$$

$$\max_i \left\{ |\mu_{\theta_i}'|, |\mu_{\varphi_i}'| \right\} < \delta. \tag{2.44b}$$

As the magnetic properties in transition metals are mainly explained by d electrons, for simplicity we neglect the contribution of s and p electrons in our self-consistent procedure.

2.3.7 Parametrization

The suitability of parameters in our semi-empirical TB method is vital for the accuracy of the results obtained in the self-consistent procedure. There are two facts we should take into account. On the one hand it is more convenient to achieve the maximum possible transferability of parameters in different systems. For example, we may wish to use the same parameters in clusters, surfaces and interfaces for the same elements. On the other hand, however, we also desire to find a set of parameters that can produce results as accurate as possible in a specific system. In general, as we have noted in the description of the TB method, this method is often designed to study a specific physical phenomenon, so that the accuracy of results is model-dependent and the transferability of parameters is weak. Therefore, no perfect tradeoff lies between the two sides. In practice, we could make a compromise between these two considerations to get sufficiently accurate quantitative results, but without losing adequate transferability in certain similar systems.

Depending on the different treatments of charge in the system, say, LCN or GCN, we have to consider different sets of parameters. For the LCN, we need the

reference energy level $\varepsilon_{i\alpha}^{0,ref}$ and the hopping integrals $t_{ij}^{\alpha\beta}$ which are derived from the same reference system. The interchange interaction $J_{i\alpha\beta}$ are extracted by a fit of magnetic moment to the the values calculated by other methods or obtained in experiments. In the case of GCN, the value of local charges is not so crucial as in the LCN case, because the charge is redistributed between different atoms and orbitals, only fulfilling the requirement that the total charge in the system is constant. The hopping integrals $t_{ij}^{\alpha\beta}$ and interchange interactions $J_{i\alpha\beta}$ are the same as those in the LCN. The remaining parameters need to include the direct interaction $U_{i\alpha\beta}$, the energy level $\varepsilon_{i\alpha}^{0,at}$ and the crystal field potential $\Omega_{i\alpha}$, which are universal for each element in different systems. Next we analyze the parameters one by one.

Band centers and hopping integrals

The hopping integrals $t_{ij}^{\alpha\beta}$ describe the electron delocalization. They are parameters that fix the shape of the density of states. In this thesis we only consider the contributions of first and second neighbors and use the method proposed by Slater and Koster [48]. In essence, this method is to write the integrals of spherical symmetric potential centered on atoms i and j as a linear combination of two-center integrals. These integrals, which we call the Slater-Koster integrals, are taken as parameters. They depend on, in addition to the element considered, the distance between atoms i and j and the chemical environment.

Regarding the dependence on the distances between atoms, we take the Slater-Koster integrals in the system in which the distances between atoms are similar to those in reference system. In the case of deviation from the reference, Harrison [49] suggested a scale law to correct the dependence on the distances, which was also used by Andersen *et al* [50, 51]. The dependence on the distances between two atoms is proportional to $R_{ij}^{-(l+l'+1)}$, where l and l' are the angular quantum numbers associated with orbitals α and β, and R_{ij} is the distance between atoms i and j. This fit has been proved to give very good results when the deviation of the distances is less than 5% compared to the reference system [52].

The Slater-Koster integrals are calculated as follows. At first, using a first-principles method, the band structure of a system is calculated. Then the integrals are adjusted until the same band structure calculated before is reproduced. There are two ways to do this. The first one is developed by Papaconstantopoulos [52]. He has made the adjustment for 53 elements in the periodic table. These adjustments, being successfully used in several papers (see, for example, [42] or [43]), allow extracting parameters in any system that can be dealt with by the TB-LMTO method. With this procedure we can obtain the hopping integrals for the system with an similar environment to the reference, taking into account both the geometric and chemical environments.

In this work, we use another method proposed by Andersen *et al* [53] to study surfaces and interfaces of transition metals, which is based on the fact that the TB-LMTO Hamiltonian can be written in a first order approximation as

$$\overline{H}^{(1)} = \overline{C} + \overline{\Delta}^{\frac{1}{2}} \overline{S} \overline{\Delta}^{\frac{1}{2}}, \tag{2.45}$$

where $\overline{S}$ is the screened-structured canonical matrix. $\overline{C}$ and $\overline{\Delta}$ are diagonal matrices. This Hamiltonian has the same form as the TB Hamiltonian. The matrix $\overline{S}$ can be written in the same way as the hopping integrals, obtaining the canonical Slater-Koster integrals. Their values are shown in Table 2.1. In this thesis, the systems considered are all with bcc structure, so only the parameters with bcc structure are used. The fcc ones are also listed, which are needed when fcc systems are considered.

To find the $\overline{C}$ and $\overline{\Delta}$ matrices, we use the following relation [53]:

$$\frac{\overline{\Delta}^{\frac{1}{2}}}{\Delta^{\frac{1}{2}}} = \frac{\overline{C} - E_\nu}{C - E_\nu} = 1 - \left(Q - \overline{Q}\right) \frac{C - E_\nu}{\Delta}. \tag{2.46}$$

The terms C, Δ, Q and E_ν are potential parameters, selfconsistent, and are obtained directly after the TB-LMTO calculation. The terms remaining to obtain the Slater-Koster integrals are the $\overline{Q}$ parameters, whose values are $\overline{Q}_s = 0,3485$, $\overline{Q}_p = 0,05303$ and $\overline{Q}_d = 0,010714$ [53].

(eV)	bcc		fcc	
ss_0	3.093		3.053	
pp_0	2.787		2.742	
$dd_0(E_g)$	1.299		1.674	
$dd_0(T_{2g}$	2.710		2.366	
	1th	2nd	1th	2nd
$ss\sigma$	-0.593	-0.203	-0.484	-0.020
$sp\sigma$	-1.178	-0.435	-0.983	-0.038
$sd\sigma$	-1.417	-0.603	-1.256	-0.062
$pp\sigma$	2.356	0.935	2.001	0.092
$pp\pi$	-0.356	-0.048	-0.255	0.003
$pd\sigma$	2.926	1.289	2.574	0.141
$pd\pi$	-0.825	-0.134	-0.603	0.006
$dd\sigma$	-3.839	-1.757	-3.459	-0.226
$dd\pi$	1.887	0.364	1.415	-0.023
$dd\delta$	-0.271	-0.049	-0.058	-0.011

TABLE 2.1: Canonical Slater-Koster integrals.

We can make a TB-LMTO calculation to produce a set of potential parameters (C, Δ, Q, E_ν) for each inequivalent site in the system which is simulated by TB-LMTO described in section 2.2.1. Using this method, we could obtain parameters for surfaces and interfaces, which pertain to their local environment.

Finally, there remains the choice of band centers $\varepsilon_{i\alpha}^{ref}$ within the LCN approximation. This choice is made together with the determination of the Slater-Koster integrals. Their physical meaning is, as their name suggests, marking the position of the band center. They are also very important parameters since the change of relative position will change the hybridization between bands, and therefore the electronic and magnetic properties.

Direct and exchange interactions

The direct interaction contains a set of universal parameters which only depend on the element considered. For simplicity, we omit the differences between s and p orbitals, that is, we use the approximation $U_{iss} = U_{isp} = U_{ipp}$ and $U_{isd} = U_{ipd}$. The relation between the remaining three independent parameters $(U_{iss}, U_{isd}, U_{idd})$ for each element is taken from Hartree-Fock calculations for isolated atoms (see ref [54]). The absolute value of U_{idd} is estimated as the level shift due to a jump

(eV)	Fe	Mn	Cr
U_{iss}	1.77	1.60	1.47
U_{isd}	2.18	2.10	1.90
U_{idd}	5.44	4.80	4.22

TABLE 2.2: Direct interaction parameters (Coulomb integrals) for Fe, Mn and Cr.

of d electron of an atom to its nearest neighbor [55, 56]. With these efforts we obtain the values for the direct interaction of various transition metals studied in this thesis, shown in Table 2.2.

The determination of the exchange interaction terms $J_{i\alpha\beta}$ differs from that of the direct interaction. The physical meaning of this interaction is very important because it controls the expansion of the bands of majority and minority spins, and thus the magnetic properties. In fact, only for values above a certain value for $J_{i\alpha\beta}$, we have magnetism in the system[3]. We can find a value of the exchange for an certain element which maintains a high precision and is as transferable as possible in all types of environments. Furthermore, we only consider the parameter for d electrons, i.e., only J_{idd} is nonzero, because d electrons are responsible for most of the magnetic properties in transition metals. In fact, the values for the terms corresponding to s and p electrons are negligible compared to d electrons. However, this does not mean that the s and p electrons do not have an influence on the magnetic properties, whereas they have, despite their influence is small. It could be expected in two ways: on the one hand, the sp-d hybridization modifies the d band, therefore the electronic structure. Furthermore, the magnetic moment of the d band that produces an external field to polarize s and p bands, thereby also contributing to the magnetic moment directly.

Bare energy levels and crystal field parameters

[3]Within the Stoner model for itinerant magnetism, this condition is called the Stoner criterion. When the value of the exchange is greater then the inverse of the density of states at the Fermi level $J > \frac{1}{N_0(\varepsilon_F)}$, the system is ferromagnetic. Despite that the Stoner model of ferromagnetism is just a simple model, this approach is valid for any system of transition metals at zero temperature.

The bare energy level $\varepsilon_{i\alpha}^{0,at}$ and crystal field potential $\xi_{i\alpha}$ are involved in the NGC approximation. According to their definitions, they are values that only depend on the specific element and orbital. Therefore, the determination of these parameters must be unique for each element. To realize this, we make TB-LMTO calculations in different structures, to take samples of atoms with different number of coordination. Through the method described above we obtain the reference band centers $\varepsilon_{i\alpha}^{0,ref}$, using the equation (2.31a),

$$\varepsilon_{i\alpha}^{0,ref} = \varepsilon_{i\alpha}^{0,at} + Z_i^{ref}\xi_{i\alpha} + \sum_{\beta} U_{i\alpha\beta}N_{i\beta}^{ref}, \tag{2.31a}$$

which results in three equations (for s, p and d orbitals) per site. The number of coordination could vary in a large range (between the corresponding isolated atom and the bulk). We then make a fit by the least square method in various situations of coordination to obtain the values we want. They are the isolated energy levels $(\varepsilon_{is}^{0,at}, \varepsilon_{ip}^{0,at}, \varepsilon_{id}^{0,at})$ and the crystal field potentials $(\xi_{is}, \xi_{ip}, \xi_{id})$.

The remaining variables that appear in equation (2.31a) are already known: the coordinations Z_i, which are calculated simply by counting the number of neighbors[4], the direct interactions $U_{i\alpha\beta}$, which have been estimated in the previous section, and the charge distributions $(N_{is}^{ref}, N_{ip}^{ref}, N_{id}^{ref})$, which are derived from TB-LMTO calculations. It should be pointed out that the charge distributions must be extracted from the TB-LMTO calculation of the system that has similar (or identical) local environment to the system we study.

So far, we have described our TB method that is parametrized by *ab initio* TB-LMTO calculations and solved self-consistently using Haydock's recursion method. Next, we show the application of this model in transition metal systems, which contain surfaces and interfaces, in the following chapters.

[4]In this case it was decided to give some weight to second neighbors, namely 10% by weight of the former.

Chapter 3

Mn Film Supported on Fe Substrate

3.1 Introduction

The interface between ferromagnetic and antiferromagnetic materials is important in a scientific point of view because the competition between ferromagnetic and antiferromagnetic interactions can lead to very complex magnetic solutions, particularly when there are frustrations, either geometrical or chemical, in the system. When an antiferromagnetic film is deposited on a substrate with a ferromagnetic monoatomic step, the magnetic frustration around this defect can cause interesting magnetic configurations, as in prototype systems such as Fe and Cr studies by Vega *et al* [57], Stoeffler *et al* [58] and Berger *et al* [59, 60]. Due to the localized nature of the frustration, it is not possible to experimentally characterize the local magnetic configurations of frustrated systems in the atomic scale until the introduction of techniques such as SP-STM and SP-STS [22, 61, 62, 119]. The properties at the interface between magnetic materials are related to exchange coupling between layers [63, 64], giant magnetoresistance [65, 66] and the systems of spin valves [67].

Mn thin films grown on substrates of Fe(001) are one of the most interesting system to study both in experiment [68–72, 123, 124] and theory [73–75], since they have quite peculiar configurations due to the complex nature of Mn in the point of view of magnetism and the possible geometric asymmetries. The interest in this system also comes from the fact that Fe is a typical ferromagnetic material, and it is expected that the structures with low dimensionality of Mn atoms can reach high values of magnetic moment, about 5 μ_B that occurs in free atoms. If this configuration is repeated parallelly, the total magnetic moment can be a big one.

The system Mn/Fe(001) is complex partly due to the possible frustration produced at the interface between a ferromagnetic and an antiferromagnetic material in certain circumstances, and is also due to the nature of Mn itself. Mn can be found in 5 allotropies. The α phase is cubic with 58 atoms in the unit cell at room temperature, stable up to 1000 K. Under the Néel temperature $T_N = 95\ K$, the α-Mn paramagnetic-antiferromagnetic transition is accompanied by a distortion to the tetragonal crystal structure [76]. The magnetic structure of α-Mn is non-collinear with high magnetic moment (up to 3 μ_B) in certain positions, coexisting with smaller magnetic moments in other positions and even non-magnetic [76, 77]. The β-Mn is cubic with 20 atoms in the unit cell [78], stable between 1000 and 1368 K. The γ-Mn (fcc) is stable between 1368 and 1406 K, and the δ-Mn (bcc) is stable from 1406 K to the melting temperature $T_M = 1517\ K$. Studies at ultrahigh pressure [79] show a phase transition to an ϵ-Mn at 165 GPa. The probable hexagonal structure is in agreement with the crystal structure of analogous elements Tc and Re.

The magnetic properties are, as expected, very different in the allotropies of Mn. For example, Nakamura *et al* [80] show that β-Mn is magnetically disordered at temperature of 1.4 K and shows strong spin fluctuations. Canals and Lacroix [81] suggest that the frustration in β-Mn overrides any magnetic order and it should be regarded as a "spin liquid". As in the α-Mn, the γ-Mn is antiferromagnetic with a Néel temperature $T_N = 570$ K. The determination of the magnetic structure

of δ-Mn is even harder to achieve. As for the ϵ-Mn phase, it is paramagnetic in equilibrium.

In the case of Mn thin films deposited on other materials, there is also a wide variety of behaviors. The studies have been conducted for Mn grown on Al [82], Cu, Ni [83], Pd [84] and Ir [85], the fcc-type substrates, and Fe [68, 86], the bcc-type substrate. All the depositions are oriented in the direction [001]. In all the cases, Mn is pseudomorph. While growing conditions prevent interdiffusion, theoretical studies [87–90] and experiments [103–105] are in agreement with a $C(2\times2)$ antiferromagnetic configuration for the case of the supported monolayer, and an antiferromagnetic configuration when two or more monolayers are deposited, except for some recent calculations in which the $C(2\times2)$ configuration occurs in the surface layer [126]. If Mn is deposited at high temperature on metals such as Cu, Ni, Ag, Pd [91–95], alloys are formed on the surface with order $C(2\times2)$.

The experimental investigations of the structure of Mn films on Fe(001) resulted in a large number of discrepant results. The experiments show that in small area, Mn grows layer by layer, taking a body-centered tetragonal (*bct*) structure with the parameters of lattice equal to the pure substrate Fe, but switching to a growth in the form of islands above a critical size of the Mn film [96–99]. This size ranges from 3 [98] to 12 monolayers [99]. For higher coverages, it might take the structure corresponding to α-Mn [100].

As for the coupling at the Mn-Fe interface, the situation is even more controversial. Some papers show a ferrimagnetic coupling with two inequivalent sites in Mn layers [69, 97, 101], while other papers present an antiferromagnetic coupling between Mn layers with antiferromagnetic coupling at the surface [86, 102] and ferromagnetic coupling at the interface [70], although the SP-STM measures can not draw a conclusion about the coupling at the interface [123, 124]. In addition, there are also ferromagnetic couplings within the Mn film with coverage up to 2-3 monolayers, and then becoming antiferromagnetic beyond these coverages [103–105].

When studying Mn films on Fe in the presence of monoatomic steps, recent experiments also show different results. In such systems magnetic domains are observed as a result of different surface coverage on both sides of the step. The value of the width of the domain wall that separates the two regions differs in the experiments of Yamada *et al* [72, 123, 128] and Schlickum *et al* [124]: while in the experiments of Yamada *et al* the width of the domain wall does not vary by increasing the thickness of Mn deposited, the results of Schlickum *et al* show that it varies and depends linearly on the number of layers deposited.

As you can see, there is a variety of results due to the complex nature of Mn and the competition of ferromagnetic and antiferromagnetic interactions, which usually make the systems studied have a frustrated magnetic configuration. And we also know that a frustrated state is very sensitive to any type of perturbations. It is expected that such a frustrated system will show a variety of magnetic configurations depending on the temperature and the external magnetic field [108]. To understand the essence of the physics of magnetic frustration, it is very important to investigate the evolution of magnetic configurations under magnetic fields up to the full saturation of magnetic moments. In a technological point of view, the response of a magnetic material to external magnetic fields is important for its potential application for data storage devices. At present the highest data storage density is 421 Gbit/in^2 (i.e., about 560 nm^2/bit)by Seagate Technology using perpendicular magnetic recording(PMR). Deeper understanding of the noncollinear magnetic properties, especially the noncollinear hysteresis, may shed light on new technologies that could express a bit of information in smaller and smaller area in a material. Then a higher level of miniaturizaiton of data storage devices could be achieved.

The rich magnetic behavior of Mn films supported on Fe substrate and the high spin polarization of both elements make it particularly interesting to study the response of the system to external magnetic fields. One already knows that the noncollinear magnetic moment configuration is essential in the systems of Mn/Fe. But when the system is imposed with an external magnetic field, and as the fields increase, the magnetic configuration would change. An interesting

phenomenon is shown in recent experimental results of Kojima *et al* [135], in which the external magnetic fields are applied up to 140 T in the $CdCr_2O_4$ system under low temperature, below 26 K. This system is noncollinear in absence of external magnetic field, but when the fields increase to the range between 28 T and 62 T, a collinear 1/2 plateau phase appears. Above 62 T, the system becomes noncollinear again until reaching the magnetic saturation at 90 T. It is expected to find a material that possesses the same magnetization process under reasonable external magnetic field (which is possible in experiment) and at room temperature. Then the application as data storage devices would be possible. Our study is on this line at the starting point.

In this chapter, we firstly depict relevant experiments shortly, from which we pick some parameters for our calculations, such as the distances between layers. Then we parameterize the system of 6 Mn layers deposited on Fe substrate that will be used in the TB calculation. Later we show our collinear and noncollinear results, without external magnetic field and then with magnetic fields up to magnetic saturation. Finally, we conclude this chapter and show some perspectives for future study.

3.2 Structure information taken from previous experimental results

The geometric information which is needed as an initial input to our TB model is taken from the experiment [128]. In this thesis we consider the *bcc* phase of Fe substrate, 6 Mn monolayers are supported on it. Due to the different atomic radii of Fe and Mn, the distances between layers in the Mn film are neither the lattice constant in pure Fe crystal nor that in pure Mn crystal. These distances should be measured layer by layer in experiment.

The STM and STS measures were carried out by Yamada *et al* [128] under the conditions of ultrahigh vacuum ($\sim 5\times10^{-11}$mbar) at room temperature. Mn layers

are grown in an almost perfect monocrystal Fe sample in the [001] orientation at temperature of 370 K and with the rate of 0.6 nm/min. The growth condition is very important, because Mn and Fe tend to mix and the magnetic properties of Mn films are very sensitive to the atomic structure [88].

Layer by layer growth of Mn on Fe(001) is achieved with coverage of up to 3 monolayers, while above these coverages the system begins to create three-dimensional islands and terraces. The structure of this growth, pseudomorphic, is characterized by the same two-dimensional structure in Fe substrate ($a = b =$ 0.287 nm), while the distance between layers is $c = 0.323$ nm, which corresponds to a *bct*-type structure. When the substrate contains a Fe monoatomic step (which is 0.143 nm high), the step is reflected on the surface of Mn as a much smaller step of height of 0.02 nm (due to the difference between the lattice constant of Fe and Mn, and the number of Mn layers is n in one side compared to $n + 1$ at the other side). For coverage higher than 6.5 monolayers, the step height of 0.02 nm is not seen any more, which means the surface tends to be flat.

The geometric parameters in the system of 6 Mn layers supported on Fe substrate are taken from the above experimental results.

3.3 Parametrization

The accuracy of the parametrization is critical for any semi-empirical model in general, especially in a system that contains Mn. We have already seen that Mn is a delicate material to work with for investigating noncollinear features due to its very complex structure..

The first step is to find the parameters for GCN approximation described in chapter 2. In order to do the least square estimation, we need some samples with different local environments. The systems and their coordinations we choose to implement TB-LMTO calculations are shown in Table 3.1. We take into account

	monolayer	bilayer	trilayer (C)	trilayer (E)	solid
(001)	4.2	6.4	8.4	4.5	8.6
(110)	0.4	4.4	8.6	6.4	8.6
(111)	0.0	3.0	6.0	3.3	8.6

TABLE 3.1: Values of the coordination for different systems and crystalline orientations. (C≡Center, E≡Exterior)

the solid, monolayer, bilayer and trilayer in three crystalline orientations, [001], [110] and [111], for Fe and Mn.

We explain the values in the table as follows, for example, in the perfect solid with the structure of *fcc* the number of first neighbors is 8 and that of second neighbors is 6, which leads to a coordination of 8.6. The remaining values are obtained similarly.

3.3.1 Parametrization for Fe

The TB-LMTO calculations of the systems described above are conducted to find the parameters of our Mn/Fe(001) system. The exchange and correlation potentials for Fe are taken as the GGA potential proposed by Perdew[106, 107]. In the calculations, depending on the compactness of the systems under consideration, 5 to 13 layers of empty spheres are taken into account to assure the electronic distribution in the central layer of empty spheres is negligible. We increase the number of k points in the Brillouin zone until the results of the band centers $\varepsilon_{i\alpha}^{0,ref}$ converge in each system. The results obtained for the band centers as well as the electronic distributions in different systems of Fe (solid, monolayer and bilayer) are shown in Table 3.2.

One can see the charges obtained for all the above systems are similar, except for the monolayer on the [111] orientation, where part of the charges is transferred to the space because the distance between atoms on this plane is the biggest.

The parametrization is checked with several tests. To test the transferability of these parameters, they are used in systems with different coordinations. We firstly

	$\varepsilon_s^{0,ref}$	$\varepsilon_p^{0,ref}$	$\varepsilon_d^{0,ref}$	N_s	N_p	N_d	N_{tot}
solid	3.87	8.56	−0.59	0.63	0.77	6.60	8.00
monolayer(001)	−1.43	0.51	−5.01	0.66	0.26	6.62	7.53
monolayer(110)	−0.90	3.67	−6.14	0.62	0.36	6.58	7.56
monolayer(111)	1.89	6.22	−3.93	0.34	0.03	6.53	6.90
bilayer(001)	0.21	4.62	−4.45	0.57	0.42	6.68	7.66
bilayer(110)	−0.98	3.55	−5.60	0.62	0.56	6.64	7.83
bilayer(111)	0.25	4.36	−4.90	0.63	0.28	6.560	7.47

TABLE 3.2: Values of the band centers (in units of eV) and charges for different systems of Fe obtained from TB-LMTO method.

	TB-LMTO		TB: SMB		TB: bilayers	
	solid	bilayer	solid	bilayer	solid	bilayer
J_{dd} (Fe)	-	-	1.20	1.20	1.20	1.20
N_s	0.64	0.60	0.66	0.58	0.65	0.56
N_p	0.78	0.44	0.73	0.39	0.75	0.39
N_d	6.58	6.62	6.61	6.70	6.60	6.72
$\mu(\mu_B)$	2.38	2.76	2.29	2.89	2.29	2.87

TABLE 3.3: Values of the charges and magnetic moments for the perfect solid and Fe bilayer in the [001] direction calculated using TB-LMTO and TB. In the latter case we have two sets of parameters: extensive solid, monolayer and bilayer (SMB) and bilayers in different orientations.

test the parametrization in perfect solid and the bilayer in the [001] direction. As a final test, the parametrization is tested in similar systems we are going to study with the TB method, i.e., 6 layers Mn supported on Fe(001) substrate. In all these cases, the TB results are compared with those obtained by the TB-LMTO method for corresponding system.

In Table 3.3 we show the results obtained for perfect solid and for the bilayer in the [001] direction using TB-LMTO and TB methods. In the TB calculations, the exchange parameter $J_{dd} = 1.20$ eV for both systems. It is taken from other systems similar to those we want to study here. And the value can be varied to adjust the values of the magnetic moment with only a little change in charges. For each case we used the hopping integrals $t_{ij}^{\alpha\beta}$ from the TB-LMTO calculations. One can see that the results for charge distributions between orbitals and the magnetic moments are in agreement with those obtained by TB-LMTO.

	TB-LMTO		TB:SMB		TB:SMB		TB:bilayer		TB:bilayer	
hopping integrals	-		solid		surface		solid		surface	
J_{dd} (Fe)	-		1.20		1.20		1.20		1.20	
	S	S-1	S	S-1	S	S-1	S	S-1	S	S-1
N_s	0.60	0.66	0.57	0.66	0.58	0.66	0.45	0.67	0.44	0.66
N_p	0.43	0.80	0.40	0.73	0.38	0.72	0.32	0.75	0.30	0.72
N_d	6.49	6.69	6.79	6.62	6.79	6.63	6.46	6.68	6.43	6.66
N_T	7.52	8.15	7.76	8.01	7.75	8.01	7.23	8.10	7.17	8.04
$\mu(\mu_B)$	3.02	2.31	2.81	2.44	2.82	2.45	3.13	2.39	3.17	2.42

TABLE 3.4: Values of charges and magnetic moments for Fe(001) surface calculated by TB-LMTO and TB methods. In the TB calculations, solid, monolayer and bilayer(SMB) and bilayers in different orientations are taken into account. S and S-1 indicate the surface layer and the layer just below the surface.

We next consider a Fe surface in the [001] direction. The results for two sets of parameters (SMB and bilayers) are shown in Table 3.4. In the TB-LMTO calculations it is sufficient to consider 5 layers of empty spheres to simulate the surface, while the number of layers needed to simulate the Fe bulk is 8. The exchange parameter J_{dd} used is the same as in previous calculations. In addition, different hopping integrals (in perfect solid and surface) are used in the TB calculations. They are two extreme cases in our calculations, hopping integrals in other cases (such as the subsurface and so on) are between these two cases. So for simplicity, we differentiate hopping integrals into these two cases.

The effect of the surface is reflected in the charges and magnetic moments: the surface atoms lose some charge with respect to the next layer and there is an increase of magnetic moment due to less coordination. When analyzing the values obtained for each parametrization compared to TB-LMTO, there are some discrepancies. In the SMB setting, in the surface layer there is an increase of 0.3 in the charge of d orbital with respect to TB-LMTO. Regarding the perfect solid (with 8 electrons in d orbital), in the SMB setting the difference of charges on the surface and subsurface in TB results is lower than that in TB-LMTO (about 0.2 electrons). But there is a bigger charge transfer in the bilayer setting. The differences in results when considering different sets of hopping integrals are not significant in the calculations, as shown in Table 3.4.

	$\varepsilon_s^{0,ref}$	$\varepsilon_p^{0,ref}$	$\varepsilon_d^{0,ref}$	N_s	N_p	N_d	N_{tot}
bilayer(001)	0.77	4.91	−4.14	0.56	0.42	5.65	6.63
bilayer(110)	−1.64	2.65	−6.45	0.61	0.59	5.61	6.81
bilayer(111)	1.16	5.40	−4.66	0.57	0.25	5.50	6.32
trilayer(001)(C)	−0.42	4.71	−4.69	0.68	0.86	5.73	7.26
trilayer(001)(E)	0.73	4.35	−4.18	0.54	0.41	5.56	6.61
trilayer(110)(C)	−0.01	4.73	−4.28	0.65	0.85	5.64	7.14
trilayer(110)(E)	0.98	5.15	−3.94	0.60	0.56	5.58	6.89
trilayer(111)(C)	1.31	6.11	−3.89	0.69	0.57	5.61	6.87
trilayer(111)(E)	1.65	5.52	−3.71	0.51	0.31	5.54	6.36

TABLE 3.5: Values of the band centers (in unit of eV) and charges for different systems of Mn obtained from TB-LMTO method.

3.3.2 Parametrization for Mn

In the case of Mn, we calculate in the same way as we did for Fe in TB-LMTO calculations in various systems (solid, monolayer and bilayer) using the exchange and correlation potential of Perdew's GGA. Sufficient layers of empty spheres and k points in Brillouin zone are taken into account. As we will see later, the variety of solutions presented in Mn makes the choice of parameters more sensitive than in other materials such as Fe. Therefore we test different sets of parameters to describe the system we study.

In Table 3.5, the values of band centers and charges for different systems of Mn are presented. The cases of bilayer and trilayer are considered. In the trilayer, the central layer is marked with C, and the exterior layer with E. Compared with the case of Fe, we observe that the band centers have the same order of magnitude. As for the charge distribution, one can see that the total charge in the bilayer in the [111] direction is quite lower (about 0.7 electrons) than that in perfect solid (7 electrons), the discrepancy is not so significant in the remaining cases.

Table 3.6 gives the parameters for the GCN approximation in two cases: bilayers and trilayers in different orientations, respectively. In choosing one or another set of parameters for the GCN approximation, relevant tests are performed as in the case of Fe, we simulate the systems in which we need to fit by TB calculations. However, the above two sets of parameters give very similar results even when we

(eV)	$\varepsilon_s^{0,at}$	$\varepsilon_p^{0,at}$	$\varepsilon_d^{0,at}$	ξ_s	ξ_p	ξ_d
bilayers	−8.21	−4.08	−29.70	−1.09	−1.07	−0.94
trilayers	−11.30	−8.36	−31.22	−0.60	−0.36	−0.55

TABLE 3.6: Mn Parameters of GCN approximation for bilayer and trilayer.

perform the TB calculations of systems with different thicknesses supported Mn on Fe(001). To single out a better set of the GCN parameters, we take into account other parameters (hopping integrals $t_{ij}^{\alpha\beta}$ and exchange parameter J_{dd}), which are also obtained from the TB-LMTO calculations.

Hopping integrals $t_{ij}^{\alpha\beta}$ for Mn

To obtain the hopping integrals $t_{ij}^{\alpha\beta}$ for the system of Mn supported on Fe(001), we have to reproduce the effects of interface between Fe and Mn as well as the surface effects and effects on intermediate Mn layers. These effects are mainly focused on the magnetic properties, e.g. the magnetic moments in various location. They are important in our TB studies both in collinear and in noncollinear framework. In Table 3.7 we compare the results of magnetic moments and charges in the system 3Mn/Fe(001) taking into account the hopping integrals obtained from TB-LMTO calculations, from the calculations already performed by Papaconstantopoulos [52] and from the Mn bulk. We have considered an exchange parameter $J_{dd} = 1.08$ eV, which is the best when comparing the magnetic moments obtained from TB-LMTO. As we can see, the results of magnetic moments obtained in 3Mn/Fe(001) is better than those with other parametrizations. It is an expected result because we've tried to simulate the similar system which we want to study the interface and surface effects.

Exchange parameter J_{dd} for Mn

The determination of the exchange parameter J_{dd} is performed in a similar system to the previous 3Mn/Fe(001). We also take into account the effects of Fe-Mn interface and Mn surface but with more Mn layers, in this case we consider 4 Mn layers supported on Fe(001). As there are many possible magnetic configurations in the Mn layers, which are more evident in the collinear calculations of

	3Mn/Fe(001)	Papaconstantopoulos	bulk	TB-LMTO
Mn(S)	3.83	3.92	3.82	3.77
Mn(S-1)	−2.39	−3.21	−2.83	−2.00
Mn(I)	2.52	3.03	2.49	2.83
Fe(I)	2.37	2.58	2.40	2.43
Fe(B)	2.35	2.30	2.38	2.33

TABLE 3.7: Results of the magnetic moments (in units of μ_B) in several selected layers of 3Mn/Fe(001) using different parametrizations and compared with those obtained with the TB-LMTO method.

J_{dd}	1.05	1.075	1.10	1.125	1.15	TB-LMTO
Mn(S)	−3.82	−3.85	−3.89	−3.92	−3.95	−3.76
Mn(S-1)	2.59	2.70	2.70	2.86	2.96	1.90
Mn(S-2)	−0.80	−0.98	−0.98	−2.45	−2.67	−2.98
Mn(I)	2.35	2.47	2.47	2.76	2.82	2.89
Fe(I)	2.34	2.33	2.33	2.34	2.33	2.45
Fe(B)	2.36	2.36	2.36	2.36	2.36	2.34

TABLE 3.8: Comparison of magnetic moments (in units of μ_B) in selected layers of 4Mn/Fe(001) using different exchange parameters with those obtained with TB-LMTO method.

6Mn/Fe(001) performed later, we choose the configuration with the lowest energy, the layered antiferromagnetic (LAF) one. The comparison with TB-LMTO results is shown in Table 3.8 in case of different choices of exchange parameter J_{dd} in TB calculations.

In all the calculations, we present here five calculations with exchange parameter J_{dd} varying from 1.05 eV through 1.15 eV. As we can see, the values of magnetic moments increase as the value of exchange parameter increases. For the first calculation, $J_{dd} = 1.05$ eV, it produces a very good value of magnetic moment on the surface, with an discrepancy of only 1.5% to the TB-LMTO calculation. However, the magnetic moments in the other layers, e.g. for the second subsurface layer Mn(S-1) the discrepancy is close to 300%, so that this value of J_{dd} should not be taken into account. Furthermore, as the errors in some layers reduce, the errors in other layers will increase, thus we arrive at a compromise to choose the most appropriate value for J_{dd}. For $J_{dd} = 1.075$ eV and 1.10 eV, the differences with respect to the previous case are not significant. There is a jump for the magnetic

moment on the second subsurface layer when $J_{dd} = 1.125$ eV, at which the error in the second subsurface layer reduces significantly. As we continue increasing the value of J_{dd}, the error in the subsurface becomes larger. So, finally, we take the exchange parameter J_{idd} because it gives the best overall result (in all Mn layers) compared to the TB-LMTO results.

3.4 6 Mn layers supported on Fe substrate: collinear framework

Mn layers supported on Fe substrate is a system that possesses fruitful magnetic effects, not only the surface and interface effects which also present in other systems, but also the complex magnetic nature of Mn which is different from other magnetic materials (Cr, Co, Ni and so on). In the periodic table, Mn is between Fe (typical ferromagnet) and Cr (typical antiferromagnet). The magnetic properties of Mn might be interesting. And the coupling between Mn and Fe is expected to be complex even in the collinear framework.

In this work, we study the system of 6 Mn layers supported on Fe(001) substrate. The structure of Fe substrate is *bcc*, and the same structure continues into the Mn layers. For more layers of Mn coverage, the structure of supported Mn tends to be very complex. The lattice constant of Fe and the interlayer distances in Mn slab and several Fe interface layers are taken from the experiment [128].

We implement our TB method to calculate, firstly, all the possible collinear magnetic configurations in Mn layers, and then apply external magnetic fields to two selected configurations up to magnetic saturation. As mentioned above, complex configurations of Mn layers are obtained. And the magnetic evolution is also examined.

state	E(eV)	moment(μ_B)	configuration
0	0.000	−0.16	− + − + − +
1	0.088	0.22	+ − − + − +
2	0.117	1.12	+ − + + − +
3	0.199	0.12	+ − + − + −
4	0.209	0.31	+ − + − − +
5	0.270	−0.28	− + + − + −
6	0.294	−0.11	− + + − − +
7	0.318	−1.16	− + − − + −
8	0.381	−1.12	− + − + − −
9	0.395	−0.30	− + − + + −
10	0.464	−0.72	+ − − + − −
11	0.469	0.12	+ − − + + −
12	0.531	0.19	+ − + + − −
13	0.604	1.12	+ + − + − +
14	0.769	−0.19	− − + + − +
15	0.787	−1.18	− − + − + −
16	0.793	−1.03	− − + − − +
17	0.942	0.16	+ + − − + −
18	0.950	1.03	+ + − + + −
19	0.996	0.23	+ + − + − −
20	1.188	−1.14	− − + + − −
21	1.272	−1.06	− − − + − +
22	1.627	−1.99	− − − + − −

TABLE 3.9: Collinear magnetic arrangements obtained for the 6Mn/Fe(001) system. The signs indicate the orientation of the magnetic moments of the Mn layers with respect to the positive z axis (Fe bulk orientation). The first sign in each configuration refers to the surface Mn layer. Energy differences relative to the collinear ground state and average magnetic moment for the Mn layers are shown.

3.4.1 Intrinsic magnetic properties

We start with the analysis of the magnetic properties of six Mn layers supported on the Fe(001) substrate. If we consider a $p(1 \times 1)$ configuration, in which the magnetic moment of each Mn layer can point either in the $+z$ direction (+) or in the $-z$ direction (−), there are $2^6 = 64$ possible collinear magnetic configurations in the Mn slab.

In Table 3.9 we present those collinear magnetic configurations which are solutions of the self-consistent calculation. The correspondence of each pair of the

input configuration	solution	input configuration	solution
+ + + + + +	+ + − + − +	− + + + + +	− + − + − +
+ + + + + −	+ + − + + −	− + + + + −	− + + − + −
+ + + + − +	+ − + + − +	− + + + − +	− + − + − +
+ + + + − −	+ − + + − −	− + + + − −	− + − + − −
+ + + − + +	+ − + − − +	− + + − + +	− + + − − +
+ + + − + −	+ − + − + −	− + + − + −	− + + − + −
+ + + − − +	+ − + − − +	− + + − − +	− + + − − +
+ + + − − −	+ − + − + −	− + + − − −	− + + − + −
+ + − + + +	+ + − + − +	− + − + + +	− + − + − +
+ + − + + −	+ + − + + −	− + − + + −	− + − + + −
+ + − + − +	+ + − + − +	− + − + − +	− + − + − +
+ + − + − −	+ + − + − −	− + − + − −	− + − + − −
+ + − − + +	+ + − + − +	− + − − + +	− + − + − +
+ + − − + −	+ + − − + −	− + − − + −	− + − − + −
+ + − − − +	+ + − + − +	− + − − − +	− + − + − +
+ + − − − −	+ + − − + −	− + − − − −	− + − − + −
+ − + + + +	+ − + + − +	− − + + + +	− − + + − +
+ − + + + −	+ − + − + −	− − + + + −	− − + − + −
+ − + + − +	+ − + + − +	− − + + − +	− − + + − +
+ − + + − −	+ − + + − −	− − + + − −	− − + + − −
+ − + − + +	+ − + − − +	− − + − + +	− − + − − +
+ − + − + −	+ − + − + −	− − + − + −	− − + − + −
+ − + − − +	+ − + − − +	− − + − − +	− − + − − +
+ − + − − −	+ − + − + −	− − + − − −	− − + − + −
+ − − + + +	+ − − + − +	− − − + + +	− + − + − +
+ − − + + −	+ − − + + −	− − − + + −	− + − + + −
+ − − + − +	+ − − + − +	− − − + − +	− − − + − +
+ − − + − −	+ − − + − −	− − − + − −	− − − + − −
+ − − − + +	+ − + − − +	− − − − + +	− + − + − +
+ − − − + −	+ − + − + −	− − − − + −	− + − − + −
+ − − − − +	+ − − + − +	− − − − − +	− − + − + −
+ − − − − −	+ − − + − −	− − − − − −	− − + − + −

configurations(state)	TB-LMTO	our results
− + − + − + (0)	0.00	0.00
+ − + + − + (2)	0.07	0.117
+ − + − − + (4)	0.16	0.209
− + + − − + (6)	0.26	0.294
+ − + − + − (3)	0.37	0.199

TABLE 3.11: Comparison of the energy (in eV) of some configurations in our TB calculations with those obtained by TB-LMTO calculations.

in Table 3.9, i.e., . This is an evidence of the particularly strong surface effect in this system.

Some of the final configurations have been already studied in previous works by means of *ab initio* DFT (TB-LMTO) calculations [125, 126]. The comparison with our calculations is shown in Table 3.11, which is in good agreement except state 3.

Both parallel and antiparallel couplings between Mn layers as well as at the Mn/Fe interface exist. The ground state in the collinear framework shows antiparallel couplings between Mn layers and a parallel coupling at the Mn/Fe interface, in agreement with experimental results[123, 124]. As a general trend, we find that those metastable configurations which are energetically close to the ground state have antiparallel coupling between the Mn-surface and subsurface layers as well as between the Mn layers adjacent to the Fe interface, and a parallel coupling at the Mn/Fe interface. A variety of metastable configurations corresponding to different magnetic couplings in Mn (particularly in the central layers of the slab) are obtained within a small energy range. The existence of all these metastable configurations indicates two facts: i) this system is a clear candidate to exhibit more stable noncollinear magnetic arrangements if we remove the constraint of collinearity. This is in accordance with results of Hafner and D. Spišák [126] for supported Mn slabs with 1 or 2 layers thicknesses; ii) This system should be particularly interesting as regard to its response to external magnetic fields. In this context, it is also interesting to note that the magnetic moments of Mn are quite large, being the surface and the interface moments ($4.0\mu_B$ and $3.0\mu_B$, respectively)

larger than the moment of the central layers (between $2.5 - 2.9\mu_B$), as the effects of decreasing the number of neighbors (surface) and the influence of the effective magnetic field from the Fe layers (interface) are taken into account.

3.4.2 Response to external magnetic fields

Starting from the system in its collinear ground state (configuration 0 in Table 3.9), we apply an uniform external magnetic field along the moments of Fe substrate, choosing the z axis as parallel to the field. We calculate the electronic structure and magnetic configurations as functions of the field, whose intensity is increased by 100 T until the system reaches the magnetic saturation. Then the field intensity is decreased to zero. In Figure 3.1 we plot the average magnetic moment in the Mn slab as a function of the external field. Each point in this graphic represents a self-consistent calculation. Units of the external field are referred to $B_S^C = 14 \times 10^3$T, which is the intensity required for the system to become magnetically saturated in the collinear framework. In the magnetically saturated configuration (S in Fig. 3.1 and Fig. 3.2) all the local magnetic moments of the system are oriented along the field (also those of the Fe substrate) and reach their maximum value since the electronic structure is fully spin-polarized. It is worth to note that intermixing at the interface can decrease the spin-flip magnetic field. Calculations performed within collinear periodic Anderson model for Fe/Cr multilayers [134] demonstrate that even the shape of hysteresis loop calculated individually for Fe and for Cr atoms changes significantly depending on the chemical structure of the interface region. In Figure 3.1 we observe both smooth and sharp changes of the average magnetization depending on the external field. When the average moment increases (or decreases) smoothly as a function of the field, the electronic structure of the system corresponds to a magnetic configuration in which the moduli of the local moments vary while preserving the relative magnetic couplings. Those regions are marked with a bidirectional arrow indicating their reversible character. When the external field reaches a critical value, it overcomes a local exchange coupling, and an irreversible change in the response is obtained. This situation is

reflected by a sharp change in Figure 3.1. The system undergoes a transition to a magnetic configuration where, not only the moduli of the local moments vary, but also their relative exchange couplings change. If, at this point, the applied external field is reduced, the old configuration is not immediately recovered, but at an smaller applied field. The system describes then a hysteresis cycle, as can be seen in Figure 3.3 and Figure 3.4 between solutions 2 and 1. In Figure 3.1 several of such irreversible transitions can be identified. One of them leads the system to a magnetic configuration with local exchange couplings similar to those of solution 4 in Table 3.9, but with different magnitudes due to the presence of the external field. There are other irreversible transitions which lead to configurations showing magnetic behaviors which are not selfconsistent solutions in the absence of external field and, therefore, are not presented in Table 3.9. These are, namely, a $(-+++-+)$, b $(-++++++)$, and c $(+++-++)$.

By analyzing the electronic structure and the magnetic configurations of the system as increasing the external field, we come to conclusions about the relative strength of the exchange couplings at the different parts of the Mn slab. As increasing the field intensity, moments of the central layers are the first to flip and to point along the field orientation (configuration a), followed by the moments close to the interface (configuration b), and finally by the surface moments. Notice that the local moments at the surface are larger than the rest. These results indicate that the antiparallel exchange couplings at the central layers of Mn are weaker than those at the interface and than those at the surface regions. This is consistent with the results obtained in the absence of external field, where the antiparallel couplings at the surface region and near the interface characterize the metastable solutions close to the ground state, see Table 3.9.

The average magnetic moments and magnetic moments in each layer of Mn slab for the intermediate configurations in the evolution shown in Figure 3.1 are listed in Table 3.12. These configurations do not exist when the magnetic field is released.

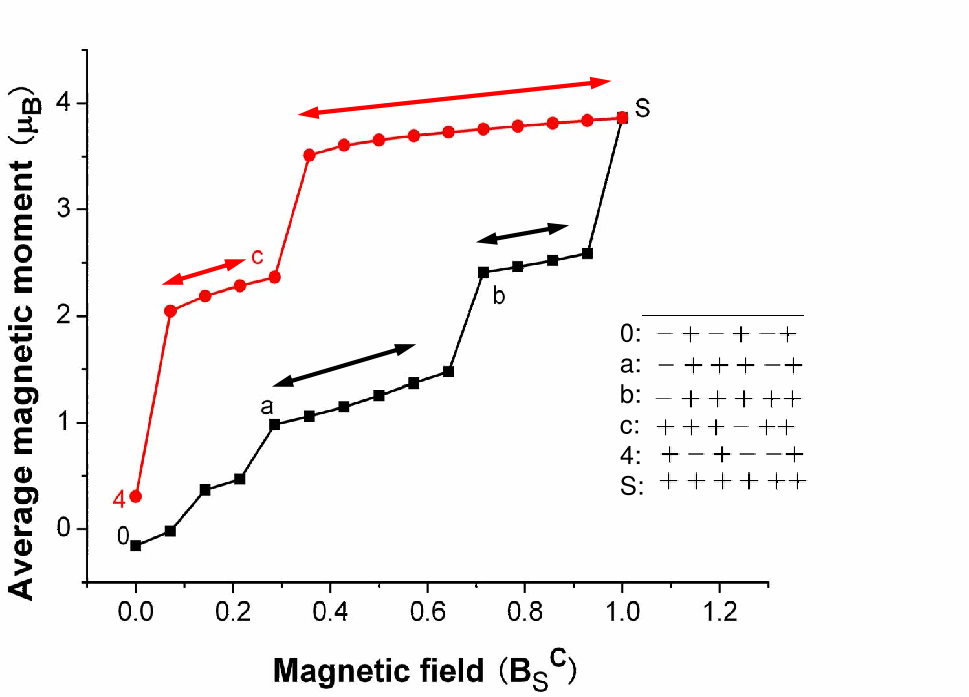

FIGURE 3.1: Evolution of the average magnetic moment (collinear approach) in the Mn slab as a function of the external uniform magnetic field (in units of the saturation field B_S^C) starting from the collinear ground state: from 0 to B_S^C (black squares) and from B_S^C to 0 (red circles). Bidirectional arrows indicate the reversible parts of the process. Note that the red circle and black square at 0 T don't overlap, actually the vertical difference between them is the energy difference between configurations 0 and 4 in Table 3.9, which is about 0.2 eV.

configuration	field(B_S^C)	μ_S	μ_{S-1}	μ_{S-2}	μ_{S-3}	μ_{S-4}	μ_{S-5}
a	0.98	-3.89	3.09	2.96	3.01	-2.44	3.16
b	2.41	-3.46	3.54	3.54	3.59	3.64	3.59
c	2.36	4.15	3.26	3.08	-2.41	2.96	3.13
S	3.86	4.05	3.76	3.77	3.75	3.71	3.71

TABLE 3.12: Magnetic moments of Mn layers for the selected intermediate configurations in Figure 3.1. The subscript S indicates the surface, S-1 the subsurface, and so on.

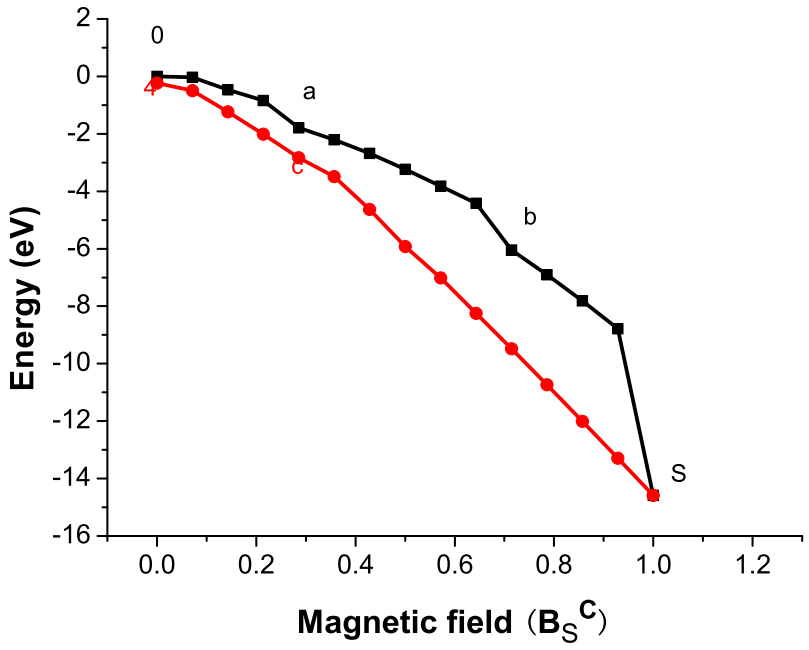

FIGURE 3.2: Evolution of the total energy in Mn slab for the process shown in Fig. 3.1.

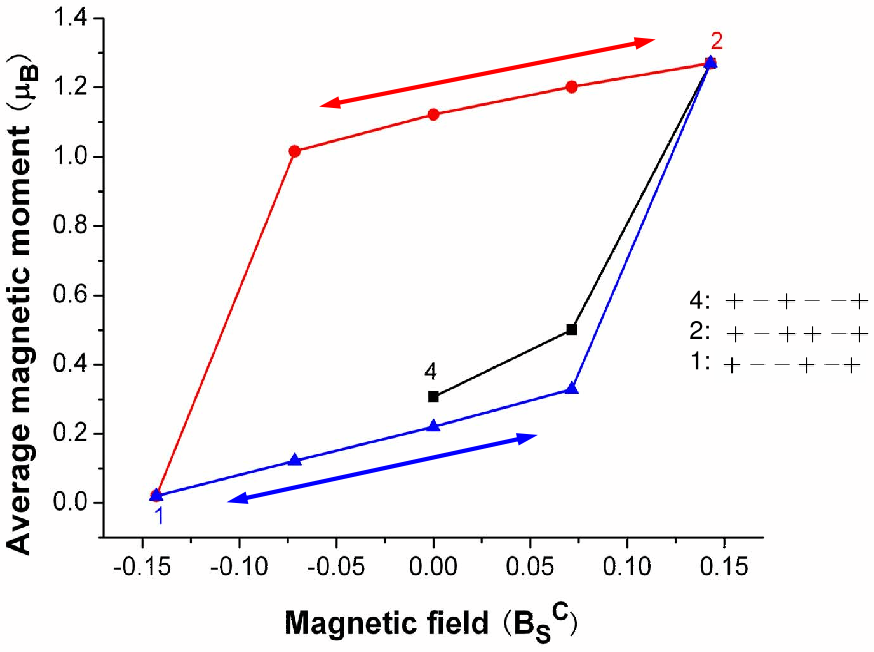

FIGURE 3.3: Evolution of the average magnetic moment as in Figure 3.1 but starting from the metastable solution 4 and closing the cycle before reaching the magnetic saturation.

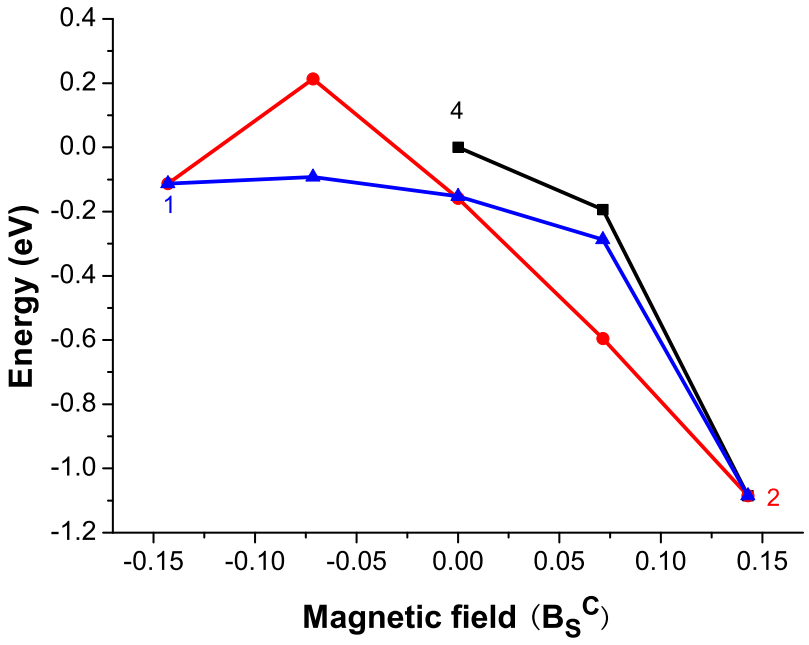

FIGURE 3.4: Evolution of the total energy as in Figure 3.2 but starting from the metastable solution 4 and closing the cycle before reaching the magnetic saturation.

The non-reversible character of the transitions between configurations having different relative exchange couplings gives rise to the possibility of using a external magnetic field for tuning the system between different magnetic solutions which are local minima in the absence of an external field. This fact is already demonstrated in Figure 3.1. Starting from the ground state (configuration 0), we were able to excite the system to configuration 4, which is a local minimum without an external field. These two solutions have similar average magnetic moment, but it is also possible to switch the system between two configurations with different average magnetization, as shown in Figure 3.3. In this case, starting from solution 4, we can reach solution 2 of Table 3.9 well before the magnetic saturation of the system. From solution 2 we can reach solution 1, closing the cycle, by using appropriate fields. Therefore, we are able to switch the system between configuration 1 (with a low average moment of $0.22\mu_B$) and configuration 2 (with high average magnetization of $1.12\mu_B$), and vice versa. We show in Table 3.13 the average magnetic moments and magnetic moments in each layer of Mn

configuration	field(B_S^C)	μ_S	μ_{S-1}	μ_{S-2}	μ_{S-3}	μ_{S-4}	μ_{S-5}
1	0.02	3.95	-3.00	-2.87	2.37	-3.09	2.77
2	1.27	4.07	-2.77	2.90	2.89	-2.55	3.09
4	0.31	4.05	-2.98	2.89	-2.66	-2.32	2.87

TABLE 3.13: Magnetic moments (in units of μ_B) of Mn layers for the selected intermediate configurations in Figure 3.3.

slab for the intermediate configurations in Figure 3.3. In this case, the average magnetic moment of configuration 2 is larger than that without external magnetic field, while the moment of configuration 1 is smaller. These differences are caused by the applied field. Although in this example we have artificially constrained the system to collinear configurations, situations similar to the present one can be achieved in systems with a strong uniaxial anisotropy, like single molecular magnets, mentioned in the introduction.

3.5 6 Mn layers supported on Fe substrate: non-collinear framework

In view of the multiple magnetic solutions obtained in the collinear framework, Mn is a clear candidate to exhibit noncollinear effects. This possibility has been explored within the DFT approach by Hafner and Spišák [126] for one or two Mn layers supported on Fe. Larger thicknesses require a huge computational cost within DFT. The magnetic frustration in the Mn/Fe(001) system arises partly from the ferromegnetic/antiferromagnetic interface, but mostly from the strange properties of Mn itself.

3.5.1 Intrinsic magnetic properties

In Figure 3.5 we show the magnetic configuration of the noncollinear ground state obtained for six Mn layers supported on Fe(001). This solution presents local couplings approaching to those obtained in the ground state collinear configuration

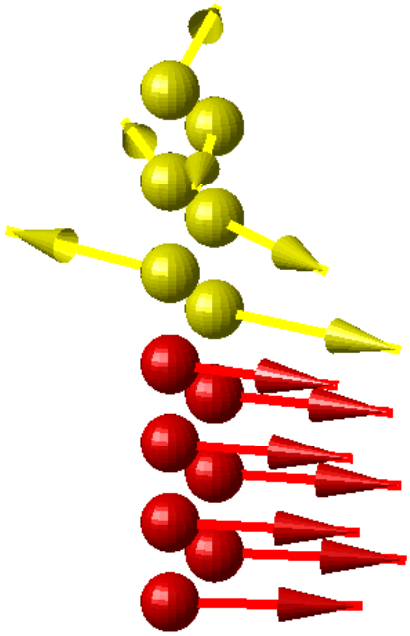

FIGURE 3.5: Noncollinear ground state of 6 Mn layers supported on Fe(001) substrate in absence of external magnetic field. One atom per (001) layer is shown. The Mn atoms are represented by yellow balls while the Fe atoms are represented by red balls. The Mn atoms are represented by yellow balls while the Fe atoms are represented by red balls. The arrows are proportional to the local magnetic moments.

(antiparallel couplings between Mn layers, and parallel couplings at the Mn/Fe interface and between Fe layers) but, in contrast, the surface magnetic moment is now perpendicular to the Fe bulk moment. The noncollinear ground state (Figure 3.5 and the collinear one (solution 0 of Table 3.9)) have otherwise similar energies, differing in 1 to 2 meV. The small energy difference can be understood considering that the local magnetic couplings are essentially preserved. Moreover, only one self-consistent magnetic arrangement (local minimum) is found in the noncollinear case, regardless of the input. As soon as one of the metastable configurations found in the collinear case is slightly perturbed and introduced as input of the noncollinear calculation, it evolves towards the noncollinear ground state. The release of the collinear constraint provides a new degree of freedom to the

local moments and their relative exchange couplings. We have seen that in the collinear framework the ground state can be only reached through the variations of the moduli of the local moments, and the system can get trapped in multiple local minima. Now, within the noncollinear framework, the local moments can continuously rotate during self-consistency towards the ground state. The mechanism of spin-flip is therefore different in both frameworks, and this will have important implications in the response of the system to external magnetic fields. As we will see in the next section, in the noncollinear picture the local moments will tend to rotate towards the field while preserving, at the same time, their relative exchange couplings.

3.5.2 Response to external magnetic fields

In the noncollinear framework the local magnetic moments of the system can have both longitudinal and transversal components (referred to the direction of the moment in the bulk). In Figure (3.6-3.8) we plot both components of the total moment in the Mn slab as a function of the external field, starting from the noncollinear ground state shown in Figure 3.5. As in the collinear case, each point represents a self-consistent calculation. In contrast to the collinear picture, now the response is reversible because the local moments can rotate and there is only one magnetic solution for a given value of the external field. Lower applied magnetic fields are now required to change the magnetic configuration, as compared with the collinear case. For instance, the applied field needed to reach the magnetic saturation is now $B_S^{NC} = 9.4 \times 10^3$ T, about two thirds of the value obtained in the collinear situation.

In Figure 3.9 we show several selected magnetic configurations corresponding to different intensities of the applied field. Their magnetic moments are listed in Table 3.14. In absence of external field, the longitudinal component of the total magnetic moment in the Mn slab is very small ($1.32\mu_B$). As the field is applied, the total moment rotates towards the field and the longitudinal component increases rapidly (see Figure 3.6). However, there is a competition between the

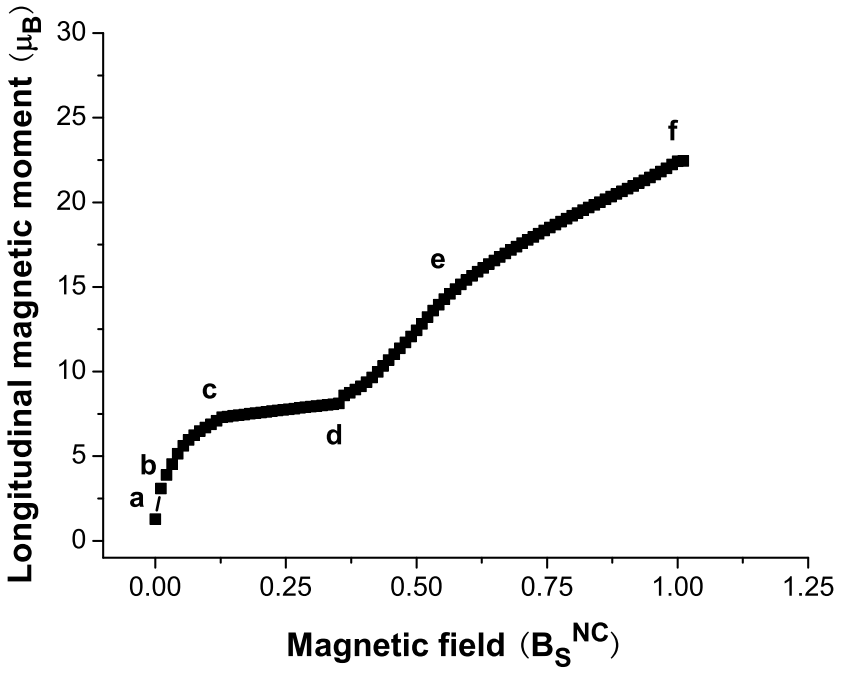

FIGURE 3.6: Evolution of the longitudinal component of the total magnetic moments in the Mn slab as a function of the external magnetic field (in units of the saturation field B_S^{NC}) starting from the noncollinear ground state. The symbol (a) in the subfigure corresponds to the ground state in Figure 3.5, and (b-f) for those states presented in Figure 3.9.

configuration	transversal moment(μ_B)	longitudinal moment(μ_B)	total moment (μ_B)
a	-0.103	1.324	1.328
b	-0.188	1.466	1.478
c	-0.001	1.835	1.835
d	-0.011	1.965	1.965
e	0.024	2.737	2.737
f	0.000	3.121	3.121

TABLE 3.14: Total magnetic moments of Mn slab for the selected intermediate configurations in Figure 3.6.

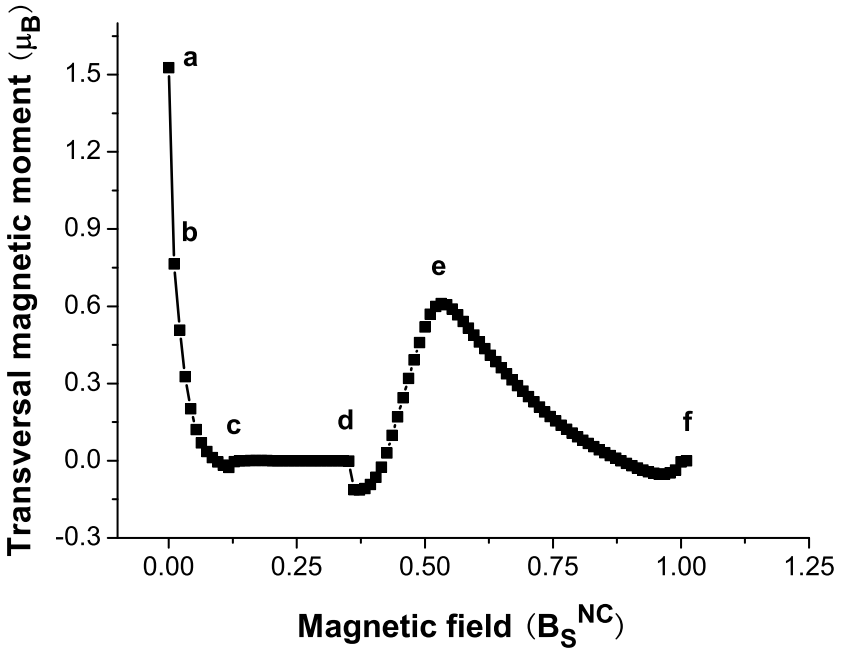

FIGURE 3.7: Evolution of the transversal component of the total magnetic moments in the Mn slab as a function of the external magnetic field (in units of the saturation field B_S^{NC}) starting from the noncollinear ground state. The symbols (a-f) are described in Figure 3.6

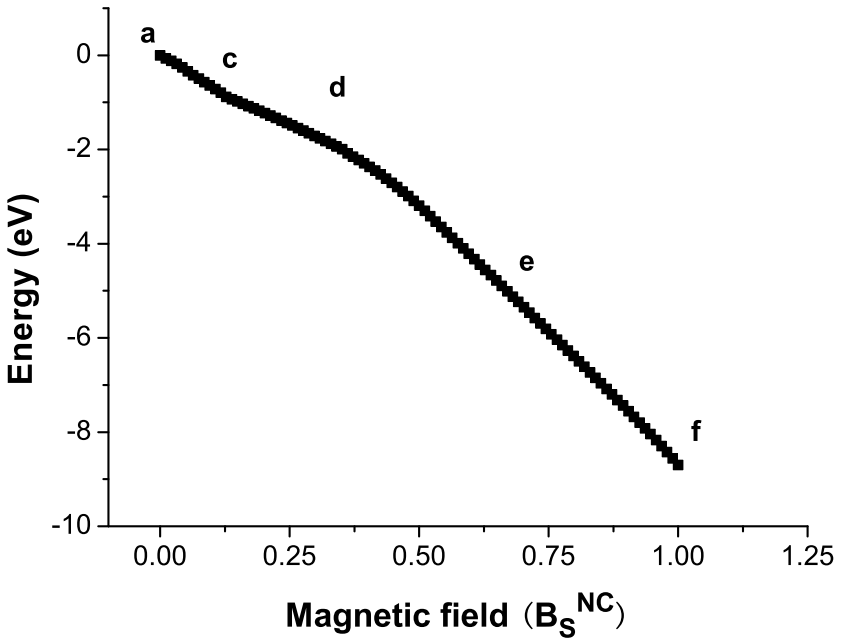

FIGURE 3.8: Evolution of the total energy in Mn slab for the process shown in Panel Figure 3.6 and 3.7.

tendencies of the local moments to align themselves with the field and to preserve their local antiparallel exchange coupling. This is clear in the selected magnetic configurations of Figure 3.9 for low fields, in which not all the local moments rotate towards the field. For instance, for $B = 0.01B_S^{NC}$ the moment of the subsurface Mn layer tries to preserve its antiparallel coupling with the moment of the surface layer, which rotates itself towards the field. This also happens in other parts of the slab. As increasing the field up to about $0.1B_S^{NC}$, the magnetic moments continue rotating; while the intensities of external magnetic fields are between this value and $0.3B_S^{NC}$, the local couplings in the system are similar to those of the collinear solution 2 of Table 3.9. In other words, the system gets trapped in a collinear magnetic configuration. This is reflected in the longitudinal and transversal components of the total magnetization in Figures 3.6 and 3.7, which stay almost constant between the referred fields. A less steep region of the energy plot in Figure 3.8 also shows this collinear configuration. For fields beyond $0.3B_S^{NC}$ the moments keep rotating up to the magnetic saturation. As obtained in the collinear framework, the magnetic couplings in the central layers are weaker than those at the interface region and at the surface.

Recently experimental results by Kojima *et al* [135] for the $CdCr_2O_4$ system show a similar noncollinear remagnetization feature at low temperature, below 26 K. They applied external magnetic fields up to 140 T in their geometrically frustrated system which saturated at 90 T. These authors referred to a 1/2 plateau phase in which Cr^{3+} has a 3-up 1-down collinear spin configuration between 28 T and 62 T. In our calculations for the Mn/Fe system we also obtain a collinear window for field intensities between $0.1B_S^{NC}$ and $0.3B_S^{NC}$. As regard to the order of magnitude of the required external fields during the remagnetization process, we note that the exchange parameter $J = 0.6\ meV$ estimated by Kojima *et al* for the system $CdCr_2O_4$ is several orders of magnitude weaker than those involved in our Mn/Fe system ($J = 1.125\ eV$ in Mn layers and $J = 1.265\ eV$ in iron layers). Therefore, huge external fields are expected to be required for the remagnetization process in our case, and in particular to reach the magnetic saturation.

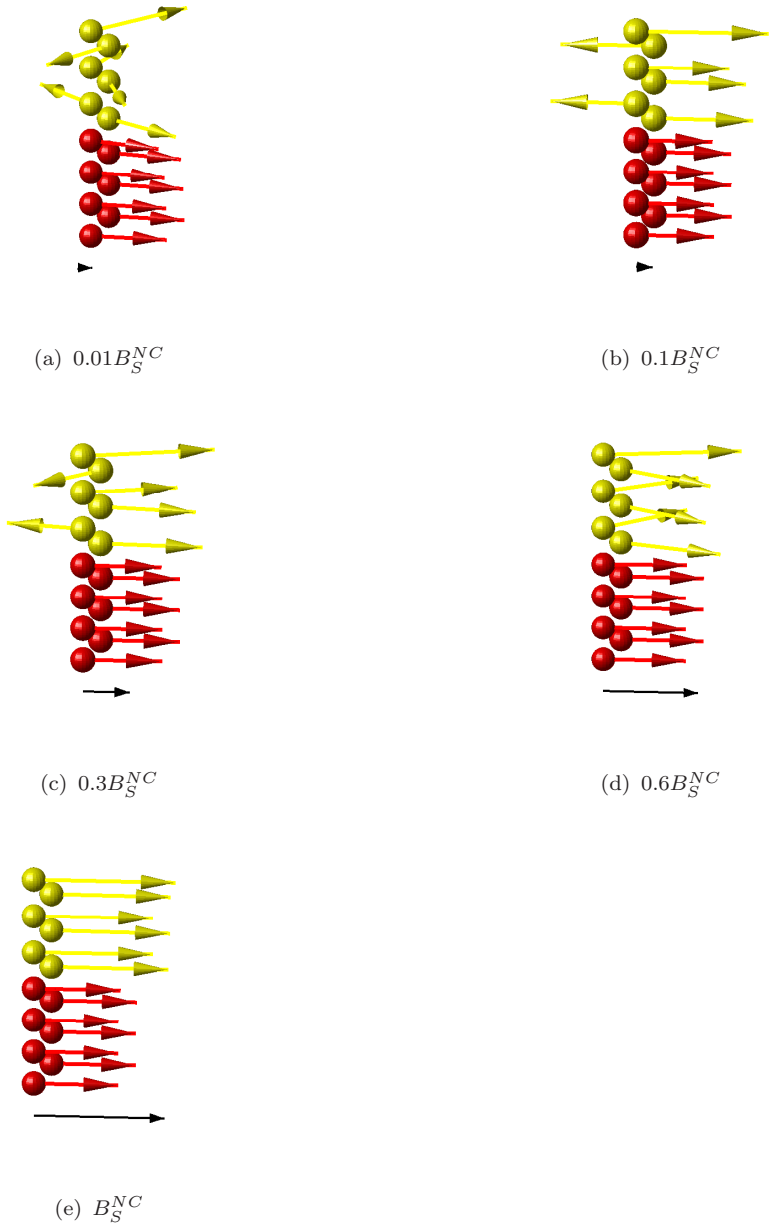

(a) $0.01B_S^{NC}$ (b) $0.1B_S^{NC}$

(c) $0.3B_S^{NC}$ (d) $0.6B_S^{NC}$

(e) B_S^{NC}

FIGURE 3.9: Selected noncollinear magnetic configurations corresponding to different values of the uniform external magnetic field applied in the z direction. One atom per (001) layer is shown. The Mn atoms are represented by yellow balls while the Fe atoms are represented by red balls. The arrows are proportional to the local magnetic moments, and the direction of the magnetization in the Fe bulk is parallel to the external field which is represented by the black vector under each figure.

The very different behavior of the system in collinear or noncollinear frameworks emphasizes the necessity of using the latter one when studying in a realistic manner systems like the one investigated here.

3.6 Conclusion

We have studied the system of 6 Mn layers supported on Fe(001) substrate both in collinear and noncollinear frameworks using our semiempirical TB method. As expected, due to the complex magnetic properties of Mn, we obtain 23 collinear configurations in the Mn layers. The ground state is the layered antiferromagnetic configuration, $-+-+-+$. We subsequently apply external magnetic fields to the ground state and the state 4, $+-+--+$. As the fields increase, there are reversible regions accompanied by sudden jumps between them. The saturation field is very huge, about 14×10^3 T, because to convert the antiferromagnetic coupling to ferromagnetic coupling must cost high energy, and the magnetic moments can only reduce in magnitude and change signs to achieve the saturation.

When the constraint of collinearity is released, we obtain only one noncollinear magnetic configuration in the absence of external magnetic fields. Although the magnetic moment of the Mn surface is 90 degrees coupled with the Fe substrate, local antiparallel coupling in Mn layers and Mn/Fe interface preserves. When external magnetic fields are applied, the magnetic moments can rotate to reach the saturation. As expected, the saturation field is much smaller (about 9.4×10^3 T) than that in the collinear case, but still high compared to the magnetic fields in experiment.

The different behavior of the system of 6 Mn layers on Fe substrate in collinear and noncollinear frameworks indicates the latter one is more basic in nature. However, due to the huge magnetic field, there is no application possibility of our calculations in the Mn/Fe(001) system. But experimentally reasonable systems may be studied in the same line using our TB method.

Chapter 4

Cr on a Stepped Fe Substrate

4.1 Introduction

In the previous chapter, we have shown the noncollinear magnetic structure and its response to external magnetic fields in the system of 6 Mn layers deposited on Fe substrate, in which the complex nature of Mn and the competition of ferromagnetic and antiferromagnetic interactions provide the magnetic frustration. We will investigate, in this chapter, the typical antiferromagnet Cr supported on Fe substrates, firstly the analogous structure of the Mn/Fe(001) system, then Cr on a stepped Fe substrate, and then Cr lines are added on the top gradually. The stepped system and added lines are studied based on two considerations: one is that the system with a smooth Cr-Fe interface may not be complex enough to cause noncollinear frustration because the magnetic property of Cr is not so complex as Mn, so geometrically more frustrated structure may be needed to induce noncollinearity in Cr/Fe system; the other is from the experimental point of view, the deposition of one material on another material carried out in laboratory is often associated with defects, such as steps and islands.

The systems containing Fe and Cr have been studied extensively in recent years because of their interesting properties, which have potential technological applications, such as the giant magnetoresistance [65, 66] and the exchange coupling

in multilayers [136–140]. Furthermore, the existence of noncollinear magnetic systems has been demonstrated both experimentally in multilayers and Cr/Fe alloys [141, 142] and by theoretical calculations in multilayers [58, 143].

Vega *et al* [57] studied the system of Cr monolayer deposited on Fe(001) with a step of monoatomic height using a simple method, in which the authors only considered the d electrons and collinear magnetic moments. They found collinear magnetic frustration and several different solutions present in that system, which are two clear indications of the existence of noncollinearity. Robles *et al* [130] confirmed these predictions later in the noncollinear framework. We will study this system under external magnetic fields.

The experimental studies of Cr/Fe systems present interesting results, especially when related to the magnetization in the systems of surfaces coated with small Cr clusters, interlayer antiferromagnetic order of Cr, and the magnitude moment of Cr. The experimental results of the scanning electron microscopy with polarization analysis shows a large decrease in the magnetization on the surface of Cr/Fe(001) when 0.1 monolayer of Cr is deposited [136, 144]. In other studies, however, a much higher value of the deposited Cr than that of the solid Cr, 4.5 μ_B [145], is obtained. The photoemission measurements of Cr/Fe(001) interface show that the Cr layers are aligned antiferromagneticly on Fe substrate [146, 147]. This could imply that when two Fe films are separated by an odd number of layers of Cr, they would be ferromagneticly coupled. But other different measurements show an ferromagnetic coupling between two Fe films when they are separated by an even number of Cr monolayers [148], which also yields an oscillatory behavior below 20 layers. The average value of the magnetic moment of Cr in a Cr monolayer supported on Fe(001) according to different experiments ranges from zero [149] to large values of the solid Cr [146] or three times of this value [150]. All these features may be due to interdiffusion effects in the Cr/Fe interface [151]. These effects could lead to the magnetic frustration.

In this chapter we investigate the system of a Cr monolayer deposited on the stepped Fe substrate in the [001] direction, shown in Figure 4.1, and several (from

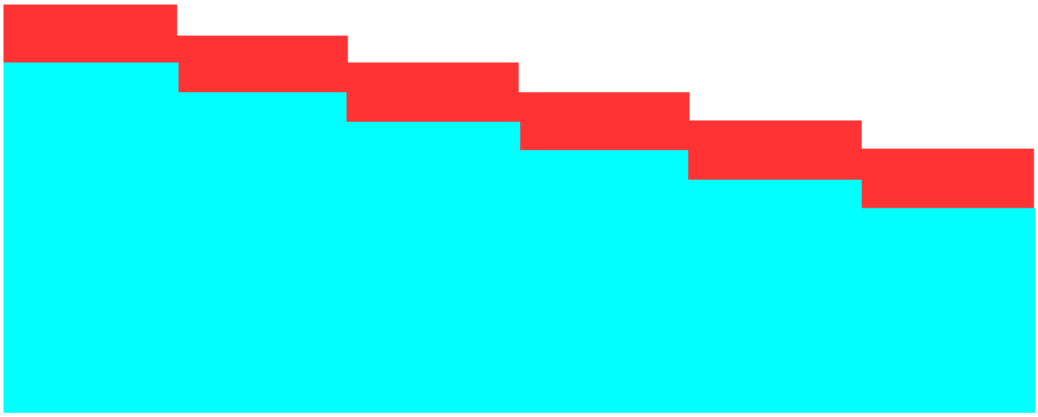

FIGURE 4.1: Schematic diagram of the system of a Cr (red) monolayer deposited on the stepped Fe (blue) substrate.

one through four) Cr lines are added subsequently on the surface of this system, the case of four additional Cr lines corresponds to two Cr layers on the stepped Fe substrate. Firstly, the situations without external magnetic field are calculated for each system, and then magnetic fields are introduced and increased up to their magnetic saturations.

4.2 Parametrization

The parameters of Fe considered for the calculations in Cr/Fe step systems coincide with those of the previous chapter in the Mn/Fe system. For Cr, we use the method described in Section 2.3.7 to obtain the parameters in GCN. The procedure runs as follows. Firstly, The TB-LMTO calculations for solid and the free monolayers and bilayers in different crystallographic orientations are performed. From these calculations the band centers $\epsilon_{i,\alpha}^{0,ref}$ are obtained which are listed in Table 4.1.

Table 4.2 presents the parameters of Cr for the GCN in a fit to Cr solid, monolayer and bilayers (SMB) and a free Cr bilayer. As can be seen in the previous chapter, these parameters between different materials, although the differences are significant, are of the same order of magnitude. After a series of tests, comparing the results obtained by TB method and TB-LMTO method, we choose the parameters of Cr that are fitted from Cr solid, monolayer and bilayers.

	$\epsilon_s^{0,ref}$	$\epsilon_p^{0,ref}$	$\epsilon_d^{0,ref}$	N_s	N_p	N_d	N_{tot}
solid	5.07	9.34	0.87	0.62	0.83	4.55	6.00
monolayer(001)	1.02	4.68	−5.10	0.41	0.14	4.39	4.95
monolayer(110)	−0.11	4.05	−5.46	0.55	0.38	4.56	5.48
monolayer(111)	2.95	6.32	−3.68	0.28	0.05	4.30	4.62
bilayer(001)	0.02	3.75	−4.88	0.57	0.43	4.61	5.61
bilayer(110)	−0.43	3.63	−5.04	0.60	0.60	4.61	5.81
bilayer(111)	1.53	5.26	−4.23	0.51	0.22	4.51	5.25

TABLE 4.1: Values of the band centers (in units of eV) and charges in various Cr systems.

(eV)	$\epsilon_s^{0,at}$	$\epsilon_p^{0,at}$	$\epsilon_d^{0,at}$	ξ_s	ξ_p	ξ_d
SMB	−7.84	−4.34	−24.95	−0.12	−0.03	0.04
bilayer	−5.98	−2.62	−23.28	−0.80	−0.70	−0.60

TABLE 4.2: Parameters of Cr for GCN from the fit of solid, monolayers and bilayers(SMB) and a free bilayer.

The hopping integrals $t_{ij}^{\alpha\beta}$ and the exchange parameter J_{dd} are taken from a fit in TB calculations of Cr multilayers on Fe. The exchange parameter is chosen to a value of 1.08 eV which, although is not a perfect result, is suitable for the treatment of the whole system.

4.3 Collinear results

4.3.1 6 layers of Cr on smooth Fe substrate

For comparison, we firstly carried out the calculations of 6 Cr monolayers deposited on Fe(001) substrate in the collinear framework, similar to what we did for the Mn/Fe(001) system. Nothing in surprise happened, 64 initial magnetic configurations converge to only one result, $+-+-+-$ (in the same notation of the previous chapter). This implies that the collinear layered antiferromagnetic configuration is the natural coupling. We next study more complex structures of the Cr/Fe system, in which the Fe substrate contains a stepped structure. Magnetic frustrations may emerge in such systems.

4.3.2 Intrinsic magnetic properties of Cr on stepped Fe substrate

Now we will study the systems shown in Fig. 4.1. Each step contains four rows of Cr atoms. Then additional rows of Cr atoms are added one by one on the top, from one row to four rows. When four additional rows of Cr atoms are added, it is really the case of two monolayers of Cr.

In this section, we show the results of the intrinsic magnetic properties of the Cr/Fe stepped systems without external magnetic field. As discussed before, the geometrically frustrated structures should result in noncollinear magnetic configurations in the step area. But the local antiferromagnetic coupling among the corner Cr rows are relatively preserved. The results are presented in the following paragraphs.

Cr monolayer

Let us start with the case of pure Cr step on Fe substrate. The noncollinear configuration is shown in Figure 4.2. Although the magnetic frustration occurs due to the step, local antiferromagnetic couplings between Cr rows 1, 2, 3 and Fe rows 6,7,8 preserve almost perfectly. While Cr row 4 at the corner of the step is approximately antiparallel coupled with the adjacent Cr row on the lower step, it can not preserve parallel coupling with the Cr rows on the same step. The magnitudes and directions of the magnetic moments of the most frustrated block of Cr and Fe rows marked with numbers from 1 to 8 in Figure 4.2 are shown in Table 4.3. Due to the effect of lack of coordination, the magnetic moments of rows 2,3 and 4 are larger than that of row 1. The moments of Fe substrate do not vary significantly from the bulk Fe, and they are not canted drastically. For Fe atoms, row 8 is the most frustrated, since it is surrounded by three Cr rows, compared to two Cr rows for Fe rows 5, 6 and 7. This is reflected by the canted angle. Row 8 has the biggest angle, 40°, in the Fe substrate.

One additional Cr row

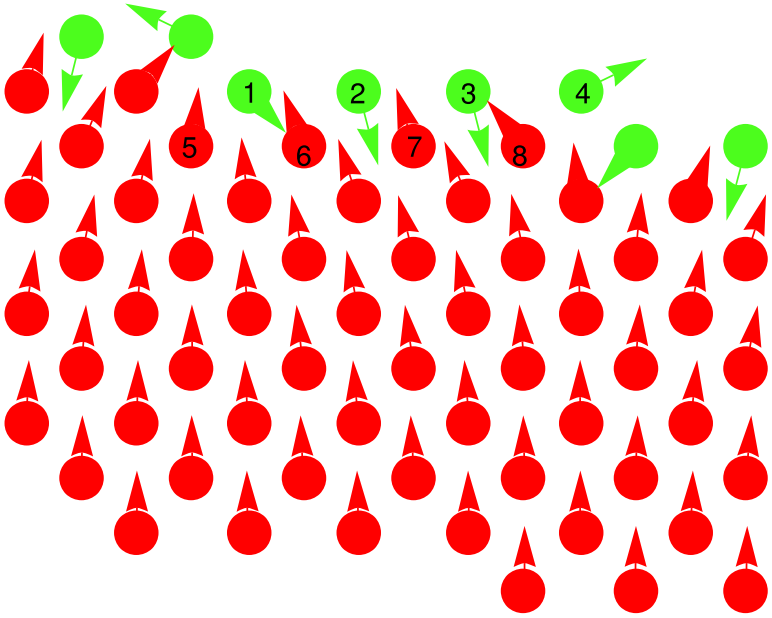

FIGURE 4.2: Noncollinear magnetic configuration of the system of a Cr monolayer on the stepped Fe[001] substrate. The Cr atoms are represented by green circles and the Fe atoms are represented by red circles. The local magnetic moments are shown by arrows. The size of the arrows is proportional to the local magnetic moments.

atom	moment(μ_B)	angle(degree)
1	2.05	137.36
2	2.77	165.01
3	2.81	165.77
4	2.70	64.02
5	2.16	5.95
6	2.16	-19.24
7	2.21	-16.74
8	2.16	-39.17

TABLE 4.3: Magnetic moments and angles of selected rows shown in Figure 4.2.

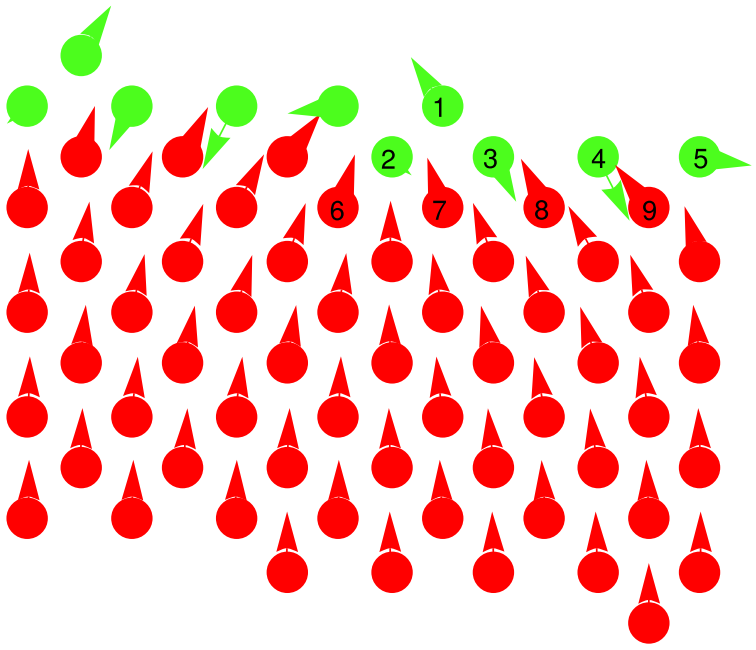

FIGURE 4.3: Noncollinear magnetic configuration of one additional Cr row on the Cr/Fe step system.

atom	moment(μ_B)	angle(degree)
1	2.22	-32.89
2	1.09	130.38
3	1.93	153.35
4	2.76	152.97
5	2.00	99.08
6	2.20	16.65
7	2.07	-16.10
8	2.16	-26.19
9	2.15	-37.51

TABLE 4.4: Magnetic moments and angles of selected rows shown in Figure 4.3.

In Figure 4.3, we present the magnetic configuration of the system of one additional Cr row (row 1) on the Cr/Fe step system. The magnitudes and directions of the magnetic moments of selected rows are listed in Table 4.4. One can observe that due to the additional row 1, the local environment of Cr rows 2, 3 and 5 change essentially. Row 2 is now largely frustrated, its magnetic moment reduces from 2.05 μ_B in the case of pure step system to 1.09 μ_B. However, the local antiferromagnetic coupling between the Cr layer and the lower Fe layer is relatively preserved.

Two additional Cr rows

In the case of two additional Cr rows are deposited on the Cr/Fe step system, shown in Figure 4.4, the rows 3 and 4 are influenced more significantly than the case of one additional Cr row is added. In Table 4.5, we can see the magnetic moment of row 3 reduces further to 1.01 μ_B. Rows 4 and 5 are also affected by the additional rows, but row 6 remains almost unchanged both in magnitude and in direction of the magnetic moment. Approximately layered antiparallel coupling between the Cr layer and adjacent Fe layer still remains beside atom 6.

Three additional Cr rows

Introducing one more additional Cr row on the Cr/Fe step system, we obtain the structure in Figure 4.5. As expected, the Cr rows 4, 5 and 6 are further frustrated. The magnitudes and directions of the magnetic moments of selected rows shown in Table 4.6 verify this trend. Their magnetic moments reduce to 0.88 μ_B, 1.13 μ_B and 1.23 μ_B from 1.01 μ_B, 1.26 μ_B and 1.95 μ_B in the case of two additional Cr rows are added, respectively. It is worthwhile to point out that the magnetic moment of row 7 rotates and reduces drastically, the magnitude of magnetic moment from 2.00 μ_B to 1.33 μ_B, and the direction from 92° to −128°. Since the introduction of row 3, row 6 becomes an inner row similar to rows 4 and 5. This demonstrates the significant influence of numbers of coordinations, i.e., local electronic environment, to the properties of atoms in solid.

Four additional Cr rows (two Cr monolayers)

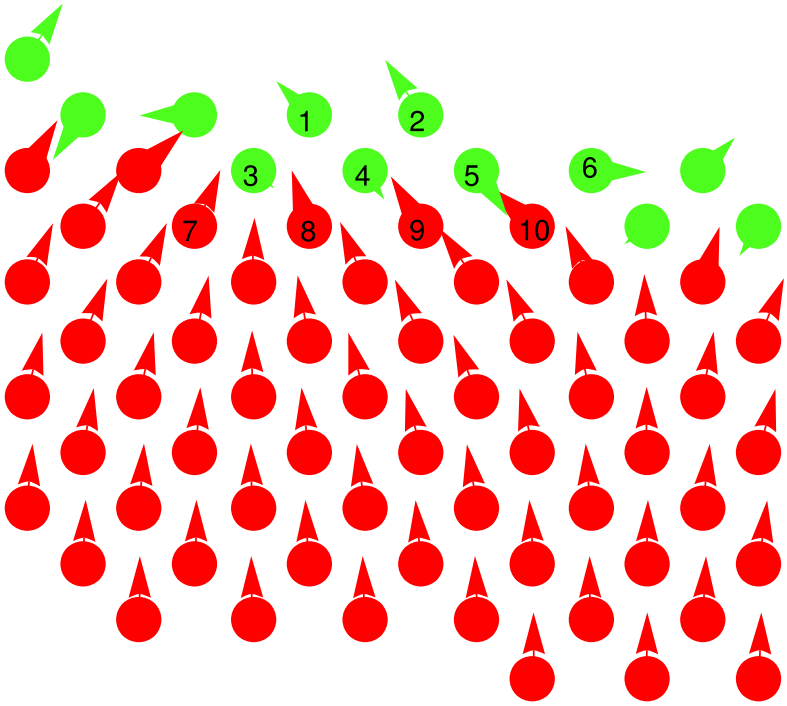

FIGURE 4.4: Noncollinear magnetic configuration of two additional Cr rows on the Cr/Fe step system.

atom	moment(μ_B)	angle(degree)
1	1.63	-44.38
2	2.31	-33.56
3	1.01	128.56
4	1.26	146.05
5	1.95	146.61
6	2.00	91.65
7	2.20	23.41
8	2.09	-16.48
9	2.08	-31.21
10	2.11	-47.85

TABLE 4.5: Magnetic moments and angles of selected rows shown in Figure 4.4.

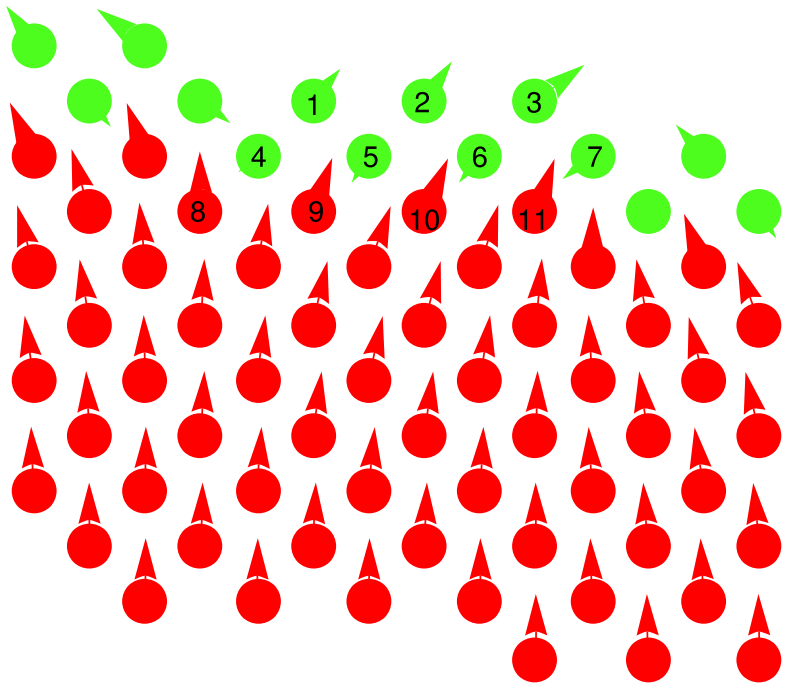

FIGURE 4.5: Noncollinear magnetic configuration of three additional Cr rows on the Cr/Fe step system.

atom	moment(μ_B)	angle(degree)
1	1.50	41.38
2	1.70	35.31
3	2.15	53.87
4	0.88	-131.25
5	1.13	-147.55
6	1.23	-141.15
7	1.33	-128.30
8	2.17	-1.27
9	2.05	19.94
10	2.10	23.83
11	2.01	19.29

TABLE 4.6: Magnetic moments and angles of selected rows shown in Figure 4.5.

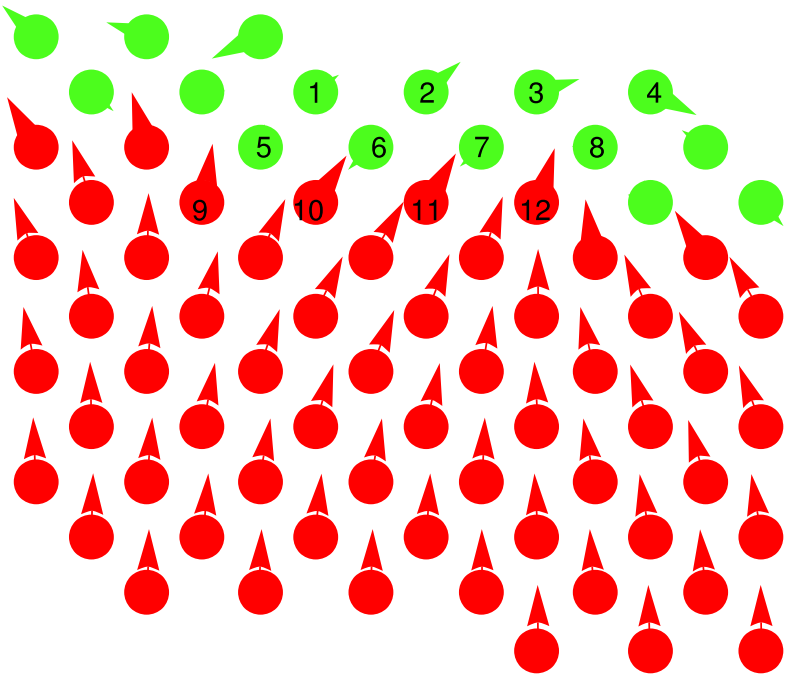

FIGURE 4.6: Noncollinear magnetic configuration of four additional Cr rows (two monolayers of Cr) on the Cr/Fe step system.

atom	moment(μ_B)	angle(degree)
1	1.05	55.86
2	1.61	49.32
3	1.54	73.47
4	1.88	117.13
5	0.75	-138.10
6	1.14	-135.43
7	1.07	-131.01
8	0.79	-88.27
9	2.14	9.19
10	2.04	33.87
11	2.06	30.84
12	2.04	16.88

TABLE 4.7: Magnetic moments and angles of selected rows shown in Figure 4.6.

When four addtional Cr rows are deposited on the Cr/Fe step system, it is actually a system with two layers of Cr coverage. The antiferromagnetic coupling between Cr layers which is similar to the case of bulk Cr is approximately preserved. The sublayer which consists of rows 5, 6, 7 and 8 is covered by another complete layer of Cr atoms, so their magnetic moments are reduced once more, see Table 4.7.

As a short conclusion of the magnetic properties of above Cr/Fe step systems without external magnetic fields, we summarize the common features in these systems. Firstly, the local antiferromagnetic couplings between Cr layers and between Cr layer and adjacent Fe layer are approximately preserved except for the corner Cr rows which possess different local electronic environments. Secondly, Fe substrates are affected but not significantly by the Cr coverage. That is, only slight rotations of magnetic moments of Fe atoms occur, no flip appears. Furthermore, as more additional Cr rows are added, the inner Cr atoms are frustrated more evidently. But the surface Cr atoms always carry stronger magnetic moments, since they are lack of coordinations with respect to the inner Cr atoms.

4.4 Response to external magnetic fields

When external agents (for example, external magnetic fields) are applied to the magnetically frustrated system, the magnetic moments would rotate rather than flip to align with the external field in the noncollinear framework. As can be seen in our calculation of Mn/Fe(001) system and the experiment result of $CdCr_2O_4$ [135], a collinear region appears in the evolution of magnetic moments under applied magnetic fields. Is this a common feature for all noncollinear systems? We will answer this question after we have investigated the response of the Cr/Fe step systems to external magnetic fields. Due to the saturation magnetic fields are still huge in the Cr/Fe step systems, typically more than 10000 T, we choose an increment of 200 T as the field increases.

Cr monolayer

In the case of pure one monolayer Cr step on Fe substrate, we start from the noncollinear configuration shown in Figure 4.2 and increase the magnetic field gradually up to the magnetic saturation at $B_S = 10800\ T$. The evolutions of magnitudes and directions of the magnetic moments of the 4 inequivalent Cr atoms are shown in Figure 4.7. In panel (b) of Figure 4.7, there is no collinear configuration during the noncollinear evolution, i.e., no jump of angles from 180° to 0° appears. The directions of magnetic moments of Cr atoms rotate smoothly to align with the Fe substrate. This example answers the question posed previously: it is not necessary for a magnetically frustrated system to go through one or more collinear configurations to reach the magnetic saturation. The collinear configuration only appears when there is a barrier to rotate the magnetic moment, that is, the collinear configuration is the one with lowest energy when certain external magnetic fields are applied. After overcoming the barrier, the system would jump to a noncollinear configuration again, and continue rotating other magnetic moments.

One additional Cr row

Different from the situation in the system of pure one Cr monolayer on the stepped Fe substrate, the case of one addtional Cr row on the Cr/Fe step system is more complicated. One can see in Figure 4.8, at 9600 T (0.6 B_S, where the saturation field $B_S = 16000\ T$.) the magnetic moment of row 2 is antiparallel to the Fe substrate, i.e., the angle in panel (b) is 180°. At this point, the system is collinear. As the magnetic field continues increasing, the magnetic moment of row 2 does not rotate, its magnitude reduces to zero at 12000 T (0.75 B_S), see panel (a), and then increases in the opposite direction until the magnetic saturation at $16000T$. As discussed in the case without external magnetic fields, row 2 is fully surrounded by Cr and Fe atoms, it tends to have the similar properties of the smooth Cr/Fe system, which is collinear, when certain external magnetic fields are applied.

Two additional Cr rows

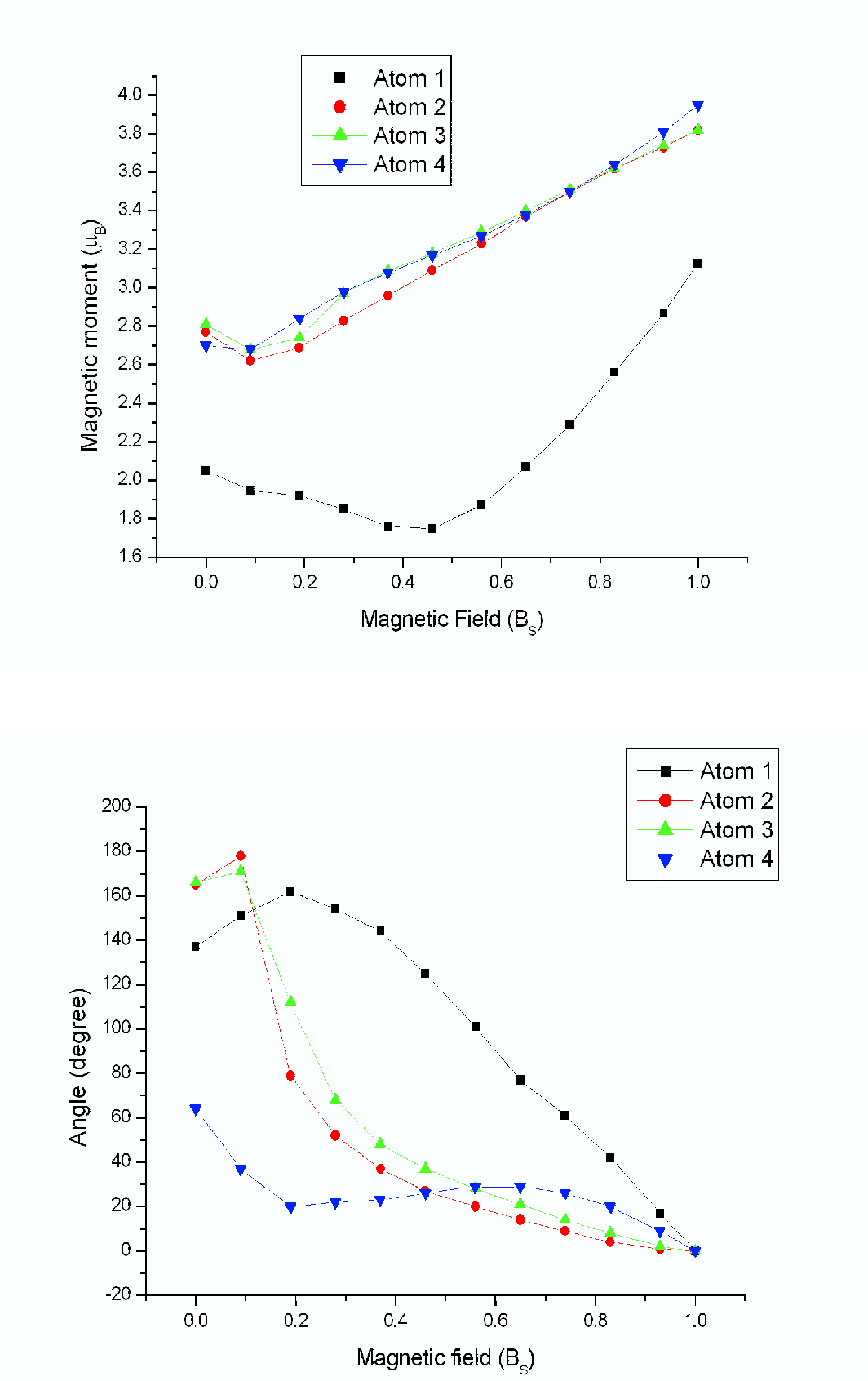

(b)

FIGURE 4.7: Evolution of the magnitudes (a) and directions (b) of the magnetic moments of Cr rows under external magnetic fields in the system of a pure Cr monolayer on the stepped Fe substrate. The atom labels correspond to those shown in Fig. 4.2. The saturation magnetic field $B_S = 10800\ T$.

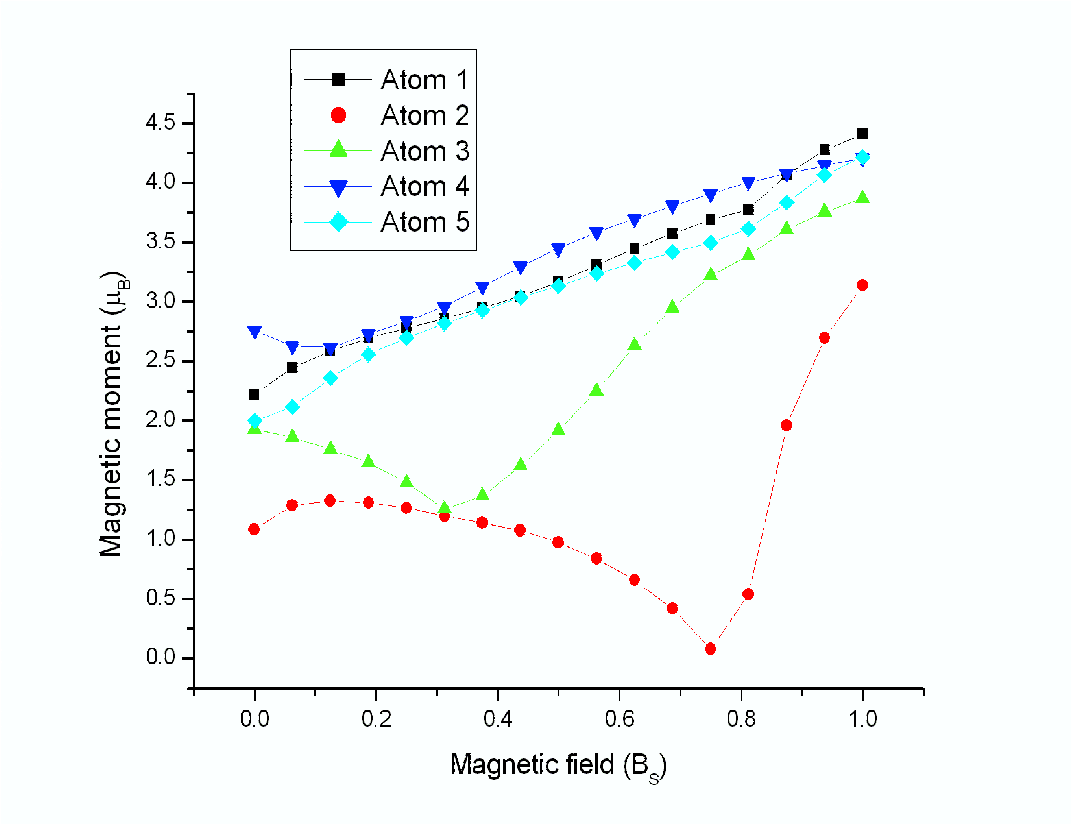

(a)

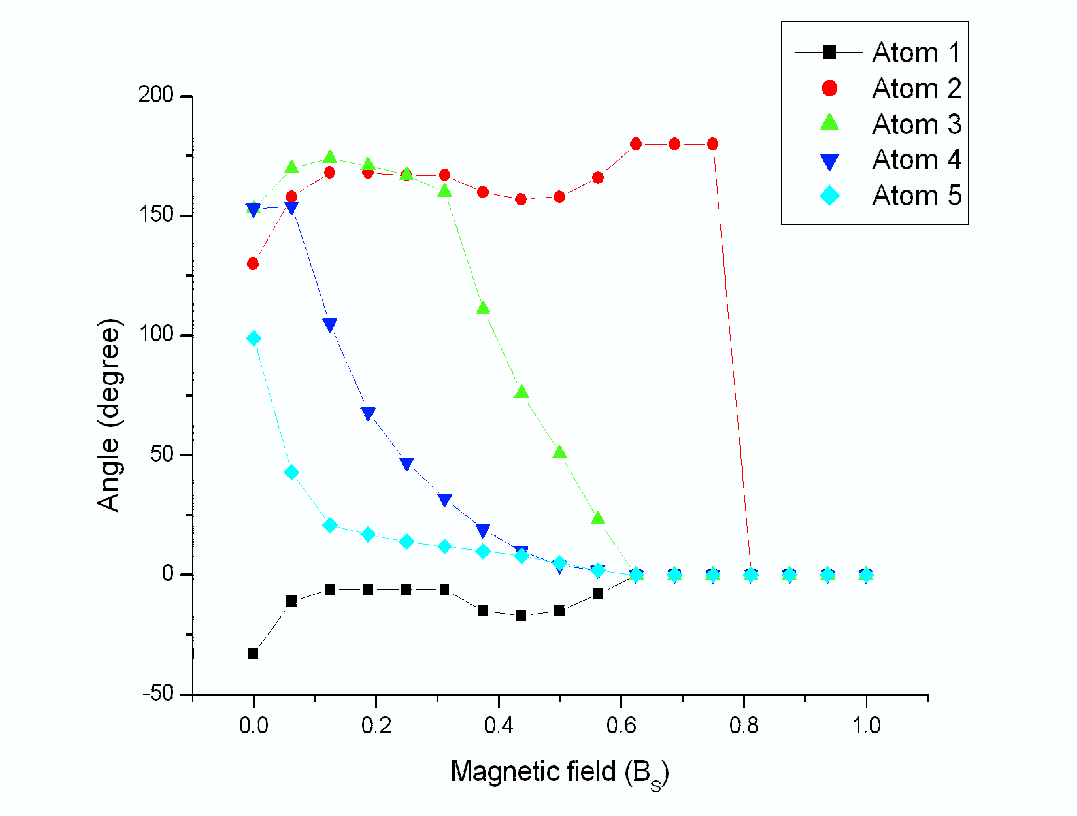

(b)

FIGURE 4.8: As in Fig. 4.7 for the system represented in Fig. 4.3. The saturation magnetic field $B_S = 16000\ T$.

The case of two additional Cr rows on the Cr/Fe step system is even more complicated. As shown in Figure 4.9, to reach the magnetic saturation at $B_S = 15000\ T$, there are two collinear regions to overcome. One is between 2000 T (0.13 B_S) and 7000 T (0.47 B_S), in which the magnetic moments of rows 3, 4 and 5 are antiparallel to the moment of Fe substrate. Their magnetic moment decrease until the system changes to noncollinear configuration at 7000 T. When the magnetic field increases to 9600 T (0.64 B_S), the magnetic moment of row 5 rotates to be parallel to the moment of Fe substrate, the system enters into collinear configuration again. Until 11800 T (0.79 B_S), the magnetic moments of rows 3 and 4 rotate quickly to align parallelly to the moment of Fe substrate. Then the magnetic moment at each site increases up to the saturation at 15000 T.

Three additional Cr rows

For the structure of three additional Cr rows on the Cr/Fe step system, Figure 4.10 shows the evolutions of the magnitudes and directions of the magnetic moments Cr atoms under external magnetic fields. This system saturates at $B_S = 16000\ T$. When external magnetic field is applied, the system jumps to a collinear configuration very soon at 400 T (0.025 B_S). In the collinear region, row 7 flips to parallel to the reference direction (the direction of the magnetic moment of the Fe substrate) at 5000 T (0.31 B_S), followed by the flip of row 4 at 8400 T (0.53 B_S). At 10200 T, the system changes to noncollinear configuration until all the magnetic moments align parallelly to the reference direction at 14000 T (0.875 B_S).

Four additional Cr rows (tow Cr monolayers)

For the system of two Cr monolayers deposited on the Fe substrate, a large collinear region appears from 2000 T through 10600 T, in which the magnetic moments of rows 2, 3, 4 are parallel to the reference direction (the direction of the magnetic moment of Fe substrate), while other rows are antiparallel to this direction at first. Rows 1 and 5 flips to align with the reference direction at 4000 T, and then atom 6 flips at 8000 T. The collinear evolution ends at 10600 T, then

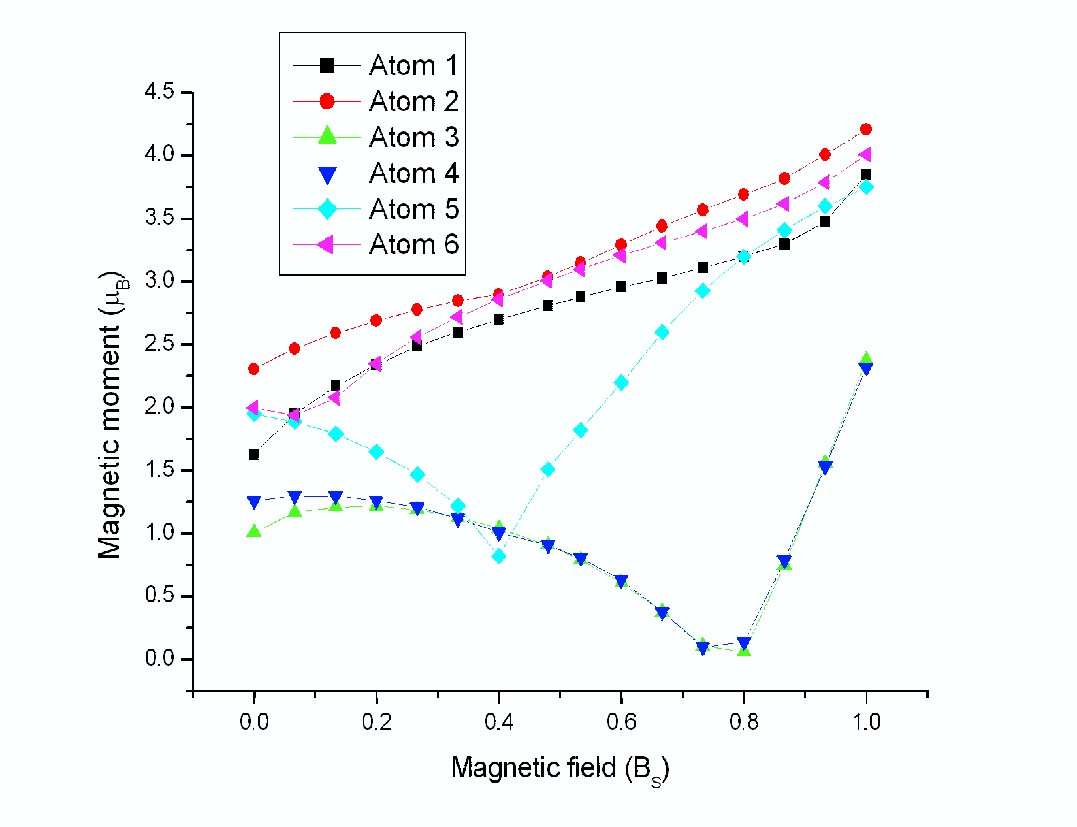

(a)

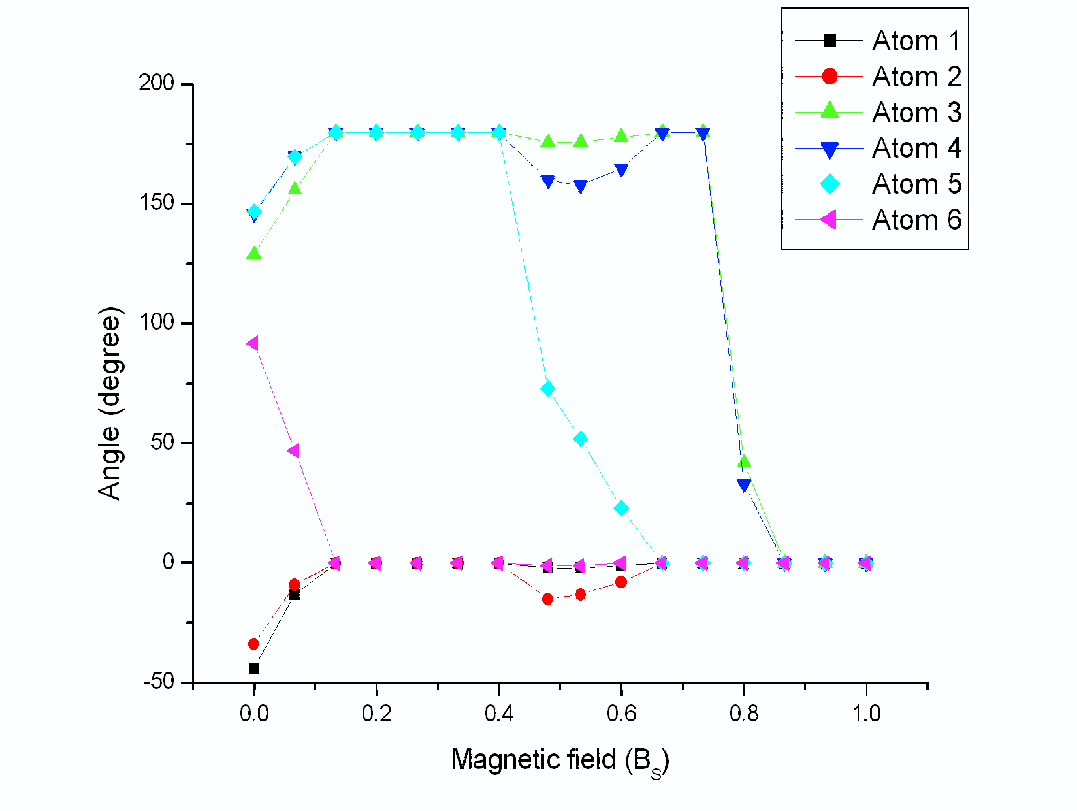

(b)

FIGURE 4.9: As in Fig. 4.7 for the system represented in Fig. 4.4. The saturation magnetic field $B_S = 15000\ T$.

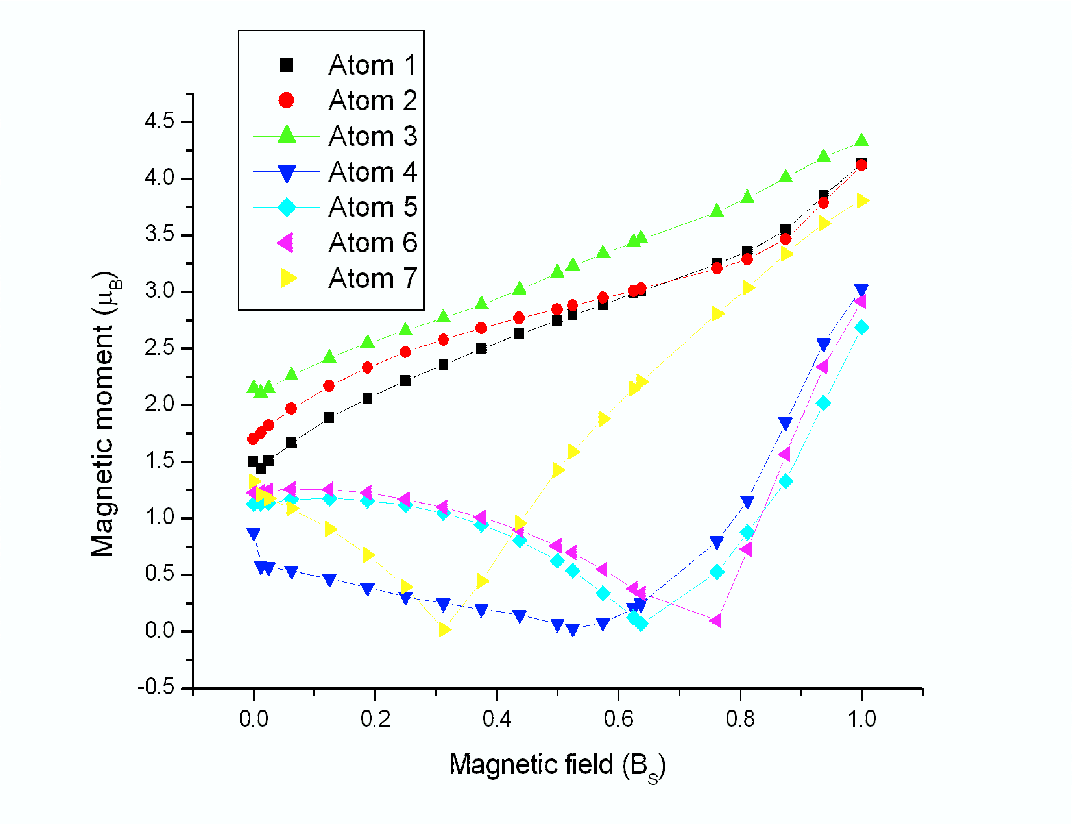

(a)

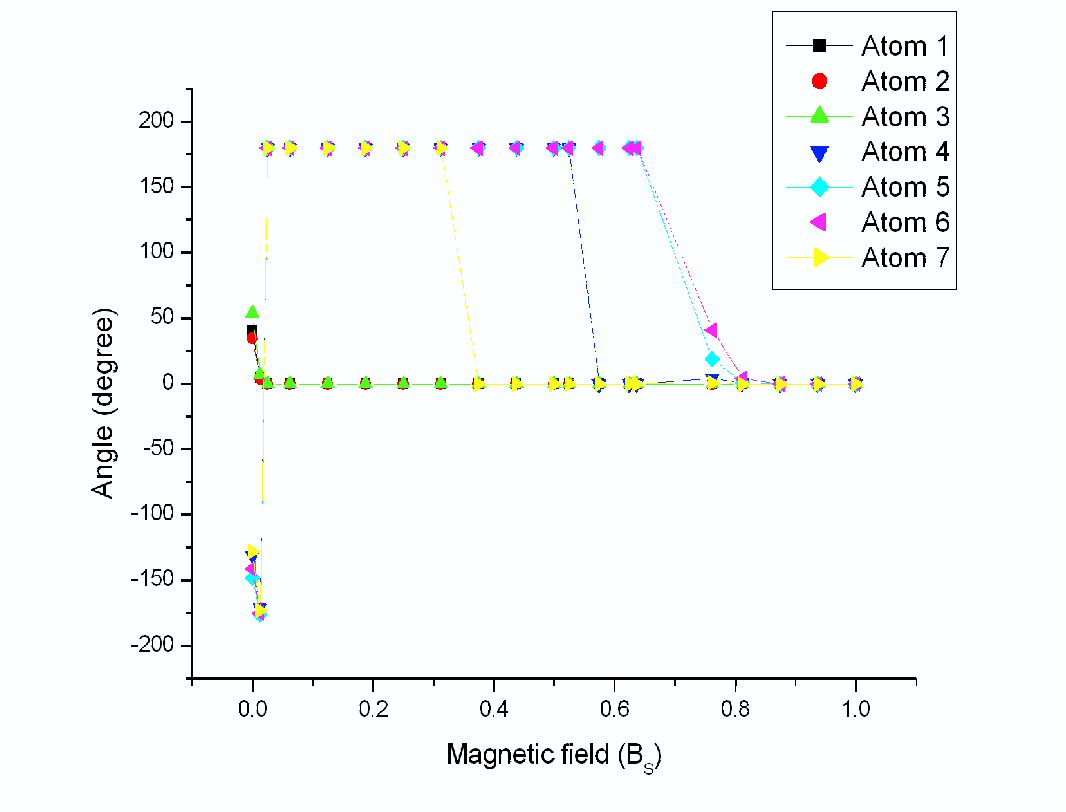

(b)

FIGURE 4.10: As in Fig. 4.7 for the system represented in Fig. 4.5. The saturation magnetic field $B_S = 16000\ T$.

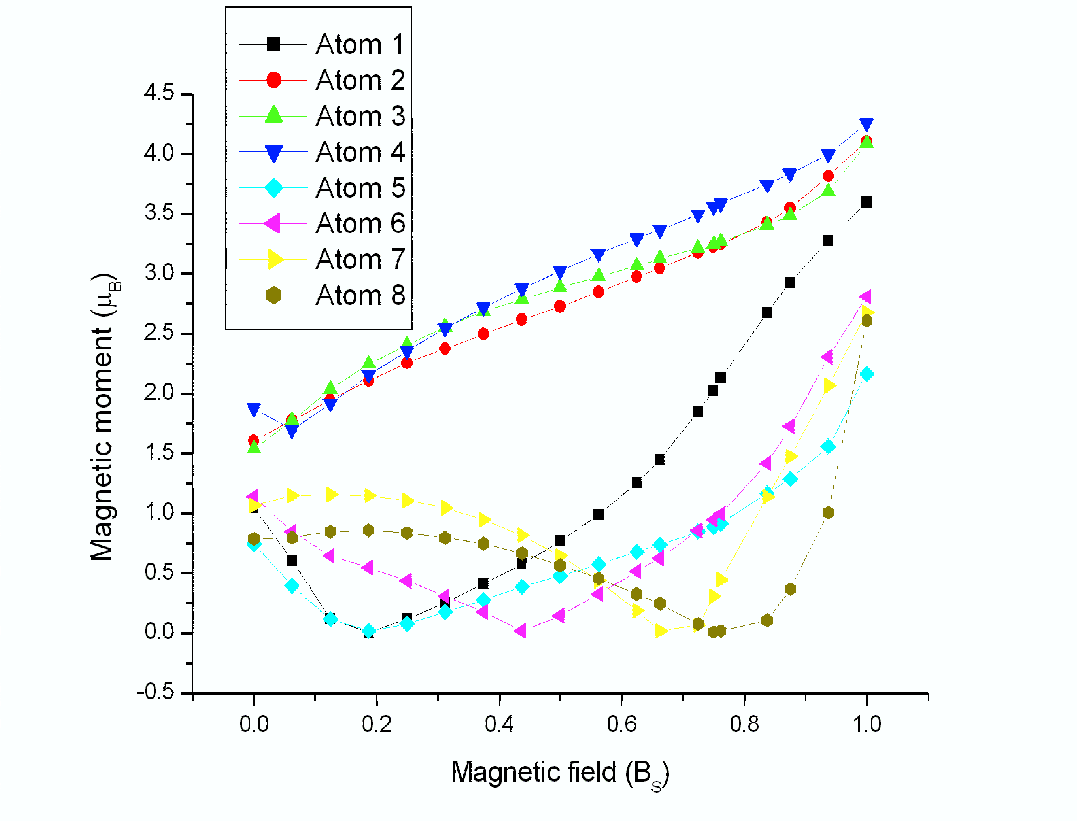

(a)

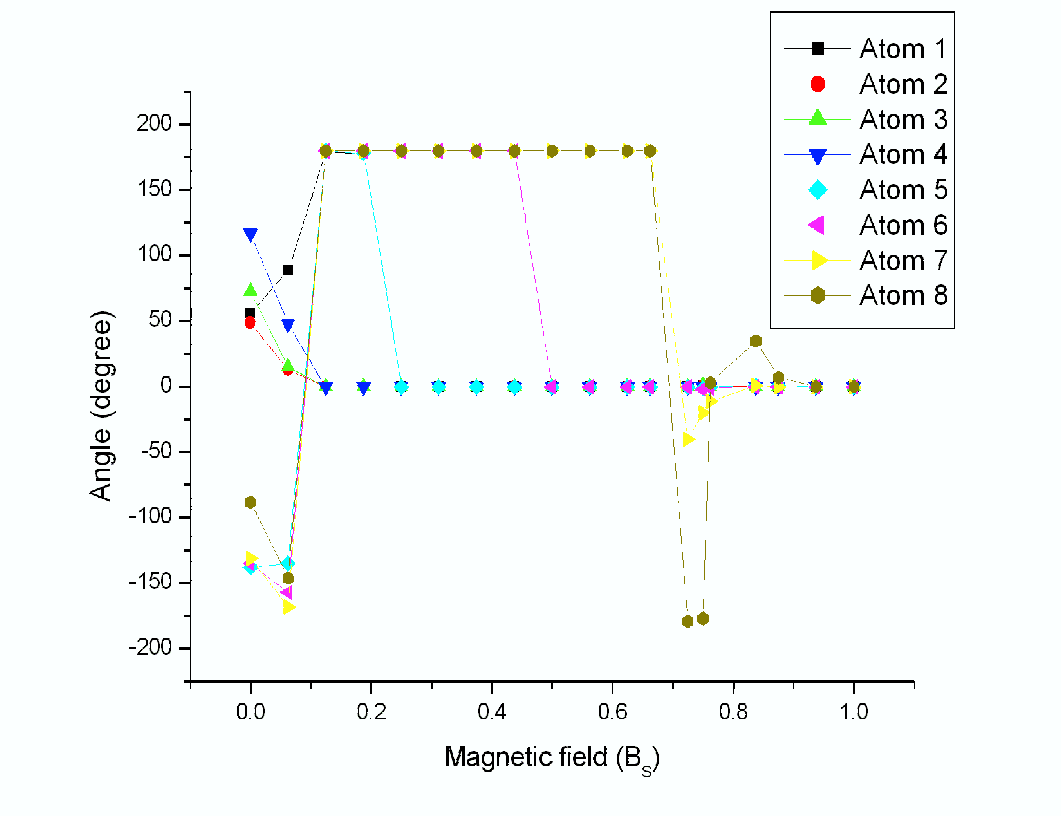

(b)

FIGURE 4.11: As in Fig. 4.7 for the system represented in Fig. 4.6. The saturation magnetic field $B_S = 16000\ T$.

in a noncollinear evolution the magnetic moments of rows 7 and 8 rotate to be parallel to the reference direction at 15000 T.

To summarize, we know that the system of Fe monolayers on smooth Cr(001) substrate has a collinear configuration. The chemical unparity of Cr and Fe does not induce a noncollinear configuration at the smooth interface. When the Fe substrate has a step, the magnetic frustration happens heavily in the step area. But locally antiferromagnetic coupling between Cr and Fe atoms is relatively preserved. Due to the strong coupling between Cr atoms and between Fe and Cr atoms, the external magnetic field needed to align all the magnetic moments with the field is huge. When more and more additional Cr rows are added on the top of the Cr/Fe step system, the number of inner Cr atoms increases, and their magnetic properties approach the smooth Cr/Fe system, that is, the collinear evolution of the magnetic moment under external magnetic fields.

4.5 Conclusion

In this chapter we have studied the system of 6 Cr monolayers on Fe(001) substrate and Cr deposited on the stepped Fe(001) substrate in the noncollinear framework using our semiempirical TB method. The natural coupling between Cr and Fe is strong and antiferromagnetic. The noncollinear calculation of the 6Cr/Fe system results in a collinear antiferromagnetic configuration, which is very different from the 6Mn/Fe system discussed in the previous Chapter.

The Cr/Fe step system is a complicated system which has both geometric frustration, the step, and chemical frustration, the Cr and Fe neighbors. Magnetic frustrations happen in the step area, especially at the corner of the step due to the lack of coordinations. But approximately local antiferromagnetic coupling preserves between the Cr and Fe interface except the corner Cr atoms. When additional Cr rows are added from one row to four rows on the top, some of the previous surface Cr atoms become “inner” atoms, and their magnetic properties tend to be like the atoms in the smooth Cr/Fe interface. After external magnetic

fields are applied, the evolution of the magnetic moments in the system of one Cr monolayer on stepped Fe substrate is totally noncollinear. However, in the systems with additional Cr rows collinear regions appear in the evolution of magnetic moments. The more Cr rows are added, the larger the collinear regions.

Chapter 5

Conclusions

In this thesis we used the semi-empirical TB method in combination with the *ab initio* TB-LMTO method for the electronic structure and magnetic properties in the system of 6 Mn(Cr) layers supported on Fe(001) and the Cr/Fe(001) step systems. The TB method employed allows the treatment of noncollinear magnetic configurations. With this method, the calculation of systems with a large number of inequivalent sites is possible in a reasonable time period. We have investigated response of the Mn/Fe(001) system and the Cr/Fe(001) step systems with adatoms to external uniform magnetic fields.

For the Mn/Fe(001) system, we firstly reproduced the calculation in collinear framework and in absence of an external field, we have obtained multiple magnetic configurations in Mn layers, the ground state showing antiparallel couplings between Mn layers and parallel coupling at the Mn/Fe interface. Similar local magnetic couplings have been obtained in the ground state configuration found in the noncollinear framework, although, in this case, the surface magnetic moment is perpendicular to the bulk moment and no other metastable configurations are obtained.

When the external field is applied, there is a competition between the tendencies of the local moments to align themselves with the external field and to preserve their antiparallel exchange coupling. In the collinear case with an external magnetic field only the value of the moments can vary continuously, whereas their

directions can only be changed via spin flip transitions. In the noncollinear approach the local moments can both rotate and change their value continuously. The response in the collinear case shows both smooth and sharp changes of the average magnetic moment of the Mn slab depending on the external field. The smooth changes correspond to reversible variations of a magnetic configuration of the system, while the sharp ones are the result of spin flip transitions between the configurations with different local exchange couplings, and correspond to a non reversible situation. In contrast, a reversible response is always obtained in the noncollinear framework for the full range of applied fields. Therefore, the response of the system is markedly different in both approaches. Due to the non-reversibility obtained in the collinear framework, the external magnetic field can be used to switch the system between different metastable configurations, some of them having very different average magnetic moments. This situation can be achieved in real systems with strong uniaxial anisotropy.

At the beginning of the study of the Cr/Fe system, we start from a comparison of the 6Cr/Fe(001) system with the 6Mn/Fe(001) system. In the noncollinear calculation, we obtain a collinear antiferromagnetic configuration in the Cr slab and the Cr-Fe interface. The chemical unparity does not induce a frustration in the smooth Cr-Fe interface. Then we introduce a geometric breaking, the step, into the Cr/Fe system.

For the Cr/Fe step systems, we compared the noncollinear configurations for the system of one Cr monolayer on the stepped Fe substrate and the systems with several additional Cr rows, from one row to four rows. Local couplings are approximately preserved except for the atoms at the corners of the steps, although magnetic frustrations appear due to the geometric symmetry breaking introduced by the steps. When the number of additional Cr rows increases, the “inner” Cr atoms lose some surface properties and approach the properties of Cr interface in the 6Cr/Fe(001) system. When external magnetic field is applied, the evolution of magnetic moments carries some common features with that observed in the Mn/Fe(001) system. In many systems (except the system of one Cr monolayer on

the stepped Fe substrate) the noncollinear evolution of the magnetic moments under external magnetic fields experiences a collinear region, in which the energy of the collinear configuration under that magnetic field is lower than noncollinear configurations. This phenomenon is demonstrated by recent experimental measures carried out in $CdCr_2O_4$ [135]. When the number of additional Cr rows increases, the collinear region becomes larger and larger. However, the collinear region is not necessary in the evolution of magnetic moments to align with external magnetic fields, e.g., in the system of one Cr monolayer on stepped Fe substrate.

Our method has an advantage of saving computing time. We can simulate relatively large systems with hundreds of inequivalent sites. Because we make many simplifications, this method also has some flaws. The first one is the omission of spin-orbit interaction and the contribution of s and p electrons. Thus, magnetic anisotropy does not present in our results. In transition metals, despite that the most relevant properties are determined mainly by d electrons, s and p electrons also play a role which is not negligible if one wants to give a detailed description. We also do not consider the geometric relaxation of the system. The geometric structure of the system considered is unknown *a priori* and the structure and level of relaxation have a large influence on the electronic properties, especially when external agents (e.g. magnetic fields) are applied. It is therefore important to conduct a structural optimization, which further complicates the calculation. The influence of temperature may also be an important reason that makes our calculated saturation fields extremely high. The experimental result of the saturation field under low temperature, below 26 K, in $CdCr_2O_4$ is 90 T [135]. The temperature fluctuation may make the rotation of magnetic moments easier. Despite of these flaws in our model, we still provide a possibility of studying complex systems with a large number of inequivalent sites in the noncollinear framework, which is almost impossible by using the first principle methods.

Our present study opens new prospects for investigating the response of other complex nanostructures, not only to uniform external magnetic fields, but also to non-uniform fields having different intensity and orientation in different local

parts of the system (even at the atomic scale), a situation that could be managed in experiment in the future.

Appendix A

Haydock's recursion method

Traditional methods of calculating DOS for crystalline solids need calculating Bloch band structure $E(\mathbf{k})$, and then integrating in the reciprocal space up to Fermi surface. These methods require a perfect solid system on an infinite and periodic lattice. When we consider surfaces and interfaces (as in this thesis), or clusters and impurities, a non-Bloch formulation of the electronic structure is required. In this appendix we introduce how to calculate (LDOS) by using Haydock's recursion method [45–47] in the real space. This method enable us to relate the electronic structure to local environment, rather than the regularity and infinite extent of a perfect crystal structure, and solve the Hamiltonian self-consistently without a need for diagonalization.

A.1 Local density of states

Suppose the system we consider can be described by a Hamiltonian $\mathbf{H}$, $\psi_n(\mathbf{r})$ and ε_n are its eigenstates and eigenvalues, respectively. The total density of states can be written as:

$$\rho(\varepsilon) = \sum_n \delta(\varepsilon - \varepsilon_n). \tag{A.1}$$

We could formally define an operator of state density $\delta(\varepsilon - \mathbf{H})$, whose matrix elements are

$$\begin{aligned} & \int d\mathbf{r}\psi^*_{n'}(\mathbf{r})\delta(\varepsilon - \mathbf{H})\psi_n(\mathbf{r}) \\ = & \int d\mathbf{r}\delta(\varepsilon - \varepsilon_n)\psi^*_{n'}(\mathbf{r})\psi_{\mathbf{n}}(\mathbf{r}) \\ = & \delta(\varepsilon - \varepsilon_n)\delta(n, n'), \end{aligned} \tag{A.2}$$

where we used the orthogonal property of eigenstates $\int d\mathbf{r}\psi^*_{n'}(\mathbf{r})\psi_{\mathbf{n}}(\mathbf{r}) = \delta(\mathbf{n}, \mathbf{n}')$. The total DOS, now, can be expressed as the trace of the operator of state density, i.e.

$$\begin{aligned} \mathrm{Tr}\delta(\varepsilon - \mathbf{H}) &= \sum_n \int d\mathbf{r}\psi^*_n(\mathbf{r})\delta(\varepsilon - \mathbf{H})\psi_n(\mathbf{r}) \\ &= \sum_n \delta(\varepsilon - \varepsilon_n) = \rho(\varepsilon). \end{aligned} \tag{A.3}$$

The integrand is defined to be the local density of states in the volume $d\mathbf{r}$ centered at $\mathbf{r}$,

$$\rho(\mathbf{r}, \varepsilon) = \sum_n \psi^*_n(\mathbf{r})\psi_n(\mathbf{r})\delta(\varepsilon - \varepsilon_n). \tag{A.4}$$

We will subsequently relate the local density of states $\rho(\varepsilon, \mathbf{r})$ with the imaginary part of the Green's function. For simplicity, we consider a one-body system. The Green's function is defined by the equation

$$[\varepsilon - \mathbf{H}(\mathbf{r})]\, G(\mathbf{r}, \mathbf{r}'; \varepsilon) = \delta(\mathbf{r} - \mathbf{r}'). \tag{A.5}$$

If we treat the Green's function $G(\mathbf{r}, \mathbf{r}'; \varepsilon)$ as an operator, the above equation has a formal solution

$$\begin{aligned} G(\varepsilon) &= \frac{1}{\varepsilon - \mathbf{H}} \\ &= \frac{1}{\varepsilon - \mathbf{H}} \sum_n |\psi_n\rangle\langle\psi_n| = \sum_n \frac{|\psi_n\rangle\langle\psi_n|}{\varepsilon - \varepsilon_n}. \end{aligned} \tag{A.6}$$

Projecting the operator into the coordinate representation, we obtain

$$G(\mathbf{r},\mathbf{r}';\varepsilon)=\sum_n \frac{\psi_n^*(\mathbf{r})\psi_n(\mathbf{r}')}{\varepsilon-\varepsilon_n}. \tag{A.7}$$

In this definition we must be careful at the sigularities ε_n, where the definition is not well-defined. In order to circumvent these singularities at the real axis, we implement a frequently used trick to add a small imaginary part η in ε. And then after some reorganization procedure, we let η converge to zero. We define two limits of the complex Green's function,

$$G^+(\mathbf{r},\mathbf{r}';\varepsilon)=\lim_{\eta\to 0^+} G^+(\mathbf{r},\mathbf{r}';\varepsilon+i\eta)=\lim_{\eta\to 0^+}\sum_n \frac{\psi_n^*(\mathbf{r})\psi_n(\mathbf{r}')}{\varepsilon+i\eta-\varepsilon_n}, \tag{A.8a}$$

$$G^-(\mathbf{r},\mathbf{r}';\varepsilon)=\lim_{\eta\to 0^+} G^+(\mathbf{r},\mathbf{r}';\varepsilon-i\eta)=\lim_{\eta\to 0^+}\sum_n \frac{\psi_n^*(\mathbf{r})\psi_n(\mathbf{r}')}{\varepsilon-i\eta-\varepsilon_n}. \tag{A.8b}$$

With the help of the identity

$$\lim_{y\to 0^+}\frac{1}{x\pm iy}=\mathscr{P}\frac{1}{x}\mp i\pi\delta(x), \tag{A.9}$$

We explicitly separate the real and imaginary parts,

$$G^\pm(\mathbf{r},\mathbf{r}';\varepsilon)=\mathscr{P}\sum_n \frac{\psi_n^*(\mathbf{r})\psi_n(\mathbf{r}')}{\varepsilon-\varepsilon_n}\mp i\pi\sum_n \psi_n^*(\mathbf{r})\psi_n(\mathbf{r}')\delta(\varepsilon-\varepsilon_n), \tag{A.10}$$

where $\mathscr{P}$ stands for the Cauchy principal value. Comparing equation (A.4) and (A.10), we conclude that the local density of states can be expressed by the imaginary part of Green's function,

$$\rho(\mathbf{r},\varepsilon)=\mp\frac{1}{\pi}\mathrm{Im}G^\pm(\mathbf{r},\mathbf{r};\varepsilon). \tag{A.11}$$

In the following sections we only use the Green's function defined by the right limit, $G^+(\mathbf{r},\mathbf{r}';\varepsilon)$.

In the tight-binding (TB) model, we consider the eigenstates of the whole system as linear combinations of a set of local atomic orbitals $\phi_{\alpha\sigma}(\mathbf{r}-\mathbf{R}_i)$ on site $\mathbf{R}_i$ with

orbital quantum number α and spin σ. So it is more convenient to choose the complete set of local orbitals as the basis of the Hilbert space, then our LDOS comes from a projection of the eigenstates onto a particular orbital,

$$\begin{aligned}
\rho_{\alpha\sigma}(\varepsilon, \mathbf{R}_i) &= \langle i\alpha\sigma|\delta(\varepsilon - \mathbf{H})|i\alpha\sigma\rangle \\
&= \langle i\alpha\sigma|\delta(\varepsilon - \mathbf{H}) \left(\sum_n |\psi_n\rangle\langle\psi_n| \right) |i\alpha\sigma\rangle \\
&= \sum_n |\langle i\alpha\sigma|\psi_n\rangle|^2 \, \delta(\varepsilon - \varepsilon_n) \\
&= \sum_n \left| \int \phi^*_{\alpha\sigma}(\mathbf{r} - \mathbf{R}_i)\psi_n(\mathbf{r}) d\mathbf{r} \right|^2 \delta(\varepsilon - \varepsilon_n). \qquad \text{(A.12)}
\end{aligned}$$

A.2 The recursion method

Now we have converted the problem of solving the LDOS to computing the diagonal elements of the Green's operator $G(\varepsilon) = \frac{1}{\varepsilon - \mathbf{H}}$. In this thesis we employ the recursion method, which can be generally used in other models with Hamiltonian other than the TB Hamiltonian. In the TB model, the Hamiltonian is given as a matrix (expressed on a basis of localized orbitals) whose elements are the self-energies and near-neighbor hopping integrals. There may be several orbitals per atom; the hopping integrals are not restricted to nearest-neighbor interactions only. The recursion method sets up a new basis in which the Hamiltonian has a tridiagonal representation, from which the matrix elements of the Green's function are very simply derived. A tridiagonal matrix is one whose non-zero elements appear only on the main diagonal and the two sub-diagonals, upper right and lower left. Mathematically, given the Hamiltonian matrix $\mathbf{H}$, the recursion method generates a unitary transformation U, such that

$$U\mathbf{H}U^\dagger = \mathbf{H}_{\mathrm{TD}}, \qquad \text{(A.13)}$$

where the tridiagonal matrix elements of $\mathbf{H}_{\mathrm{TD}}$ are

$$[\mathbf{H}_{\mathrm{TD}}]_{mn} = \begin{cases} a_m, & \text{if } n = m, \\ b_{m+1}, & \text{if } n = m+1, \\ b_m, & \text{if } n = m-1, \\ 0, & \text{otherwise.} \end{cases} \tag{A.14}$$

Although the tridiagonal Hamiltonian $\mathbf{H}_{\mathrm{TD}}$ is identical in form to the representation of the Hamiltonian of a semi-infinite, nearest-neighbor interacting, linear chain of atoms (the so-called chain model), we are not confined to nearest-neighbor interactions in our starting Hamiltonian $\mathbf{H}$. The mathematical idea of the recursion method was developed many years ago, but known as the Lanczos method[152, 153]. Piage[154] discussed the numerical stability of the Lanczos method. In fact, the recursion method is one of the few techniques of stably retaining information contained in the high moments of the DOS.

Next we describe how to formulate the tridiagonal Hamiltonian matrix and to solve the LDOS from the Green's function, which is actually an inverse operator. Suppose we have a complete set of orthonormal states $\{|n\rangle, n = 0, 1, 2, \cdots\}$ in the Hilbert space expanded by the Hamiltonian $\mathbf{H}$ and they satisfy the recursion equation

$$\mathbf{H}|n\rangle = a_n|n\rangle + b_{n+1}|n+1\rangle + b_{n-1}|n-1\rangle, \tag{A.15}$$

where a_n's and b_n's are unknown coefficients.

The first step is to select an initial state $|0\rangle$. In the collinear framework, it is simply to choose the local orbitals for each site $\mathbf{R}_i$, orbital α and spin σ. Taking account of the electrons in the 3rd shell, we have electrons in subshells s, p and d, each orbital can hold two electrons, spin up and down. So we consider 18 initial states per atom in total. From each initial state we carry out the recursion method to obtain the LDOS, which is then integrated in the self-consistent procedure. In the case of non-collinearity, the selection of an initial state must be made more carefully, because the local moment could rotate. A local coordinate system solves this problem. The local magnetic moment $\overrightarrow{\mu}_{i\alpha}$ can be decomposed in the local

spherical basis with unit vector $(\hat{u}_{r_i}, \hat{u}_{\theta_i}, \hat{u}_{\varphi_i})$:

$$\overrightarrow{\mu}_{i\alpha} = \mu_{r_{i\alpha}}\hat{u}_{r_i} + \mu_{\theta_{i\alpha}}\hat{u}_{\theta_i} + \mu_{\varphi_{i\alpha}}\hat{u}_{\varphi_i}.$$

In this case we have 54 initial states per atom, three times more than the collinear case. The local components $(\mu_{r_{i\alpha}}, \mu_{\theta_{i\alpha}}, \mu_{\varphi_{i\alpha}})$ are generated from the same method we introduced in deriving the non-collinear Hamiltonian, see equation (2.25). In a global coordinate system, the spin components of local orbitals can be described in the spinor SU(2) space,

$$\begin{aligned} |i\alpha\uparrow\rangle &= |i\alpha\rangle \begin{pmatrix} 1 \\ 0 \end{pmatrix}, \\ |i\alpha\downarrow\rangle &= |i\alpha\rangle \begin{pmatrix} 0 \\ 1 \end{pmatrix}. \end{aligned} \tag{A.16}$$

Once the initial state $|0\rangle$ is selected, we use the recursion equation (A.15) to calculate the coefficients a_n and b_n. Since $|-1\rangle$ vanishes, when $n = 0$, the recursion equation reads

$$\mathbf{H}|0\rangle = a_0|0\rangle + b_1|1\rangle. \tag{A.17}$$

From the assumed orthonormality of $|n\rangle$'s, we obtain

$$a_0 = \langle 0|\mathbf{H}|0\rangle, \tag{A.18}$$

which is a real number because Hamiltonian operator $\mathbf{H}$ is hermitian. Reorganizing equation (A.17), the state $|1\rangle$ can be expressed as

$$|1\rangle = \frac{1}{b_1}(\mathbf{H} - a_0)|0\rangle. \tag{A.19}$$

The coefficient b_1 is given by the normalization of state $|1\rangle$,

$$b_1^2 = |(\mathbf{H} - a_0)|0\rangle|^2 \geq 0. \tag{A.20}$$

we choose b_1 to be the positive value $|(\mathbf{H} - a_0)|0\rangle|$, so that the first recursion is well defined.

To continue the recursive process, suppose we have performed the first n steps of the recursion, i.e., the orthonormal states $\{|0\rangle, |1\rangle, \cdots, |n\rangle, n \geq 1\}$ and coefficients $a_0, a_1, \cdots, a_{n-1}$ and $b_1, b_2, \cdots, b_n, (b_n \neq 0)$ are known, we next carry out the $(n+1)$th recursive relation to obtain the state $|n+1\rangle$. From equation (A.15), $a_n = \langle n|\mathbf{H}|n\rangle$ and $|n+1\rangle$ reads

$$|n+1\rangle = \frac{1}{b_{n+1}} \left[(\mathbf{H} - a_n)|n\rangle - b_n|n-1\rangle\right]. \tag{A.21}$$

The orthonormality of $|n+1\rangle$ determines the value of b_{n+1},

$$b_{n+1}^2 = \left|(\mathbf{H} - a_n)|n\rangle - b_n|n-1\rangle\right|^2. \tag{A.22}$$

We choose again the positive value. The orthogonality between $|n\rangle$ and $|n+1\rangle$ is used as assumption in the $(n+1)$th recursion, the only thing remained to be verified is the orthogonality of state $|n+1\rangle$ to the states $|0\rangle, |1\rangle, \cdots, |n-1\rangle$. For any $m \leq n-2$, we apply $\langle m|$ to equation (A.15),

$$\langle m|\mathbf{H}|n\rangle = b_{n+1}\langle m|n+1\rangle. \tag{A.23}$$

The operation of $\mathbf{H}$ on $|m\rangle$ results in a linear combination of states $|m\rangle$, $|m-1\rangle$ and $|m+1\rangle$, which are orthogonal to $|n\rangle$, so the left hand side of equation (A.23) vanishes, then states $|n+1\rangle$ and $|m\rangle$ are orthogonal. If applying $\langle n-1|$ to equation (A.15),

$$\langle n-1|\mathbf{H}|n\rangle = b_n + b_{n+1}\langle n-1|n+1\rangle. \tag{A.24}$$

$\langle n-1|\mathbf{H}|n\rangle = b_n$ is calculated using the previous recursion

$$\mathbf{H}|n-1\rangle = b_{n-1}|n-2\rangle + a_{n-1}|n-1\rangle + b_n|n\rangle.$$

So we verified the feasibility of the recursion method. The recursion procedure

ends when, for some n, $b_n = 0$. In the next section, we will solve the LDOS in the context of Green's function.

A.3 Calculating LDOS

The LDOS is calculated through its relation with Green's function,

$$\rho_{i\alpha\sigma} = -\frac{1}{\pi}\mathrm{Im}\langle i\alpha\sigma|G^{+}(\varepsilon)|i\alpha\sigma\rangle, \tag{A.25}$$

where $|i\alpha\sigma\rangle$ is an initial state chosen in the recursion method. With the recursion bases $\{|0\rangle, |1\rangle, \cdots, |n\rangle\}$, the Hamiltonian matrix $\mathbf{H}$ is largely simplified to be a tridiagonal matrix $\mathbf{H}_{\mathrm{HD}}$ in equation (A.14). The matrix form of Green operator $G(\varepsilon) = \frac{1}{\varepsilon - \mathbf{H}}$ is the inverse matrix of tridiagonal matrix $\varepsilon - \mathbf{H}$,

$$G(\varepsilon) = \frac{1}{\varepsilon - \mathbf{H}} = \begin{pmatrix} \varepsilon - a_0 & -b_1 & & & \\ -b_1 & \varepsilon - a_1 & -b_2 & & \\ & -b_2 & \varepsilon - a_2 & -b_3 & \\ & & -b_3 & \varepsilon - a_3 & \ddots \\ & & & \ddots & \ddots \end{pmatrix}^{-1}. \tag{A.26}$$

The LDOS only relates to the first element of the Green matrix, $G_{00}(\varepsilon)$. Denote a sequence of determinants $\{D_n\}$ to be

$$D_n = \begin{vmatrix} a_n & b_{n+1} & & & \\ b_{n+1} & a_{n+1} & b_{n+2} & & \\ & b_{n+2} & a_{n+2} & b_{n+3} & \\ & & b_{n+3} & a_{n+3} & \ddots \\ & & & \ddots & \ddots \end{vmatrix}, \tag{A.27}$$

the first element of Green matrix can be expressed as

$$G_{00}(\varepsilon) = \frac{D_1}{D_0}. \tag{A.28}$$

Performing the determinant calculation of matrix, D_0 can be described by determinants of matrices with lower order,

$$D_0 = (\varepsilon - a_0)D_1 - b_1^2 D_2. \tag{A.29}$$

Substituting equation (A.29) into equation (A.28), we get

$$G_{00}(\varepsilon) = \frac{1}{\varepsilon - a_0 - b_1^2 \frac{D_2}{D_1}}. \tag{A.30}$$

Continue to calculate the ratio $\frac{D_2}{D_1}$ and thereafter the ratio of determinants of matrices with lower order,

$$\frac{D_{n+1}}{D_n} = \frac{1}{\varepsilon - a_n - b_{n+1}^2 \frac{D_{n+2}}{D_{n+1}}}, \tag{A.31}$$

$G_{00}(\varepsilon)$ becomes an infinite continued fraction,

$$G_{00}(\varepsilon) = \cfrac{1}{\varepsilon - a_0 - \cfrac{b_1^2}{\varepsilon - a_1 - \cfrac{b_2^2}{\varepsilon - a_2 - \cfrac{b_3^2}{\ddots}}}}. \tag{A.32}$$

This equation allows us to calculate the LDOS only in terms of the coefficients obtained in the recursion method and without a need for diagonalizing the Hamiltonian matrix.

A.4 Terminating the continued fraction

The recursion relation gives a continued fraction expansion of the resolvent that is exact to all orders. In practice, however, it is impossible to make the exact

calculation to infinite order. One computes only the first N pairs of coefficients, $\{a_i, b_i\}$, and approximates the remaining coefficients, that is, one must approximate the remainder of the continued fraction beyond the Nth level. One possible way is to evaluate $G_{00}(\varepsilon + i\eta)$ for a small imaginary part. This means imposing a Lorentzian broadening on delta functions which constitute the real LDOS. This method is mostly used in the calculations of free clusters, in which the recursion coefficients tend to zero after a certain level. The continued fraction ends in a natural way. But in the case of infinite systems or semi-infinite systems, in general the recursion coefficients converge to zero indefinitely. In practice, fortunately, the recursion coefficients (a_i, b_i) settle down quickly and tend towards asymptotic values denoted by (a_∞, b_∞). By setting $(a_n, b_n) = (a_\infty, b_\infty)$ for $n > N$, we can evaluate the remainder of the continued fraction analytically. Thus the terminator is calculated by

$$t(\varepsilon) = \cfrac{b_{N+1}^2}{\varepsilon - a_{N+1} - \cfrac{b_{N+2}^2}{\varepsilon - a_{N+2} - \frac{b_{N+3}^2}{\varepsilon - \cdots}}} = \frac{b_\infty^2}{\varepsilon - a_\infty - t(\varepsilon)}. \tag{A.33}$$

For the second equality we have used the asymptotic property. Solving the quadratic equation for $t(\varepsilon)$, we obtain the terminator,

$$t(\varepsilon) = \frac{(\varepsilon - a_\infty) - \sqrt{(\varepsilon - a_\infty)^2 - 4b_\infty^2}}{2}. \tag{A.34}$$

The second solution is rejected because $t(\varepsilon)$ must vanish as $\varepsilon \to \infty$ in order that the resolvent preserves its analytic character (of the form ε^{-1}) there. $t(\varepsilon)$ is real for real ε outside the interval $(a_\infty - 2b_\infty, a_\infty + 2b_\infty)$, so that the continued fraction will be real, except for isolated delta functions should the real part of $G_{00}(\varepsilon)$ change sign. Inside the same interval, $t(\varepsilon)$ has a cut and we obtain a band of allowed energies. Note that if we set $(a_i, b_i) = (a_\infty, b_\infty)$ for all i, the LDS, proportional to

$$G_{00}(\varepsilon) = \frac{2}{\varepsilon - a_\infty - \sqrt{(\varepsilon - a_\infty)^2 - 4b_\infty^2}}, \tag{A.35}$$

is a featureless semi-ellipse, corresponding to a uniform effective medium. The deviations of the pairs of coefficients (a_i, b_i) for $0 \leq i \leq N$ add the structure to LDOS based on the information about the local atomic environment of the starting orbital.

As we have discussed, increasing the number of levels of continued fraction in our calculation, we get more and more accurate estimation of the "true" LDOS. However, the computing time increases considerably with this number. We must make a compromise between the accuracy and computing power. In the work of this thesis, we take 12 levels of the continued fraction, which provide sufficient quantities and a reasonable structure in LDOS, and do not need too much computing power.

Acknowledgements

I would like to express my deep gratitude to my research supervisor Prof. Dr. Gunnar Borstel for his constant support in solving scientific and administrative problems.

I am greatly thankful to Prof. Dr. Andrés Vega Hierro in Valladolid, Spain for his invaluable support, discussion, encouragement and the invitation to Valladolid during which time I learned a lot about the semi-empirical method used for the doctoral research. Without his help I could not publish the papers to an academic journal and this doctoral work would have never been done.

My special thanks are due to my colleagues, Dr. Eduardo Martínez Moreno and Homero Cantera Lopéz, for their helpful explanations discussions and various support.

Prof. Dr. Valery M. Uzdin in Petersburg, Russia, and Dr. Roberto Robles Rodríguez in Richmond, USA deserve my special thanks for their fruitful discussions via email.

I am very thankful to Prof. Dr. Ole Krogh Andersen and Prof. Dr. Ove Jepsen for their useful explanation of the LMTO method and the invitation to Max Planck Institute for Solid State Research, Stuttgart.

I am indebted to Mr. Werner Nienhüser and Mr. Frank Elsner, who gave me a lot of helps for managing the computers in our group, and Dr. Heidrun Elfering and Mrs. Susanne Guthoff, the secretary of the Promotionprogram and the secretary of our group, who helped me handling various administrative problems.

And finally, I would like to thank all the persons who gave me supports and helps during my Ph.D study, including my family, my friends.

This work has been supported financially by the Promotionsprogramm des Landes Niedersachsen “Synthesis and Characterization of Surfaces and Interfaces assembled from Clusters and Molecules”.

Bibliography

[1] J. P. Bucher, D. C. Douglass and L. A. Bloomfield, *Phys. Rev. Lett.* **66** (1991) 3052.

[2] I. M. L. Billas, A. Châtelain and W. A. de Heer, *Science* **265** (1994) 1682.

[3] E. E. Fullerton, J. S. Jiang, C. H. Sowers, J. E. Pearson and S. D. Bader, *Appl. Phys. Lett.* **72** (1998) 380.

[4] S. Jung, B. Watkins, L. DeLong, J. B. Ketterson and V. Chandrasekhar, *Phys. Rev. B* **66** (2002) 132401.

[5] U. Ebels, J. L. Duvail, P. E. Wigen, L. Piraus, L. D. Buda and K. Ounadjela, *Phys. Rev. B* **64** (2001) 144421.

[6] A. E. Berkowitz, J. R. Mitchell, M. J. Carey, A. P. Young, S. Zhang, F. E. Spada, F. T. Parker, A. Hutten and G. Thomas, *Phys. Rev. Lett.* **68** (1992) 3745.

[7] J. Q. Xiao, J. S. Jiang and C. L. Chien, *Phys. Rev. Lett.* **68** (1992) 3749.

[8] D. A. Thompson and J. S. Best, *IBM J. Res. Dev.* **44** (2000) 311.

[9] D. Weller and A. Moser, *IEEE Trans. Mag.* **29** (1999) 4423.

[10] R. D. Shull, *IEEE Trans. Mag.* **29** (1993) 2614.

[11] L. X. Tiefenauer, G. Kuehne and R. Y. Andres, *Bioconjugate Chem.* **4** (1993) 347.

[12] M. Beller, H. Fischer, K. Kuhlein, C. P. Reisinger and W. A. Herrmann, *J. Organometal. Chem.* **520** (1996) 257.

[13] C. r. Martin and P. Kohli, *Nat. Rev. Drug Dis.* **2** (2003) 29.

[14] G. Binnig, H. Rohrer, Ch. Gerber, and E. Weibel, *Phys. Rev. Lett.* **49** (1982) 57.

[15] G. Binnig, H. Rohrer, Ch. Gerber, and E. Weibel, *Phys. Rev. Lett.* **50** (1983) 120.

[16] G. Binnig, H. Rohrer, Ch. Gerber, and E. Weibel, *Appl. Phys. Lett.* **40** (1982) 178.

[17] J. W. Matthews, *Epitaxial Growth*, (New York: Academic, 1975).

[18] J. W. Evans, D. E. Sanders, P. A. Thiel, and Andrew E. DePristo, *Phys. Rev. B* **41** (1990) 5410.

[19] Deepak Venkateshvaran, Matthias Althammer, *et al.*, *Phys. Rev. B* **79** (2009) 134405.

[20] G. N. Philips, M. Siekman, L. Abelmann and J. C. Lodder, *Appl. Phys. Lett.* **81** (2002) 865.

[21] T. Kohashi and K. Koike, *Jpn. J. Appl. Phys.* bf 40 (2001) L1264.

[22] S. Heinze, M. Bode, A. Kubetzka, O. Pietzsch, X. Nie, S. Blügel and R. Wiesendanger, *Science* **288** (2000) 1805.

[23] M. Kleiber, M. Bode, R. Ravlić and R. Wiesendanger, *Phys. Rev. Lett.* **85** (2000) 4606.

[24] R. Liebmann, *Statistical Mechanics of Periodic Frustrated Ising Systems*, Lecture Notes in Physics, vol. 251 (Springer-Verlag, Berlin, 1986).

[25] G. Toulouse, *Commun. Phys.* **2** (1997) 115.

[26] J. Villain, *J. Phys. C* **10** (1977) 115.

[27] R. Robles, *Doctor thesis*, Universidad de Valladolid, 2003.

[28] E. Martínez, *Doctor thesis*, Universidad de Valladolid, 2007.

[29] P. Hohenberg and W. Kohn, *Phys. Rev.* **136** (1964) B864.

[30] W. Kohn and L. J. Sham, *Phys. Rev.* **140** (1965) A1133.

[31] Gy. Csanak, H. S. Taylor, and R. Yaris, *Adv. At. Mol. Phys* **7** (1971) 287.

[32] G. Onida, L. Reining, and A. Rubio, *Rev. Mod. Phys.* **74** (2002) 601.

[33] O. Madelung, *Introduction to Solid-State Theory* (Springer-Verlag, 1996).

[34] N. D. Ashcroft and N. W. Mermin, *Solid State Physics* (Harcourt, 1976).

[35] O. K. Andersen, *Phys. Rev. B* **12** (1975) 3060.

[36] O. K. Andersen and O. Jepsen, *Phys. Rev. Lett.* **53** (1984) 2571.

[37] O. K. Andersen, A. V. Postnikov and S. Z. Savrasov, *Mat. Res. Symp. Proc.* **253** (1992) 37.

[38] J. Hubbard, *Proceedings of Royal Society of London. Series A, Mathematical and Physical Sciences*, Vol. 276, No.1365, (1963) 238.

[39] J. Hubbard, *Proceedings of Royal Society of London. Series A, Mathematical and Physical Sciences*, Vol. 277, No. 1369, (1964) 237.

[40] J. Hubbard, *Proceedings of Royal Society of London. Series A, Mathematical and Physical Sciences*, Vol. 281, No. 1386, (1964) 401.

[41] J. Hubbard, *Proceedings of Royal Society of London. Series A, Mathematical and Physical Sciences*, Vol. 285, No. 1403, (1965) 542.

[42] J. Izquierdo, A. Vega and L. C. Balbás, *Phys. Rev. B* **55** (1997) 445.

[43] R. Robles, J. Izquierdo and A. Vega, *Phys. Rev. B* **61** (2000) 6848.

[44] J. Izquierdo, D. I. Bazhanov, A. Vega, V. S. Stepanyuk and W. Hergert, *Phys. Rev. B* **63** (2001) 140413(R).

[45] R. Haydock, V. Heine, and M. J. Kelly, *J. Phys. C: Solid State Phys.* **5** (1972) 2845.

[46] R. Haydock, V. Heine, and M. J. Kelly, *J. Phys. C: Solid State Phys.* **8** (1975) 2591.

[47] R. Haydock, *Solid State Physics*, edited by F. Seitz, H. Ehrenreich and D. Turnbull (Academic Press, London, 1980), Vol. 35, p. 215.

[48] J. C. Slater and G. F. Koster, *Phys. Rev. B* **94** (1954) 1498.

[49] W. A. Harrison, *Solid State Theory*, (Dover, New York, 1980).

[50] O. K. Andersen and O. Jepsen, *Physica B* **91** (1977) 317.

[51] O. K. Andersen, W. Close and H. Nohl, *Phys. Rev. B* **17** (1978) 1209.

[52] D. A. Papaconstantopoulos, *The Band Structure of Elemental Solids*, (Plenum Press, New York, 1986).

[53] O. K. Andersen, O. Jepsen and D. Glötzel, *Highlights of Condensed Matter Theory*, edited by F. Bassani, F. Fumi and M. P. Tossi, (North Halland, Amsterdam, 1985), p. 59.

[54] J. B. Mann, *Atomic Structure Calculations*, Los Alamos Sci. Lab. Rept., (1967) IA-3690.

[55] G. M. Pastor, J. Dorantes-Dávila and K.H. Bennemann, *Physica B* **149** (1988) 22.

[56] G. M. Pastor, J. Dorantes-Dávila and K.H. Bennemann, *Phys. Rev. B* **40** (1989) 7642.

[57] A. Vega, C. Demangeat and H. Dreyseé, *Phys. Rev. B* **51** (1995) 11546.

[58] D. Stoeffler and F. Gautier, *J. Magn. Magn. Mater.* **147** (1995) 260.

[59] A. Berger and H. Hopster, *Phys. Rev. Lett.* **73** (1994) 193.

[60] A. Berger and E. E. Fullerton, *J. Magn. Magn. Mater.* **165** (1997) 471.

[61] A. Kubetzka, O. Pietzsch, M. Bode and R. Wiesendanger, *Phys. Rev. B* **63** (2001) 140407(R).

[62] M. Bode, M. Getzlaff and R. Wiesendanger, *Phys. Rev. Lett.* **81** (1998) 4256.

[63] P. Grünberg, R. Schreiber, Y. Pang, M.B. Brodsky and H. Sowers, *Phys. Rev. Lett.* **57** (1986) 2442.

[64] S. S. P. Parkin, N. More and K. P. Roche, *Phys. Rev. Lett.* **64** (1990) 2304.

[65] N. N. Baibich, J. M. Broto, A. Fert, F. Nguyen Van Dau, F. Petroff, P. Etienne, G. Creuzet, A. Friedrich and J. Chazelas, *Phys. Rev. Lett.* **61** (1988) 2472.

[66] G. Binash, P. Grünberg, F. Saurenbach and W. Zinn, *Phys. Rev. B* **39** (1989) 4828.

[67] B. Dieny, V. S. Speriosu, S. S. Parkin, B. A. Gurney, D. R. Wilhoit and D. Mauri, *Phys. Rev. B* **43** (1991) 1297.

[68] B. Heinrich, A. S. Arrott, C. Liu and S. T. Purcell, *J. Vac. Sci. Technol. A* **5** (1987) 1935.

[69] T. Igel, R. Pfandzelter and H. Winter, *Surf. Sci.* **405** (1995) 182.

[70] D. A. Tulchinski, J. Unguris and R. J. Celotta, *J. Magn. Magn. Mater.* **212** (2000) 91.

[71] E. Kentzinger, U. Rücker, W. Caliebe, G. Goerigk, F. Werges, S. Nerger, J. Voigt, W. Schmidt, B. Alefeld, C. Fermon and Th. Brükel, *Physica B* **276-278** (2000). 586

[72] T. K. Yamada, M. M. J. Bischoff, T. Mizoguchi and H. van Kempen, *Surf. Sci.* **516** (2002) 179.

[73] M. A. Khan, S. Bouarab, H. Nait-Laziz, C. Demangeat and M. Benakki, *Surf. Sci.* **148** (1995) 76.

[74] D. Spišák and J. Hafner, *Phys. Rev. B* **55** (1997) 8304

[75] D. Spišák and J. Hafner, *Surf. Sci.* **601** (2007) 4348.

[76] A. C. Lawson, A. C. Larson, M. C. Aronson, S. Johnson, Z. Fisk, P. C. Canfield, J. D. Thompson and R. B. von Dreele, *J. Appl. Phys.* **76** (1994) 7049.

[77] H. Yamagata and K. Asayama, *J. Phy. Soc. Jpn.* **33** (1972) 400.

[78] M. O'Keefe and S. Anderson, *Acta Crystallogr., Sect. A: Crist. Phys. Diffr. Theor. Gen. Crystallogr.* **33** (1977) 914.

[79] H. Fujihisa and K. Takemura, *Phys. Rev. B* **52** (1995) 13257.

[80] H. Nakamura, K. Yoshimoto, M. Shiga, M. Nishi and K. Kakurai, *J. Phys.: Condens. Matter* **9** (1997) 4701.

[81] B. Canals and C. Lacroix, *Phys. Rev. B* **61** (2000) 11251.

[82] Y. Nishihata, M. Nakayama, N. Sano and H. Terushi, *J. Phys. Soc. Jpn.* **63** (1988) 319.

[83] W. F. Egelhoff, I. Jacob, J. M. Rudd, J. F. Cochran and B. Heinrich, *J. Vac. Sci. Technol. A* **8** (1990) 1582.

[84] D. Tian, S. C. Wu, F. Jona and P. M. Marcus, *Solid State Commun.* **70** (1989) 199.

[85] S. Andrieu, H. M. Fischer, M. Piccuch, A. Traverse and J. Mimault, *Phys. Rev. B* **54** (1996) 2822.

[86] T. G. Walker and H. Hopster, *Phys. Rev. B* **48** (1993) R3563.

[87] R. Wu and A. J. Freeman, *Phys. Rev. B* **51** (1995) 17131.

[88] R. Wu and A. J. Freeman, *J. Magn. Magn. Mater.* **161** (1996) 89.

[89] T. Asada and S. Blügel, *Physica B* **237** (1997) 359.

[90] M. Eder, J. Hafner and E. G. Moroni, *Phys. Rev. B* **61** (2000) 11492.

[91] T. Flores, M. Hansen and M. Wuttig, *Surf. Sci.* **279** (1992) 251.

[92] M. Wuttig, C. C. Knight, T. Flores and Y. Gauthier, *Surf. Sci.* **292** (1993) 189.

[93] M. Wuttig, T. Flores and C. C. Knight, *Phys. Rev. B* **48** (1993) 12082.

[94] M. Wuttig, B. Feldmann and T. Flores, *Surf. Sci.* **331-333** (1995) 659.

[95] Ch. Ross, B. Schirmer, M. Wuttig, Y. Gauthier, G. Bihlmayer and S. Blügel, *Phys. Rev. B* **57** (1998) 2607.

[96] S. K. Kim, Y. Tian, M. Montesano, F. Jona and P. M. Marcus, *Phys. Rev. B* **54** (1996) 5081.

[97] O. Rader, W. Gudat, D. Schmitz, C. Carbone and W. Eberhardt, *Phys. Rev. B* **56** (1997) 5053.

[98] M. M. J. Bischoff, T. Yamada, A. J. Quinn and H. van Kempen, *Surf. Sci.* **501** (2002) 155.

[99] R. Pfandzelter, T. Igel and H. Winter, *Surf. Sci.* **389** (1997) 317.

[100] E. C. Passamani, B. Croonenborghs, B. Degroote and A. Vantomme, *Phys. Rev. B* **67** (2003) 174424.

[101] J. Dresselhaus, D. Spanke, F. U. Hillebrecht, E. Kisker, G. van der Laan, J. B. Goedkoop and N. B. Brookes, *Phys. Rev. B* **56** (1997) 5461.

[102] Ch. Roth, Th. Kleemann, F. U. Hillebrecht and E. Kisker, *Phys. Rev. B* **52** (1995) R15691.

[103] P. Torelli, F. Sirotti and P. Ballone, *Phys. Rev. B* **68** (2003) 205413.

[104] S. Andrieu, M. Finazzi, F. Yubero, H. Fischer, P. Arcade, F. Chevrier, K. Hricovini, g. Krill and Piecuch, *J. Magn. Magn. Mater.* **165** (1997) 191.

[105] S. Andrieu, M. Finnazi, Ph. Bauer, H. Fischer, P. Lefevre, K. Hricovini, G. Krill and M. Piecuch, *Phys. Rev. B* **57** (1998) 1985.

[106] J. P. Perdew, *Electronic Structure of Solids'91*, (Akademie-Verlag, Berlin, 1991).

[107] J. P. Perdew, J. A. Chevary, S. H. Vosko, Koblar A. Jackson, Mark R. Pederson, D. J. Singh and Carlos Fiolhais, *Phys. Rev. B* **46** (1992) 6671.

[108] T. Ono and H. Tanaka, *J. Phys. Soc. Jpn.* **68** (1999) 3174.

[109] S. D. Bader, *Rev. Mod. Phys.* **78** (2006) 1.

[110] P. Bruno, *Phys. Rev. Lett* **83** (1999) 2425.

[111] C. Chappert and T. Devolder, *Nature* **432** (2004) 162.

[112] E. Saitoh, H. Miyajima, T. Yamaoka and G. Tatara, *Nature* **432** (2004) 203.

[113] D. Suess, *Appl. Phys. Lett.* **89** (2006) 113105.

[114] J. Hauschild, U. Gradmann and H. J. Elmers, *Appl. Phys. Lett.* **72** (1998) 3211.

[115] T. Eimüller, R. Kalchgruber, P. Fischer, G. Schütz, P. Guttmann, G. Schmahl, M. Köhler, K. Prügl, M. Scholz, F. Bammes and G. Bayreuther, *J. Appl. Phys.* **87** (2000) 6478.

[116] V. V. Volkov and Y. Zhu, *J. Magn. Magn. Matter* **214** (2000) 204.

[117] K. J. Kirk, J. N. Chapman, S. McVitie, P. R. Aitchison and C. D. W. Wilkinson, *Appl. Phys. Lett.* **75** (1999) 3683.

[118] W. H. Rippard, A. C. Perrella, P. Chalsani, F. J. Albert, J. A. Katine and R. A. Buhrman, *Appl. Phys. Lett.* **77** (2000) 1357.

[119] O. Pietzsch, A. Kubetzka, M. Bode and R. Wiesendanger, *Science* **292** (2001) 2053.

[120] V.M. Uzdin and C. Demangeat, *J. Phys.: Condens. Matter* **18** (2006) 2717.

[121] L.Thomas, F.Lionti, R.Ballou, D. Gatteschi, R. Sessoli and B. Barbara, *Nature* **83** (1996) 145.

[122] E.E. Fullerton, J. S. Jiang, M. Grimsditch, C. H. Sowers, and S. D. Bader, *Phys. Rev. B* **58** (1998) 12193.

[123] T. K. Yamada, M. M. J. Bischoff, G. M. M. Heijnen, T. Mizoguchi and H. van Kempen, *Phys. Rev. Lett.* **90** (2003) 056803.

[124] U. Schlickum, N. Janke-Gilman, W. Wulfhekel and J. Kirschner, *Phys. Rev. Lett.* **92** (2004) 107203.

[125] E. Martínez, A. Vega, R. Robles and A. L. Vázquez de Parga, *Phys. Lett. A* **337** (2005) 469.

[126] J. Hafner and D. Spišák, *Phys. Rev. B* **72** (2005) 144420.

[127] A. Ernst, J. Henk and R. K. Thapa, *J. Phys.: Condens. Matter* **17** (2005) 3269.

[128] T. K. Yamada, E. Martínez, A. Vega, R. Robles, D. Stoeffler, A. L. Vázquez de Parga, T. Mizoguchi and H. van Kempen, *Nanotechnology* **18** (2007) 235702.

[129] V.M. Uzdin and A. Vega, *Phys. Rev. B* **77** (2008) 134446 ; *Nanotechnology* **19** (2008) 315401.

[130] R. Robles, E. Martínez, D. Stoeffler and A. Vega, *Phys. Rev. B* **68** (2003) 094413.

[131] E. Martínez, R. Robles, D. Stoeffler and A. Vega, *Phys. Rev. B* **74** (2006) 184435.

[132] O.K. Andersen and O. Jepsen, *Phys. Rev. Lett.* **53** (1984) 2571.

[133] R. Haydock, in *Solid State Physics*, edited by H. Ehrenreich, F. Seitz, and D. Turnbull (Academic, New York, 1980), Vol. 35, p. 215.

[134] V.M. Uzdin and N.S. Yartseva, *J. Magn. Magn. Mat.* **203** (1999) 280.

[135] E. Kojima, A. Miyata, *et al*, *Phys. Rev. B* **77** (2008) 212408.

[136] J. Unguris, R. J. Celotta and D. T. Pierce, *Phys. Rev. Lett.* **67** (1991) 140.

[137] J. Unguris, R. J. Celotta and D. T. Pierce, *Phys. Rev. Lett.* **69** (1992) 1125.

[138] B. Heinrich, J. F. Cochran, T. Monchesky and R. Urban, *Phys. Rev. B* **59** (1999) 14529.

[139] F. Herman, J. Sticht and M.V. Schilfgaarde, *J. Appl. Phys.* **69** (1991) 4783.

[140] D. Stoeffler and C. Cornea, *Europhys. Lett.* **56** (2001) 282.

[141] V. Lauter-Pasyuk, H. J. Lauter, B. P. Toperverg, L. Romashev and V. Ustinov, *Phys. Rev. Lett.* **89** (2002) 167203.

[142] R. Ravlić, M. Bode and R. Wiesendanger, *J. Phys.: Condens. Matter* **15** (2003) S2513.

[143] R. S. Fishman, *Phys. Rev. Lett.* **81** (1998) 4979.

[144] D. T. Pierce, R. J. Celotta and J. Unguris, *J. Appl. Phys.* **73** (1993) 6201.

[145] C. Turtur and G. Bayreuther, *Phys. Rev. Lett.* **72** (1994) 1557.

[146] F. U. Hillebrecht, Ch. Roth, R. Jungblut, E. Kisker and A. Bringer, *Europhys. Lett.* **19** (1992) 711.

[147] P. D. Johnson, N. B. Brookes and Y. Chang, *Mater. res. Soc. Symp. Proc.* **231** (1992) 49.

[148] B. Heinrich, Z. Celinski, J. F. Cochran and M. From, *Magnetism and Structure in systems of Reduced Dimensions*, edited by R. F. C. Farrow, B. Dieny, M. Donath, A. Fert and B. D. Hermsmeir, NATO Advanced Study Institute Ser. B **309** (Plenum, New York, 1993), p. 101.

[149] M. Donath, D. Scholl and E. Kay, *Phys. Rev. B* **43** (1991) 13164.

[150] P. Fuchs, K. Totlandy and M. Landolt, *Proceedings of the 14th International Colloquium of Magnetic Films and Surfaces, E-MRS Symposium on Magnetic Ultrathin Films and Multilayers and Surfaces, Düsseldor, Germany 1994* (Elsevier, Amsterdam, 1995).

[151] A. Davies, J. A. Stroscio, D. T. Pierce and R. J. Celotta, *Phys. Rev. Lett.* **76** (1996) 4175.

[152] C. Lanczos, *J. Res. Natl. Bur. Stand.* **45** (1950) 255.

[153] J. H. Wilkinson, *The Algebraic Eegenvalue Problem*, (Oxford: Clarendon Press), 1965.

[154] C. C. Piage, *J. Inst. Math. Appl.* **10** (1972) 373.

Eidesstattliche Erklärung

Hiermit erkläre ich, dass ich die vorliegende Arbeit selbstständig und ohne fremde Hilfe verfasst, andere als die von mir angegebenen Quellen und Hilfsmittel nicht benutzt und die den benutzten Werken wörtlich oder inhaltlich entnommenen Stellen als solche kenntlich gemacht und keine vorherigen Promotionsversuche unternommen habe.

Osnabrück, Sep.30.2009

Huahai Tan

Curriculum Vitae

Personal Data

Name:	Huahai Tan
Birth Date:	Oct. 19, 1980
Birthplace:	Guangshui, Hubei Province, P.R. China

Education Background

1987-1993	The Children's School of CN15MCC, Guixi, Jiangxi Province, P.R. China Primary school
1993-1996	The Children's School of CN15MCC, Guixi, Jiangxi Province, P.R. China Junior middle school
1996-1999	The 1st Middle School, Guixi, Jiangxi Province, P.R. China Senior middle school
1999-2003	Tsinghua University, Beijing, P.R. China Bachelor of Science in Physics
2003-2006	Tsinghua University, Beijing, P.R. China Master of Science
2006-2009	Universität Osnabrück, Osnabrück, Germany Doctor of Science